Numerical Performance of the Holomorphic Embedding Method

by

Qirui Li

A Thesis Presented in Partial Fulfillment
of the Requirements for the Degree
Master of Science

Approved June 2018 by the
Graduate Supervisory Committee:

Daniel Tylavsky, Chair
Qin Lei
Yang Weng

ARIZONA STATE UNIVERSITY

August 2018

ABSTRACT

Recently, a novel non-iterative power flow (PF) method known as the Holomorphic Embedding Method (HEM) was applied to the power-flow problem. Its superiority over other traditional iterative methods such as Gauss-Seidel (GS), Newton-Raphson (NR), Fast Decoupled Load Flow (FDLF) and their variants is that it is theoretically guaranteed to find the operable solution, if one exists, and will unequivocally signal if no solution exists. However, while theoretical convergence is guaranteed by Stahl's theorem, numerical convergence is not. Numerically, the HEM may require extended precision to converge, especially for heavily-loaded and ill-conditioned power system models.

In light of the advantages and disadvantages of the HEM, this report focuses on three topics:

1. Exploring the effect of double and extended precision on the performance of HEM,
2. Investigating the performance of different embedding formulations of HEM, and
3. Estimating the saddle-node bifurcation point (SNBP) from HEM-based Thévenin-like networks using pseudo-measurements.

The HEM algorithm consists of three distinct procedures that might accumulate roundoff error and cause precision loss during the calculations: the matrix equation

solution calculation, the power series inversion calculation and the Padé approximant calculation. Numerical experiments have been performed to investigate which aspect of the HEM algorithm causes the most precision loss and needs extended precision. It is shown that extended precision must be used for the entire algorithm to improve numerical performance.

A comparison of two common embedding formulations, a scalable formulation and a non-scalable formulation, is conducted and it is shown that these two formulations could have extremely different numerical properties on some power systems.

The application of HEM to the SNBP estimation using local-measurements is explored. The maximum power transfer theorem (MPTT) obtained for nonlinear Thévenin-like networks is validated with high precision. Different numerical methods based on MPTT are investigated. Numerical results show that the MPTT method works reasonably well for weak buses in the system. The roots method, as an alternative, is also studied. It is shown to be less effective than the MPTT method but the roots of the Padé approximant can be used as a research tool for determining the effects of noisy measurements on the accuracy of SNBP prediction.

ACKNOWLEDGMENTS

First, I would like to express my deepest gratitude to my advisor, Dr. Daniel J. Tylavsky, for offering great support on this thesis research. I sincerely thank him for his invaluable guidance, patience and encouragement throughout my master studies. He sets a good example of researcher to our group by his sharp engineering insight and great enthusiasm in research.

I would like to thank my committee members, Dr. Qin Lei and Dr. Yang Weng for taking the time to give their invaluable feedback.

I express my sincere thanks to Shruti Rao, who brought me up to speed on the project. Without her endless guidance, I could not continue to improve my research work. I would also like to thank Yujia Zhu, Chinmay Vaidya, Songyan Li in the research group. Besides, I would like to thank Weili Yi and Yang Feng for their help.

In addition, I would like to express my appreciation to GEIRI North America, for providing financial support.

Finally, I would like to thank my parents and my friend Songjun Sun for the continuous emotional support they have given me throughout my time in graduate school.

TABLE OF CONTENTS

Page

CHAPTER Page

CHAPTER Page

CHAPTER Page

CHAPTER Page

LIST OF FIGURES

Figure Page

Figure Page

Figure Page

Figure Page

Figure Page

Figure Page

Figure Page

LIST OF TABLES

Table Page

NOMENCLATURE

α	Complex variable used in holomorphic embedding
α_0	Embedding parameter in the Padé-Weierstrass method
β	Embedding parameter for the pre-reference state power flow problem
σ	Parameter calculated using complex power and line impedance in a two-bus system
σ_R	The real part of σ
σ_I	The imaginary part of σ
a	Unknown coefficients in the numerator polynomial of the Padé approximant
A	Floating-point number
b	Unknown coefficients in the denominator polynomial of the Padé approximant
E	The exponent of a floating-point number
F	The mantissa of a floating-point number
L	Degree of numerator polynomial in the Padé approximant
M	Degree of denominator polynomial in the Padé approximant
n	Number of terms in power series
N	Number of buses in a power system
P_i	Real power injection at bus i
P_{gi}	Real power generated at bus i
P_{li}	Real power load at bus i
PQ	Set of PQ buses
PV	Set of PV buses

Q_i	Reactive power injection at bus i
Q_{gi}	Reactive power generated at bus i
Q_{li}	Reactive power load at bus i
Q_{gi_0}	Germ reactive power generation at bus i for the scalable formulation
$Q_{gi}\ (\alpha)$	Reactive power generation at PV bus represented as a power series
r	The base of a floating point number
R	Transmission line resistance
S_i	Complex power injection at bus i
U	Normalized Voltage
U_R	Real part of the normalized voltage
U_I	Imaginary part of the normalized voltage
V_i^{sp}	Specified voltage at bus i
V_s	Source voltage in the Thévenin-like network
V_{slack}	Slack bus voltage
$V_{i\ re}[n]$	Real part of the voltage series coefficient of degree n
$V_i[n]$	n^{th} order voltage series coefficients of bus i
$W_i(\alpha)$	Inverse voltage series for bus i
$W_i[n]$	n^{th} order inverse voltage series coefficients of bus i
X	Transmission line reactance
Y_{ik}	The component of the bus asmittance matrix between buses i and k
$Y_{i\ shunt}$	Shunt component of the bus admittance matrix at bus i

$Y_{ik\ trans}$	Non-shunt component of the bus admittance matrix between buses *i* and *k*
Z	Transmission line impedance
Z_L	Load impedance at the retained bus
Z_S	Source impedance from network impedance
Z_{th}	Thévenin impedance in the Thévenin equivalent network

1 INTRODUCTION

1.1 Power-flow problem

The power flow (PF) study is one of the most fundamental engineering studies conducted for power system steady-state analysis, planning and operation. It plays a key role in all other power system studies such as contingency analysis, power system expansion and transient stability simulations. The objective of the PF problem is to determine the magnitude and phase angle of the voltage at each bus in a balanced three phase power system [1]. As a by-product of the calculation, the real and reactive branch power flows and the losses in the network can be computed from the voltage solution.

Traditional iterative PF methods such as Gauss-Seidel (GS), Newton-Raphson (NR) and the Fast Decoupled Load Flow (FDLF) [2]-[6] have been widely used in the industry and usually work reliably under normal loading conditions. However, as is well-known, one common shortcoming of these traditional methods is that their numerical performance heavily depends on the choice of the initial estimate. When the system is heavily loaded, these methods may fail to converge or converge to a non-operable solution. Though many improvements to the existing PF algorithms have been proposed [7]-[13], the convergence is still not guaranteed in all cases and a more reliable method is needed.

1.2 Holomorphic embedding method

In mathematics, a holomorphic function is a complex-valued function that is complex differentiable in a neighborhood of every point in its domain. Since a holomorphic function is infinitely differentiable, it can be expressed as its own Taylor series. The Holomorphic Embedding Method (HEM) is known as a mathematical tool that can be used to advantage for solving some types of nonlinear equations.

The Holomorphic Embedding Load-flow Method (HELM), which is one variant of HEM method, was proposed by Dr. Antonio Trias in 2012 [14]. HELM represents a novel PF method that is distinct from established iterative PF methods. It is non-iterative but may be described as recursive. It is theoretically guaranteed to find the operable solution when it exists and unequivocally signal when there is no solution.

HEM is based on complex analysis. The central idea of HEM as it is applied to the PF problem, is to convert the non-holomorphic power balance equations (PBE's) into holomorphic functions by embedding a complex parameter α. Then the unknown variables can be expressed as a power series of α. The coefficients of the power series are calculated by establishing recursion relationship from the embedded PBE's. Then the Padé approximant [15], which provides maximal analytic continuation, is used to extend the radius of the convergence of power series. Finally, by setting $\alpha = 1$, the voltage solution is obtained.

Though convergence is theoretically guaranteed, numerical convergence is another matter. HEM has numerical issues especially for stressed power systems or systems which are described as "ill-conditioned." Practically, the closer the system loading level is to the Saddle Node Bifurcation Point (SNBP), the greater the number of terms of power series is required to get an accurate converged solution. Then, for example, when using the matrix Padé-approximate method, the matrix involved in the process can become severely ill-conditioned and thus cause precision loss. The issue of necessary precision is a non-negligible concern when implementing the HEM. Further, for a given problem, since there are an infinite number of embedding formulations, each with different numerical properties, the numerical performance issue is one that is likely to be investigated for some time to come. One of the first steps of course is deciding which formulation will, on average, have the best numerical performance, and that is a large problem deserving of study in and of itself.

1.3 Objectives

The research reported upon here has two main objectives. One is to explore how to improve the numerical performance of the HEM. Another one is to focus on one of its applications: Estimating the SNBP from HE-based reduced-order Thévenin-like network equivalents, which must be generated using pseudo-measurements and HE-based method.

This thesis covers the following topics. It:

- Introduces the theory of the HEM and describe two common HE formulations in detail.
- Describes the concept of arbitrary precision and introduces the toolbox used to implement arbitrary precision in this research.
- Shows the effect of high precision on the performance of HEM by two simple numerical examples.
- Investigates the numerical issues of the HEM by testing which part of the HEM algorithm causes the most precision loss and compares the performance of implementing high precision with Padé-Weierstrass technique.
- Explores the numerical properties of different embedding formulations to solve the PF problems.
- Validates the HE-based Thévenin-like network to estimate the SNBP on medium-sized power systems and evaluates the numerical performance of this theory.

1.4 Organization

This thesis is organized into seven chapters:

Chapter 2 includes a literature review of different methods of evaluating the saddle -node bifurcation point of a power system.

The implementation of an arbitrary-precision HEM is introduced in Chapter 3. In this chapter, two common HEM embedding formulations are discussed in detail and the improvement obtained by implementing the algorithms using high precision is illustrated in two simple numerical experiments: The PF results for the IEEE 14 bus system and the accuracy of the SNBP estimation from the HE-based so-called roots method for a two-bus system.

Chapter 4 presents the investigation of the numerical performance of HEM when the implementation uses high precision. Numerical experiments have been performed on several power systems to investigate which aspect of the HEM algorithm suffers from the worst numerical roundoff error behavior and therefore needs higher precision. Both a high precision implementation and the Padé-Weierstrass method are used to improve the numerical convergence for a problematic 43 bus system.

The numerical properties of the scalable formulation and the non-scalable formulation are given in Chapter 5. The comparison of the two formulations is performed on the 43 bus system and the IEEE 145 bus system.

Chapter 6 concentrates on the SNBP estimation from HE-based Thévenin-like networks using local-measurements. The Maximum Power Transfer Theorem (MPTT) is validated with extremely high precision. The comparison of four different numerical methods based on the MPTT are tested on the modified IEEE 118-bus system using pseudo-measurements. The roots method is also been discussed and compared with the

MPTT method. The effect of noisy measurements on the accuracy of SNBP estimation is explored.

Finally, the conclusion and the scope for the future work are included in Chapter 7.

2 LITERATURE REVIEW

In recent years, power systems are operated under increasingly stressed conditions, which has elevated the concern about system voltage stability. The saddle-node bifurcation point (SNBP) can be used as a useful voltage-stability-margin metric and hence the prediction of SNBP has received significant attention [16].

When the loads of a power system increase up to a critical limit, the static model of the power system will experience voltage collapse and this critical point is identified as a saddle-node bifurcation point. In mathematics, the SNBP represents the intersection points where different equilibria of a dynamical system meet [17]. When the dynamic model is constructed using classical machine models, the equilibria are represented by a set of nonlinear algebraic equations and the SNBP is a saddle-nose type of branch point in this set of algebraic equations. In this section, several methods of estimating the SNBP will be discussed.

2.1 Continuation Power Flow

The continuation power flow (CPF) [18] is a NR-based method which can be used to trace the P-V curve from a base case up to the maximum loading point by solving successive power flows while scaling up the load and generation level of the power system [18]. In the CPF method, the PF equations are reformulated to include a loading parameter to eliminate the singularity of Jacobian matrix when close to SNBP. The basic strategy behind the CPF is to use of a predictor-corrector scheme, which contains

two steps: One is to predict the next solution by taking a specified step size in the direction of a tangent vector corresponding to a different value of the load parameter. Then the other one is to correct the solution using a local parameterization technique.

The computational complexity of the CPF is much higher than the Newton-Raphson method since it requires calculating each operating point on the P-V curve. In addition, the control of the step size and the continuation parameter plays a key role in computational efficiency of CPF. For example, a small step size gives too many solution points and requires much computation time, whereas a large step size may give a poor starting point in predictor and thus cause divergence in corrector.

Various modified versions of CPF methods have been proposed to improve the accuracy and speed of the CPF. In [19]-[21], the geometric parameterization technique is used. In [22]-[24], modified predictor-corrector approaches are introduced. Techniques for controlling the step size are also proposed in [22]-[24]. In [25], multiple power injection variations in the power system are modeled.

References [19]-[21] present an efficient geometric parameterization technique for the CPF from the observation of the geometrical behavior of PF solutions. The Jacobian matrix singularity is avoided by the addition of a line equation, which passes through a point in the plane determined by the total real power losses and loading factor.

In [22], a singularity avoidance procedure is implemented around the SNBP. This method avoids the computational complexities of the existing CPFs and overcomes the

difficulty of how to smoothly cross through the SNBP and continue tracing the lower part of the P-V curve. In [23], the CPF with an adaptive step size control using a convergence monitor is proposed. It is shown that this approach needs much less time and does not need the critical buses preselected. A modified fast-decoupled power flow based CPF is reported in [24]. The use of a first-order polynomial secant predictor, where the step size controlled using the Euclidean norm of the tangent vector, reduces the number of iterations of the corrector step.

In [25], an improved CPF is proposed that allows the power injections at each bus to vary according to multiple load variations and actual real generation dispatch.

2.2 HEM-based methods

Since holomorphic embedding method can eliminate the non-convergence issues of those traditional iterative methods, this advantage can be exploited to develop methods that can reliably estimate the SNBP of a system. In [26], four different HEM-based methods to estimate the SNBP are proposed and compared in terms of accuracy as well as computational efficiency:

i. Power-Flow Search Method (PFSM)

In this approach, the PF equations are embedded in a non-extrapolating way such that the formulation is only valid at α =1 and has no meaningful interpretation at any other value of α. A binary search, which is similar to CPF, is performed until the SNBP is reached. This involves solving multiple PF problems and is of the order of the

complexity of the CPF. This approach is computationally the most expensive method over the four proposed HEM-based methods.

ii. Padé Approximant Search (PAS):

By using an extrapolation embedding formulation, the solution obtained at different values of α can represent the solution when the loads and real power generations of the system are uniformly scaled by a factor of α. Therefore, the PF problem only needs to be solved once to get the Padé approximants (PA's) and then, by evaluating the Padé approximants for various α values, using a binary search approach, the SNBP is obtained.

iii. Extrapolating Sigma Method (ESM)

The idea behind this method is to develop a two-bus equivalent network consisting of only slack bus and one retained bus and use the so-called σ index to estimate the SNBP of the system. The condition to ensure the system is short of or at its static voltage collapse point, called the 'σ condition' is given by:

$$\frac{1}{4} + \sigma_R - \sigma_I^2 \geq 0 \tag{2.1}$$

With the proposed extrapolation formulation, σ is obtained as a function of α. Then the SNBP of the system can be estimated by evaluating the Padé approximates for all the $\sigma_i(\alpha)$ at escalating values of α until the σ condition is violated.

iv. Roots method

In this approach, the extrapolation formulation is used to estimate the SNBP using the poles and zeros of the Padé approximates of an arbitrary bus. The smallest real zero/pole is taken as the load-scaling factor at the SNBP. Unlike (i), (ii) and (iii), the roots method does not involve any binary search process, which could be computationally expensive. This method is shown to be the most efficient of all the HEM methods, provided a reference state for the scalable-form power flow exists.

2.3 Measurement-based methods

The main idea of the local-measurement-based approach [32]-[37] comes from the impedance matching concept of the single-port Thévenin equivalent circuit: The local voltage and local current measurements are used to build a Thévenin equivalent representing the rest of the system. When the system is at the voltage collapse point, the Thévenin impedance has the same magnitude as load impedance. The parameters of the Thévenin equivalent are estimated using the least-squares method [32], [33], or Kalman filter method [37], or other alternative methods [34], [35]. A comparative study of four Thévenin equivalent identification methods was examined in [36]. Once the Thévenin equivalent parameters are obtained, a voltage stability index is computed to track the voltage stability margin. Some other indices such as power margin have been used in [33], [37] to provide information of how much load should be shed.

The wide deployment of phasor measurement units (PMU) has opened new perspectives for developing wide-area measurement-based methods to estimate voltage

stability margin [38]-[45]. Effort has been focused on building a more accurate model from measurements on all monitored buses [40], [41]-[43]. Reference [41] provides a modified coupled single-port model for long-term voltage stability assessment (VSA). In [42], a quasi-steady-state model for the external injections is constructed. A multiport Thévenin equivalent network has been built in [43] to better account for the different limits on individual tie-lines connecting to the load area. A comparison of different methods using local measurements or wide-area measurements to estimate the voltage stability margin was completed in [45].

3 APPLICATION OF HIGH PRECISION IN HEM

While in theory HEM is theoretically guaranteed to find the solution if it exists provide the problem formulation obeys the requirements of Stahl's theorem, the limitation of precision can have significant effect on the performance of any numerical algorithm selected. In this chapter, the application of high precision to voltage series obtained from a HEM-based solution of the PF problem will be discussed and the benefits obtained from high precision will be illustrated in two numerical examples. From a research perspective, the use of high-precision supports Stahl's theory of universal theoretical convergence (when a solution exists) and that non-convergence can be remedied through the use of high precision.

3.1 Arbitrary precision application

3.1.1 Floating-point arithmetic and arbitrary-precision arithmetic

Floating-point representation is the most common way of representing the approximation of a real number in a digital computer. A floating-point number A is represented approximately in the following form:

$$A = F \times r^{E}$$

Where F is represented using a fixed number of digits, which is referred to as the significand or mantissa, or coefficient, r is the base which is normally two, ten or sixteen and E is the exponent.

In the MATLAB environment, the floating-point numbers are represented in either double-precision or single-precision. The default is double precision. MATLAB constructs the floating-point data according to IEEE Standard 754. Any value stored as double in MATLAB will occupy 64 bits and its significand has a precision of 53 bits (about 16 decimal digits).

Increasing the precision of the floating-point representation generally helps to reduce round-off errors. The IEEE 754 standard for quadruple precision is a binary format that occupies 128 bits and has a significand precision of 113 bits (approximately 34 decimal digits). The binary formats for single precision, double precision and quadruple precision in IEEE Standard 754 are shown in Table 3.1.

Table 3.1 IEEE 754 Binary Float Formats

Type	Sign bits	Exponent bits	Total bits	Decimal digits
Single	1	8	32	7
Double	1	11	64	16
Quadruple	1	15	128	34

Arbitrary-precision arithmetic [46] consists of a set of algorithms, functions and data structures designed to deal with numbers that can be represented with arbitrary precision. There exist several software and libraries that support arbitrary-precision computations such as Maple, Mathematica, Multi-Precision Complex (MPC), etc. These implementations typically use variable arrays of digits instead of a fixed number of bits to store values.

3.1.2 Multiprecision Computing Toolbox

The arbitrary-precision application used in this research is called the Multiprecision Computing Toolbox [47]. This toolbox was selected mainly because it allows easy porting of existing MATLAB programs to arbitrary precision-with little or no modifications to the source code. It supplies arbitrary-precision support to the majority of mathematical functions in MATLAB.

Multiprecision Computing Toolbox is capable of working with any specified digit of precision if there is no hardware limitation. The default precision is assigned to 34 decimal digits which conforms to IEEE 754 for quadruple precision. This toolbox is designed to rely on recent state-of-the-art algorithms and multi-core parallelism to provide high performance. The comparison of Multiprecision Computing Toolbox with Symbolic Math Toolbox online [48] indicates that in some cases, the speed of quadruple precision computations in toolbox is comparable (or even higher) than the double precision routines of MATLAB.

3.2 Non-scalable formulation

Consider an *N*-bus system consisting of a slack bus, called *slack*, a set *PQ* of PQ buses and a set *PV* of PV buses.

The PBE for a PQ bus can be expressed as:

$$\sum_{k=1}^{N} Y_{ik} V_k = \frac{S_i^*}{V_i^*}, \qquad i \in PQ \tag{3.1}$$

where Y_{ik} is the (i,k) element of the bus admittance matrix, S_i is the complex power injection at bus i and V_i is the bus voltage at bus i.

The PBE for a PV bus are given by (3.2) and (3.3).

$$P_i = Re\left(V_i \sum_{k=1}^{N} Y_{ik}^* V_k^*\right), \qquad i \in PV \tag{3.2}$$

$$|V_i| = V_i^{sp}, \qquad i \in PV \tag{3.3}$$

where P_i is the real power injection at bus i and V_i^{sp} denotes the specified voltage magnitude at bus i.

The PBE for the slack bus is:

$$V_i = V_{slack}, \qquad i \in slack \tag{3.4}$$

where V_{slack} is the specified slack bus voltage in the system.

3.2.1 Embedded PBE's

To solve the PF problem, (3.1)-(3.4) will first be holomorphically embedded with a complex parameter α.There are infinite number of ways to embed the PBE's. One possible embedding formulation referred to as the non-scalable formulation is shown as follows:

$$\sum_{k=1}^{N} Y_{ik}^{trans} V_k(\alpha) = \frac{\alpha S_i^*}{V_i^*(\alpha^*)} - \alpha Y_i^{shunt} V_i(\alpha), \qquad i \in PQ \tag{3.5}$$

$$\sum_{k=1}^{N} Y_{ik}^{trans} V_k(\alpha) = \frac{\alpha P_i - jQ_i(\alpha)}{V_i^*(\alpha^*)} - \alpha Y_i^{shunt} V_i(\alpha), \qquad i \in PV \tag{3.6}$$

$$V_i(\alpha) * V_i^*(\alpha^*) = 1 + \alpha(\left|V_i^{sp}\right|^2 - 1),\ i \in PV \tag{3.7}$$

$$V_i(\alpha) = 1 + \alpha(V_{slack} - 1),\ i \in slack \tag{3.8}$$

where Y_{ik}^{trans} are the elements of the transmission admittance matrix, Y_i^{shunt} are shunt admittances, $Q_i$is the reactive power injection at bus i. Note that in (3.5), (3.6) and (3.7), the complex conjugate of the bus voltage is embedded as $V^*(\alpha^*)$ instead of $V^*(\alpha)$. This is because $V^*(\alpha)$ is not holomorphic since it does not satisfy Cauchy-Riemann conditions. Therefore, this formulation uses the expression $V^*(\alpha^*)$ to retain the holomorphicity of the function. For this reason, (3.5), (3.6) and (3.7) represent the original power system only for real α values and only at $\alpha = 1$.

Since $V(\alpha)$ and $Q(\alpha)$ are holomorphic functions of the parameter α, they can be represented in their following Maclaurin series form:

$$V(\alpha) = V[0] + V[1]\alpha + V[2]\alpha^2 + \cdots + V[n]\alpha^n \tag{3.9}$$

$$Q(\alpha) = Q[0] + Q[1]\alpha + Q[2]\alpha^2 + \cdots + Q[n]\alpha^n \tag{3.10}$$

The Maclaurin series for $V^*(\alpha^*)$ is given by:

$$V^*(\alpha^*) = V^*[0] + V^*[1]\alpha + V^*[2]\alpha^2 + \cdots + V^*[n]\alpha^n \tag{3.11}$$

Additionally, let a power series $W(\alpha)$ represent the inverse of the voltage function. The $W(\alpha)$ and $W^*(\alpha^*)$ are given by (3.12), and (3.13).

$$W(\alpha) = \frac{1}{V(\alpha)} = W[0] + W[1]\alpha + W[2]\alpha^2 + \cdots + W[n]\alpha^n \tag{3.12}$$

$$W^*(\alpha^*) = \frac{1}{V^*(\alpha^*)} = \tag{3.13}$$

$$W^*[0] + W^*[1]\alpha + W^*[2]\alpha^2 + \cdots + W^*[n]\alpha^n$$

Observe that at $\alpha = 1$, the PBE's are recovered from the embedded formulation, therefore, the solution at $\alpha = 1$ for $V(\alpha)$ is the solution for the original PF problem.

3.2.2 Reference state solution

By substituting (3.9), (3.10), (3.11) and (3.13) into (3.5), (3.6), (3.7) and (3.8), we obtain:

$$\sum_{k=1}^{N} Y_{ik}^{trans}(V_k[0] + V_k[1]\alpha + V_k[2]\alpha^2 + \cdots) = \alpha S_i^*(W_i^* + W_i^*[1]\alpha + W_i^*[2]\alpha^2 + \cdots), i \in PQ \tag{3.14}$$

$$\begin{aligned}\sum_{k=1}^{N} Y_{ik}^{trans}(V_k[0] + V_k[1]\alpha + V_k[2]\alpha^2 + \cdots) &= (\alpha P_i - j(Q_i[0] + Q_i[1]\alpha + Q_i[2]\alpha^2 + \cdots) \cdot \\ (W_i^*[0] + W_i^*[1]\alpha + W_i^*[2]\alpha^2 + \cdots) &- \alpha Y_i^{shunt}(V_i[0] + V_i[1]\alpha + V_i[2]\alpha^2 + \cdots), i \in PV\end{aligned} \tag{3.15}$$

$$\begin{aligned}&(V_i[0] + V_i[1]\alpha + V_i[2]\alpha^2 + \cdots) \cdot \\ &(V_i^*[0] + V_i^*[1]\alpha + V_i^*[2]\alpha^2 + \cdots) = 1 + \alpha(\left|V_i^{sp}\right|^2 - 1),\ i \in PV\end{aligned} \tag{3.16}$$

$$V_i[0] + V_i[1]\alpha + V_i[2]\alpha^2 + \cdots = 1 + \alpha(V_{slack} - 1), i \in slack \tag{3.17}$$

The reference state represents the case where $\alpha = 0$, which for these equations represent the case where there is no load/generation in the system. It is calculated by setting α equal to 0. The set of equations to be solve for the reference state solution is given by:

$$\sum_{k=1}^{N} Y_{ik}^{trans} V_k[0] = 0\,, \qquad i \in PQ \tag{3.18}$$

$$\sum_{k=1}^{N} Y_{ik}^{trans} V_k[0] = -jQ_i[0]W_i^*[0], \qquad i \in PV \tag{3.19}$$

$$V_i[0] * V_i^*[0] = 1, \qquad i \in PV \tag{3.20}$$

$$V_i[0] = 1, \ i \in slack \tag{3.21}$$

Notice that (3.18), (3.19), (3.20) and (3.21) can be satisfied if all the bus voltages are 1.0 pu and all reactive power injections at the PV buses are zero. Thus, the solution at α=0 can be easily obtained by observation instead of calculation. The reference state solution is:

$$V_i[0] = 1, i \in PQ \cup PV \cup slack \tag{3.22}$$

$$W_i[0] = \frac{1}{V_i[0]} 1, i \in PQ \cup PV \cup slack \tag{3.23}$$

$$Q_i[0] = 0, i \in PV \tag{3.24}$$

3.2.3 Power series calculation

3.2.3.1 Recurrence relation

In section 3.2.2, the constant terms of $V_i(\alpha)$ and $Q_i(\alpha)$ have been obtained. The next step is to establish the recurrence relation to find the remaining terms of the power series. The recurrence relation is obtained by equating the coefficients of the same order of α on both sides of equations (3.14), (3.15), (3.16) and (3.17). Obtaining the recurrence relation for PQ buses and slack bus is relatively straight forward. The recurrence relation is given by equations (3.25) and (3.26) respectively.

$$\sum_{k=1}^{N} Y_{ik}^{trans} V_k[n] = S_i^* W_i^*[n-1] - Y_i^{shunt} V_i[n-1], i \in PQ \tag{3.25}$$

$$V_i[n] = \delta_{n0} + \delta_{n1}(V_{slack} - 1), \quad i \in slack \tag{3.26}$$

where δ_{ni} is the Kronecker delta, defined by (3.27).

$$\delta_{ni} = \begin{cases} 1, if\ n = i \\ 0, otherwise \end{cases} \tag{3.27}$$

For the PV buses, when equating the coefficients of n^{th} order on both sides in (3.15), the $-\mathrm{j}Q_i(\alpha)W_i^*(\alpha)$ term can be written as a convolution of two power series. The recurrence relation is expressed as:

$$\begin{aligned} &\sum_{k=1}^{N} Y_{ik}^{trans} V_k[n] = P_i W_i^*[n-1] \\ &-j \sum_{m=0}^{n} Q_i[m] W_i^*[n-m] - Y_i^{shunt} V_i[n-1], i \in PV \end{aligned} \tag{3.28}$$

Equating the coefficients on both sides in (3.16) yields,

$$\begin{aligned} &V_i[0]V_i^*[0] = 1 \\ &\Longrightarrow V_i[0] = 1 \text{ (reference state)} \\ &V_i[0]V_i^*[0] + V_i[1]V_i^*[0] = \left|V_i^{sp}\right|^2 - 1 \\ &\Longrightarrow V_i^*[1] + V_i[1] = 2V_{ire}[1] = \left|V_i^{sp}\right|^2 - 1 \\ &\vdots \\ &V_i[0]V_i^*[n] + V_i[1]V_i^*[n-1] + \cdots + V_i[n-1]V_i^*[1] + V_i[n]V_i^*[0] \\ &\qquad = 0 \end{aligned} \tag{3.29}$$

$$\Longrightarrow V_i^*[n] + V_i[n] = 2V_{ire}[n] = -\sum_{k=1}^{n-1} V_i[k]V_i^*[n-k]$$

where $V_{ire}[n]$ represents the real part of the n^{th} coefficient of the voltage power series. The notation δ_{ni} as defined in (3.27) is used to write a generalized expression to evaluate $V_{ire}[n]$. The calculation of $V_{ire}[n]$ for an arbitrary n can be written as:

$$V_{ire}[n] = \delta_{n0} + \delta_{n1}\frac{\left|V_i^{sp}\right|^2 - 1}{2} - \frac{1}{2}\sum_{k=1}^{n-1} V_i[k]V_i^*[n-k], i \in PV \tag{3.30}$$

Note that in equations (3.25) and (3.28), a new unknown $W_i[n]$ is introduced. The relationship between $W_i[n]$ and $V_i[n]$ is obtained as given in (3.31) by equating the coefficients of the same order of α on both sides of (3.12).

$$W_i[0]\,V_i[0] = 1$$

$$\Longrightarrow W_i[0] = 1 \text{ (reference state)}$$

$$W_i[0]V_i[1] + W_i[1]V_i[0] = 0 \tag{3.31}$$

$$\vdots$$

$$W_i[0]V_i[n] + W_i[1]V_i[n-1] + \cdots + W_i[n-1]V_i[1] + \mathrm{W}[n]V_i[0] = 0$$

The n^{th} coefficient for $W_i(\alpha)$ can be calculated by:

$$W_i[n] = -\frac{\sum_{k=1}^{n} V_i[k]W_i[n-k]}{V_i[0]} \tag{3.32}$$

3.2.3.2 Calculation process

To recursively calculate the remaining coefficients of $V_i(\alpha)$ and $Q_i(\alpha)$, all the knowns and unknowns in (3.25), (3.26), (3.28) and (3.30) need to be moved to the RHS and LHS respectively. Observe that in (3.28), the values $Q_i[n]$ and $W_i^*[n]$ on the RHS are unknowns. Rearrange equation (3.28) to obtain:

$$\begin{aligned}
&\sum_{k=1}^{N} Y_{ik}^{trans} V_k[n] = P_i W_i^*[n-1] \\
&-j\left(\sum_{m=1}^{n-1} Q_i[m] W_i^*[n-m] + Q_i[0] W_i^*[n] + Q_i[n] W_i^*[0]\right) \\
&\qquad - Y_i^{shunt} V_i[n-1], i \in PV \\
&\sum_{k=1}^{N} Y_{ik}^{trans} V_k[n] = P_i W_i^*[n-1] \\
&-j\left(\sum_{m=1}^{n-1} Q_i[m] W_i^*[n-m] + 0 \cdot W_i^*[n] + Q_i[n] \cdot 1\right) \\
&-Y_i^{shunt} V_i[n-1], i \in PV \\
&\sum_{k=1}^{N} Y_{ik}^{trans} V_k[n] + jQ_i[n] W_i^*[0] = P_i W_i^*[n-1] \\
&-j \sum_{m=1}^{n-1} Q_i[m] W_i^*[n-m] - Y_i^{shunt} V_i[n-1], i \in PV
\end{aligned} \tag{3.33}$$

Breaking the transmission admittance matrix and complex coefficients of $V(\alpha)$, $W(\alpha)$ into real and imaginary parts, the power series coefficients can be obtained by solving a real-valued linear matrix equation consisting of (3.25), (3.26) and (3.33). Assuming bus 1 is the slack bus, bus p ($p = 2,3..M$) is a PV bus and bus q ($q = M + 1, M + 2..N$) is a PQ bus, the matrix equation to compute the n^{th} term is given as:

$$\begin{bmatrix} 1 & 0 & \cdots & 0 & 0 & \cdots & 0 & 0 & \cdots \\ 0 & 1 & \cdots & 0 & 0 & \cdots & 0 & 0 & \cdots \\ \vdots & \vdots & \vdots & \vdots & \vdots & \vdots & \vdots & \vdots & \vdots \\ G_{p1} & -B_{p1} & \cdots & 0 & -B_{pp} & \cdots & G_{pq} & -B_{pq} & \cdots \\ B_{p1} & G_{p1} & \cdots & 1 & G_{pp} & \cdots & B_{pq} & G_{pq} & \cdots \\ \vdots & \vdots & \vdots & \vdots & \vdots & \vdots & \vdots & \vdots & \vdots \\ G_{q1} & -B_{q1} & \cdots & 0 & -B_{qp} & \cdots & G_{qq} & -B_{qq} & \cdots \\ B_{q1} & G_{q1} & \cdots & 0 & G_{qp} & \cdots & B_{qq} & G_{qq} & \cdots \\ \vdots & \vdots & \vdots & \vdots & \vdots & \vdots & \vdots & \vdots & \vdots \end{bmatrix} \begin{bmatrix} V_{1re}[n] \\ V_{1im}[n] \\ \vdots \\ Q_p[n] \\ V_{pim}[n] \\ \vdots \\ V_{qre}[n] \\ V_{qim}[n] \\ \vdots \end{bmatrix}$$

$$= \begin{bmatrix} \delta_{n0} + \delta_{n1}(V_{slack} - 1) \\ 0 \\ \vdots \\ Re\left\{P_p W_p^*[n-1] - j\sum_{m=1}^{n-1} Q_p[m] W_p^*[n-m] - Y_p^{shunt} V_p[n-1]\right\} \\ Im\left\{P_p W_p^*[n-1] - j\sum_{m=1}^{n-1} Q_p[m] W_p^*[n-m] - Y_p^{shunt} V_p[n-1]\right\} \\ \vdots \\ Re\{S_q^* W_q^*[n-1] - Y_q^{shunt} V_q[n-1]\} \\ Im\{S_q^* W_q^*[n-1] - Y_q^{shunt} V_q[n-1]\} \\ \vdots \end{bmatrix} \quad (3.34)$$

$$- \cdots - \begin{bmatrix} 0 \\ 0 \\ \vdots \\ G_{pp} \\ B_{pp} \\ \vdots \\ G_{qp} \\ B_{qp} \\ \vdots \end{bmatrix} V_{pre}[n] - \cdots$$

where G_{ik} and B_{ik} are the real and imaginary parts of the transmission matrix entries $Y_{trans}(i,k)$, and V_{ire} and V_{iim} are the real and imaginary parts of the voltage power series coefficients, respectively. Notice that all values of $V_{ire}[n]$ for the PV buses are obtained from (3.30) before (3.34) is solved.

In summary, the process used to calculate the power series is shown below:

1. Calculate the reference state solution at $\alpha = 0$ using (3.22), (3.23) and (3.24).

2. Calculate $W[n-1]$ for all buses from $W[i]$ $(i < n-1)$ and $V[i]$ $(i \leq n-1)$ using (3.32).
3. Calculate $V_{ire}[n]$ for PV buses using (3.30).
4. Calculate $V_{ire}[n]$ for slack bus and PQ buses and $V_{iim}[n]$ for all buses by solving a linear matrix equation (3.34).
5. Set $n = n + 1$. Repeat steps 2 through 4.

3.2.4 Padé approximant

As stated previously, the solution at $\alpha = 1$ is the solution of the PF problem. Since the power series obtained from the recurrence relationships given above will only converge within its radius of convergence (ROC), analytic continuation is used to find the converged solution of the voltage function. Stahl's theorem [49] proves that the sequence of near-diagonal Padé approximant is the maximal analytic continuation of the power series, provided these equations obey the requirements stipulated in the equation. Thus, the Padé approximant will be used to evaluate the voltage solution.

The Padé approximant is a rational-form approximation to a power series. Assume a power series is expressed as follows:

$$c(\alpha) = c[0] + c[1]\alpha + c[2]\alpha^2 + c[3]\alpha^3 + \cdots = \sum_{n=0}^{\infty} c[n]\alpha^n \tag{3.35}$$

where $c[n]$ is the power series coefficient of the n^{th} order term.

For the power series given by (3.35) truncated to L+M+1 terms, the Padé approximant can be expressed as the rational form of two polynomials, $a(\alpha)$ and $b(\alpha)$ as given in (3.36).

$$[L/M] = \frac{a[0] + a[1]\alpha + a[2]\alpha^2 + \cdots a[L]\alpha^L}{b[0] + b[1]\alpha + b[2]\alpha^2 + b[M]\alpha^M} \tag{3.36}$$

In (3.36), L is the degree of the numerator polynomial a(α) and M is the degree of the denominator polynomial $b(\alpha)$.

The approximant in (3.36) is referred as$[L/M]$ Padé. If $L = M$, it is a diagonal Padé approximant. If $|L - M| = 1$, it is said to be a near-diagonal Padé approximant. The $[L/M]$ Padé can be evaluated from the power series in (3.35) truncated at $(L + M)$-th order, given in (3.37):

$$\begin{aligned} c(\alpha) &= c[0] + c[1]\alpha + c[2]\alpha^2 + \cdots c[L+M]\alpha^{L+M} + O(\alpha^{L+M+1}) \\ &= \frac{a[0] + a[1]\alpha + a[2]\alpha^2 + \cdots a[L]\alpha^L}{b[0] + b[1]\alpha + b[2]\alpha^2 + \cdots b[M]\alpha^M} = \frac{a(\alpha)}{b(\alpha)} \end{aligned} \tag{3.37}$$

Multiplying (3.37) by $b(\alpha)$ on both sides to obtain:

$$\begin{aligned} &(c[0] + c[1]\alpha + c[2]\alpha^2 + \cdots c[L+M]\alpha^{L+M})(b[0] + b[1]\alpha + b[2]\alpha^2 \\ &+ \cdots b[M]\alpha^M) = a[0] + a[1]\alpha + a[2]\alpha^2 + \cdots a[L]\alpha^L \end{aligned} \tag{3.38}$$

Equating the coefficients of α^0, α^1, $\alpha^2 \ldots \alpha^L$at both sides of (3.38) , we obtain:

$$\begin{aligned} b[0]c[0] &= a[0] \\ b[0]c[1] + b[1]c[0] &= a[1] \\ b[0]c[2] + b[1]c[1] + b[2]c[0] &= a[2] \\ &\vdots \end{aligned} \tag{3.39}$$

$$\sum_{i=0}^{\min(L,M)} b[i]c[L-i] = a[L]$$

It can be observed that the coefficients of α^{L+1} through α^{L+M} on the LHS of (3.38) have to be zero since there are no corresponding terms on the RHS of (3.38). Equating the coefficients of α^{L+1}, α^{L+2}, …α^{L+M}at both sides of (3.38), we obtain:

$$\begin{aligned} b[0]c[L+1] + \cdots b[M-1]c[L-M+2] + b[M]C[L-M+1] &= 0 \\ b[0]c[L+2] + \cdots b[M-1]c[L-M+3] + b[M]C[L-M+2] &= 0 \\ \vdots & \\ b[0]c[L+M] + \cdots b[M-1]c[L+1] + b[M]C[L] &= 0 \\ if\ M > L, c[j] = 0, j < 0 & \end{aligned} \tag{3.40}$$

Notice that with (3.39) and (3.40), we have L+M+1 knowns while there are L+M+2 unknowns in $a(\alpha)$ and $b(\alpha)$. Therefore, one of the coefficients in either $a(\alpha)$ or $b(\alpha)$ is a free variable. For simplicity, the value for $b[0]$ is chosen to be 1.0.

The system of equations given in (3.40) can be written in the matrix form given by (3.41). The coefficients of the denominator polynomial $b(\alpha)$ can be obtained by solving (3.41) through the LU factorization of the Padé matrix and forward/backward substitution.

$$\begin{bmatrix} c[L-M+1] & c[L-M+2] & c[L-M+3] & \cdots & c[L] \\ c[L-M+2] & c[L-M+3] & c[L-M+4] & \cdots & c[L+1] \\ c[L-M+3] & c[L-M+4] & c[L-M+5] & \cdots & c[L+2] \\ \vdots & \vdots & \vdots & \vdots & \vdots \\ c[L] & c[L+1] & c[L+2] & \cdots & c[L-M] \end{bmatrix} \begin{bmatrix} b[M] \\ b[M-1] \\ b[M-2] \\ \vdots \\ b[1] \end{bmatrix} \tag{3.41}$$

$$= -\begin{bmatrix} c[L+1] \\ c[L+2] \\ c[L+3] \\ \vdots \\ c[L+M] \end{bmatrix}$$

With the coefficients obtained for $b(\alpha)$, then from equation (3.39), the coefficients for the numerator polynomial $a(\alpha)$ can be evaluated. Thus, both the numerator and denominator polynomials of Padé approximant can be obtained. For the PF problem, the converged solution evaluated from the Padé approximant of $V(\alpha)$ at $\alpha = 1$ is guaranteed to be the operable solution, provided a solution exists.

3.3 Scalable formulation

The non-scalable formulation given in section 3.2 represents the original PBE's only at $\alpha = 1$ and the $V(\alpha)$ evaluated at any other value of α is meaningless. The scalable formulation [26] given in this section, however, can allow the solution obtained at different values of α to represent the solution when all loads and real power generations are uniformly scaled by a factor of α. Consider the following set of holomorphically embedded equations, where (3.42) represents the PBE for PQ buses (3.1), (3.43) represents the PBE for PV buses (3.2), (3.44) represents the voltage magnitude constraint for the PV buses (3.3) and (3.45) represents voltage constraint for the slack bus (3.4),

$$\sum_{k=1}^{N} Y_{ik} V_k(\alpha) = \frac{\alpha S_i^*}{V_i^*(\alpha^*)}, \qquad i \in PQ \tag{3.42}$$

$$\sum_{k=1}^{N} Y_{ik} V_k(\alpha) = \frac{\alpha P_i + j\alpha Q_{li} - jQ_{gi}(\alpha)}{V_i^*(\alpha^*)}, \qquad i \in PV \tag{3.43}$$

$$V_i(\alpha) * V_i^*(\alpha^*) = \left|V_i^{sp}\right|^2, \ i \in PV \tag{3.44}$$

$$V_i(\alpha) = V_{slack}, \ i \in slack \tag{3.45}$$

where P_i denotes the real power injection at bus i, $Q_{gi}(\alpha)$ denotes the reactive power generation at bus i and Q_{li} denotes the reactive power load at bus i. Note that in (3.43), Q_{gi} is written as a function of α so that the variable value of the reactive power generation needed to maintain bus voltage control is calculated from the power series while the real power injection P_i and reactive power load Q_{li} are scaled by a factor of α.

Substituting (3.9), (3.13) and $Q_{gi}(\alpha)$, defined by $Q_{gi}(\alpha) = Q_{gi}[0] + Q_{gi}[1]\alpha + Q_{gi}[2]\alpha^2 + \cdots$into (3.42), (3.43), (3.44) and (3.45), we obtain:

$$\begin{aligned} &\sum_{k=1}^{N} Y_{ik}(V_k[0] + V_k[1]\alpha + V_k[2]\alpha^2 + \cdots) \\ &= \alpha S_i^*(W_i^*[0] + W_i^*[1]\alpha + W_i^*[2]\alpha^2 + \cdots), i \in PQ \end{aligned} \tag{3.46}$$

$$\begin{aligned} &\sum_{k=1}^{N} Y_{ik}(V_k[0] + V_k[1]\alpha + V_k[2]\alpha^2 + \cdots) \\ &= (\alpha(P_i + jQ_{li}) - j\big(Q_{gi}[0] + Q_{gi}[1]\alpha + Q_i[2]\alpha^2 + \cdots\big) \cdot \\ &\quad (W_i^*[0] + W_i^*[1]\alpha + W_i^*[2]\alpha^2 + \cdots) \\ &-\alpha Y_i^{shunt}(V_i[0] + V_i[1]\alpha + V_i[2]\alpha^2 + \cdots), i \in PV \end{aligned} \tag{3.47}$$

$$\begin{aligned} &(V_i[0] + V_i[1]\alpha + V_i[2]\alpha^2 + \cdots) \cdot \\ &(V_i^*[0] + V_i^*[1]\alpha + V_i^*[2]\alpha^2 + \cdots) = \left|V_i^{sp}\right|^2, \ i \in PV \end{aligned} \tag{3.48}$$

$$V_i[0] + V_i[1]\alpha + V_i[2]\alpha^2 + \cdots = V_{slack}, i \in slack \tag{3.49}$$

3.3.1 Reference state calculation

The system of equations to be solved for the reference state at $\alpha = 0$ is given by (3.50)-(3.53).

$$\sum_{k=1}^{N} Y_{ik} V_k[0] = 0\,, \qquad i \in PQ \tag{3.50}$$

$$\sum_{k=1}^{N} Y_{ik} V_k[0] = -jQ_{gi}[0] W_i^*[0]\,, \qquad i \in PV \tag{3.51}$$

$$V_i[0] * V_i^*[0] = \left|V_i^{sp}\right|^2,\ i \in PV \tag{3.52}$$

$$V_i[0] = V_{slack}, \qquad i \in slack \tag{3.53}$$

Note that the reference state cannot be obtained only through observation. To calculate the reference state, the voltages and reactive power generation at $\alpha = 0$ can be represented as different Maclaurin series of the complex embedding parameter β, and the above equations (3.50)-(3.53) are going to embedded into a non-scalable form as given by (3.54)-(3.57),

$$\sum_{k=1}^{N} Y_{ik}^{trans} V_{k\_0}(\beta) = -\beta Y_i^{shunt} V_{i\_0}(\beta)\,, \qquad i \in PQ \tag{3.54}$$

$$\sum_{k=1}^{N} Y_{ik}^{trans} V_{k\_0}(\beta) = -jQ_{gi\_0}(\beta) W_{i\_0}^*(\beta) - \beta Y_i^{shunt} V_{i\_0}(\beta)\,, i \in PV \tag{3.55}$$

$$V_{i\_0}(\beta) * V_{i\_0}^*(\beta^*) = 1 + \beta\left(\left|V_i^{sp}\right|^2 - 1\right),\ i \in PV \tag{3.56}$$

$$V_{i_0}(\beta) = 1 + \beta(V_{slack} - 1),\ i \in slack \tag{3.57}$$

where the $V_{i\_0}(\beta = 1)$ and $Q_{gi\_0}(\beta = 1)$ represent the voltage and reactive power generation under no-load conditions respectively. The approach for obtaining the solution is similar to that presented in section 3.2, so recursion relationships for the so-called pre-reference state power flow in this section are not given.

3.3.2 Recurrence relationship

Similar to the power series calculation for the non-scalable formulation presented in section 3.2.3, the recurrence relation for the scalable formulation is obtained by equating the coefficients of the same order of α on both sides of equations (3.54), (3.55), (3.56) and (3.57). The recurrence relation is shown as follows:

$$\sum_{k=1}^{N} Y_{ik} V_k[n] = S_i^* W_i^*[n-1], i \in PQ \tag{3.58}$$

$$V_i[n] = 0, n \geq 1 \quad i \in slack \tag{3.59}$$

$$\sum_{k=1}^{N} Y_{ik} V_k[n] = (P_i + jQ_{li}) W_i^*[n-1] - j \sum_{m=0}^{n} Q_{gi}[m] W_i^*[n-m]], i \in PV \tag{3.60}$$

$$V_i[0] V_i^*[n] + V_i[n] V_i^*[0] = -\sum_{k=1}^{n-1} V_i[k] V_i^*[n-k], n \geq 1 \quad i \in PV \tag{3.61}$$

Similarly, splitting the admittance matrix into real and imaginary parts, breaking the voltage series coefficients into real and imaginary parts and moving all the knowns and unknowns to the RHS and LHS, these equations can be written in matrix form, as given in (3.62).

$$
\begin{bmatrix}
1 & 0 & \cdots & 0 & 0 & 0 & 0 & 0 & \cdots & 0 \\
0 & 1 & \cdots & 0 & 0 & 0 & 0 & 0 & \cdots & 0 \\
\vdots & \vdots & \vdots & \vdots & \vdots & \vdots & \vdots & \vdots & \vdots & \vdots \\
0 & 0 & \cdots & V_{pre}[0] & V_{pim}[0] & 0 & 0 & 0 & \cdots & 0 \\
0 & 0 & \cdots & W_{pre}[0] & -W_{pim}[0] & V_{pre}[0] & -V_{pim}[0] & 0 & \cdots & 0 \\
0 & 0 & \cdots & W_{pim}[0] & W_{pre}[0] & V_{pim}[0] & V_{pre}[0] & 0 & \cdots & 0 \\
G_{p1} & -B_{p1} & \cdots & G_{pp} & -B_{pp} & 0 & 0 & W_{pim}[0] & \cdots & G_{pq} \\
B_{p1} & G_{p1} & \cdots & B_{pp} & G_{pp} & 0 & 0 & W_{pre}[0] & \cdots & B_{pq} \\
\vdots & \vdots & \vdots & \vdots & \vdots & \vdots & \vdots & \vdots & \vdots & \vdots \\
G_{q1} & -B_{q1} & \cdots & 0 & -B_{qp} & 0 & 0 & 0 & \cdots & G_{qq} \\
B_{q1} & G_{q1} & \cdots & 0 & G_{qp} & 0 & 0 & 0 & \cdots & B_{qq} \\
\vdots & \vdots & \vdots & \vdots & \vdots & \vdots & \vdots & \vdots & \vdots & \vdots
\end{bmatrix}
$$

$$
\times \begin{bmatrix}
V_{1re}[n] \\ V_{1im}[n] \\ \vdots \\ V_{pre}[n] \\ V_{pim}[n] \\ W_{pre}[n] \\ W_{pim}[n] \\ Q_{gp}[n] \\ \vdots \\ V_{qre}[n] \\ V_{qim}[n] \\ \vdots
\end{bmatrix} =
\begin{bmatrix}
0 \\ 0 \\ \vdots \\
Re\left\{-\frac{1}{2}\sum_{k=1}^{n-1} V_p[k]V_p^*[n-k]\right\} \\
Re\left\{-\sum_{k=1}^{n-1} W_p[k]V_p[n-k]\right\} \\
Im\left\{-\sum_{k=1}^{n-1} W_p[k]V_p[n-k]\right\} \\
Re\left\{(P_p + jQ_{lp})W_p^*[n-1] - j\sum_{m=1}^{n-1} Q_{gp}[m]W_p^*[n-m]\right\} \\
Im\left\{(P_p + jQ_{lp})W_p^*[n-1] - j\sum_{m=1}^{n-1} Q_{gp}[m]W_p^*[n-m]\right\} \\
\vdots \\
Re\{S_q^* W_q^*[n-1]\} \\
Im\{S_q^* W_q^*[n-1]\} \\
\vdots
\end{bmatrix} \tag{3.62}
$$

$$
W_i[n] = -\frac{\sum_{k=1}^{n} V_i[k]W_i[n-k]}{V_i[0]} \tag{3.63}
$$

The relationship between the voltage series $V(\alpha)$ and the inverse of the voltage $W(\alpha)$ given by (3.63) will also be used to calculate the power series coefficients. The calculation process is: Calculate the reference state solution using (3.58)-(3.61) and then get the remaining terms of the power series using (3.62) and (3.63).

After obtaining all needed power series terms, similar to section 3.2.4, the Padé approximant is used to evaluate the power series outside its radius of convergence. Note

that unlike the non-scalable formulation which represents the original PF problem only at $\alpha = 1$, the solution obtained at higher values of α from the scalable formulation can represent the case when all loads and real power generation are scaled by a factor of α.When this extrapolation-capable formulation is used, the poles and zeros of the Padé approximant can be used to estimate the SNBP using the so-called roots method. Some results on the effect of high precision on the roots method are shown in section 3.4.

3.4 Numerical examples

3.4.1 Solving a power flow problem using HEM

The IEEE 14-bus system is used as an example to show the benefits of using high precision by comparing the numerical performance of the HEM using three different levels of precision: double precision, quadruple precision (34 digits) and 50 digits of precision. The MVA base is 100 MVA and the number of series terms used in this experiment is 90. The SNBP of the 14 bus system is encountered when $\alpha = 4.07$.

The maximum PBE mismatch in pu vs. the number of terms in the power series for the base case of the 14 bus system is plotted in Figure 3.1. It can be observed that, the PBE mismatch error decreases as the number of terms used in the power series increases until a limit is encountered due to precision. The best PBE mismatch obtained from double precision is at the level of 10^{-14} while using 34 or 50 digits of precision, the level of accuracy can be achieved are 10^{-33} and 10^{-49} respectively. Now for this problem at

this loading level, all levels of precision are acceptable, but for some problems the use of double precision prevents convergence.

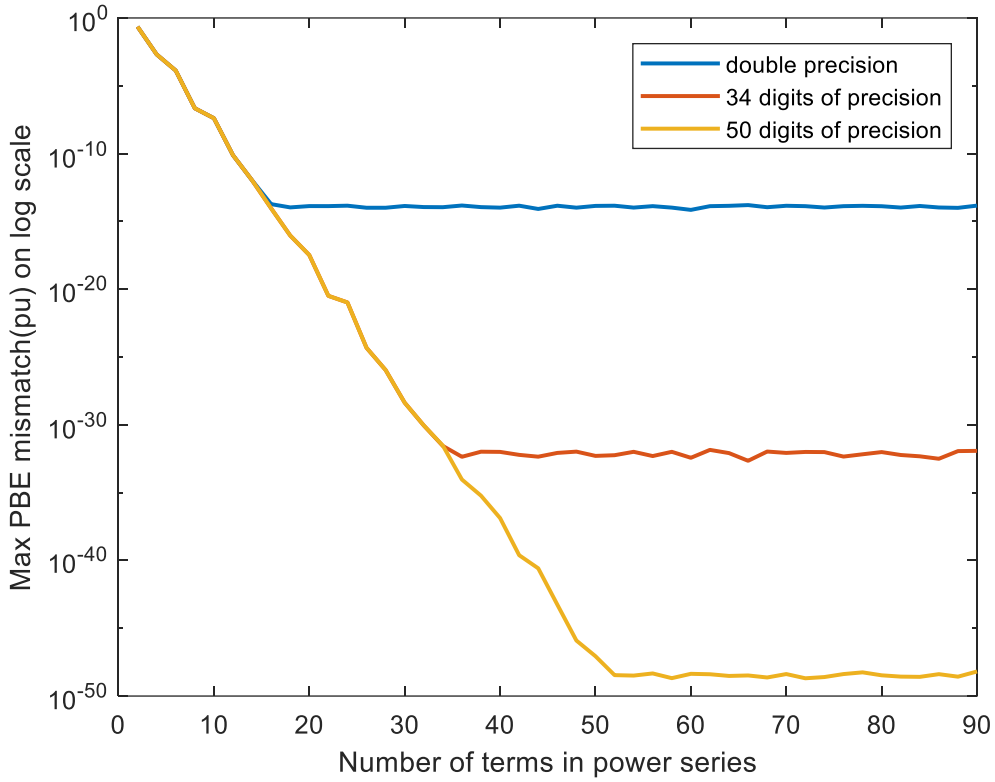

Figure 3.1 Maximum PBE mismatch vs. number of terms for the IEEE 14 bus system at base case

When all loads and real power generation of the 14 bus system are scaled by a factor of 4, so that the system is loaded to 98.3% of its SNBP, the convergence rate as shown in Figure 3.2 is much slower as compared to the base case as seen in Figure 3.1. When using double precision as represented by the blue solid line, the rate of the convergence decreases after the number of series terms reaches n=40, which indicates that the accumulated round-off errors due to limited precision start to impact the accuracy of the PF results at this point. However, the PF solution can continue converging at almost

the same rate when higher precision (34 digits or 50 digits of precision) is implemented. At n=90, the PBE mismatch for double precision is around 1×10^{-5} pu while for 34 or 50 digits of precision, the PBE mismatch is around 2×10^{-8} pu.

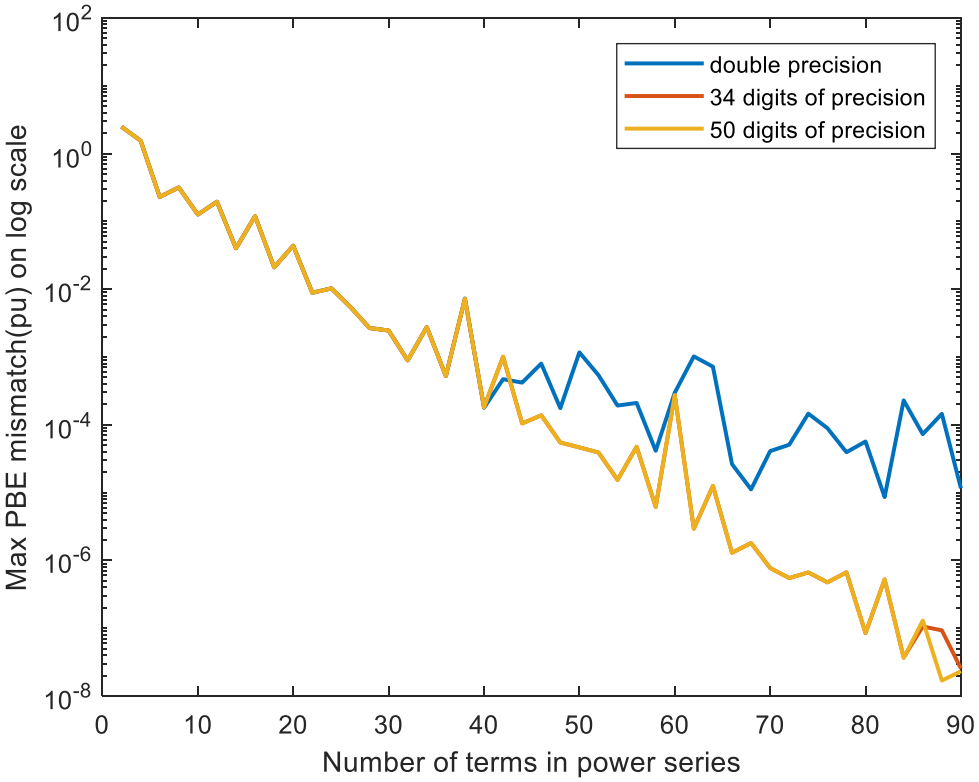

Figure 3.2 Maximum PBE mismatch vs. number of terms for the IEEE 14 bus system at load scaling factor=4

If the PF mismatch tolerance is set to be 10^{-5} pu (0.001 MVA), the number of terms needed to converge within the given tolerance for these three different levels of precision is plotted against the load scaling factor (expressed as the percentage of the SNBP) when the 14 bus system is heavily loaded, as given in Figure 3.3. It can be observed that as the load increases, more number of terms are needed to reach the mismatch tolerance.

When the system is loaded to 98% of its SNBP, the number of terms needed for double precision and higher precision (34 or 50 digits of precision) are 49 and 59 terms, respectively. When the system is loaded to 98.5% of its SNBP, the MATLAB program with double precision cannot find the solution within 90 terms while the program with higher precision (34 or 50 digits of precision) can find the solution with 55 terms included in the power series.

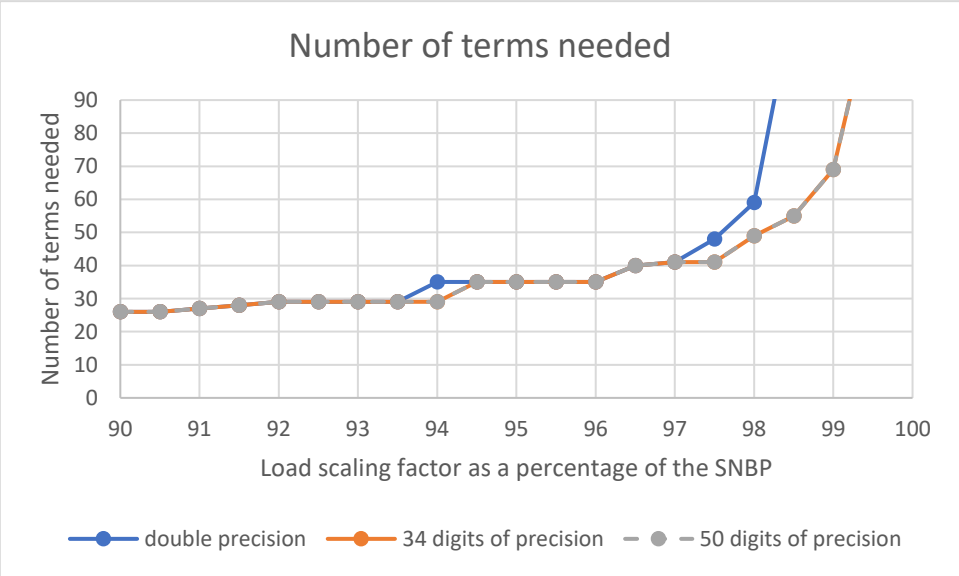

Figure 3.3 Number of terms needed vs. load scaling factor

It can be concluded from the above figures that the implementation of high precision is able to improve the accuracy of computations especially when the system is close to the voltage collapse point. As shown in Figure 3.3, with higher precision, fewer number of terms are needed. However, the speed of the program typically would be slower. Thus, there exists a trade-off between the accuracy and execution time. Determining how many terms are needed and how many digits of precision must be used remains an open question.

3.4.2 Estimating the SNBP using roots method

In the roots method [26], the scalable formulation is used to estimate the SNBP using the poles/zeros of the Padé approximant. The smallest positive-real-valued zero or pole is viewed as the estimation of the SNBP.

A simple two-bus system comprised of a slack bus and a PQ bus as shown in Figure 3.4 is used to demonstrate the effect of high precision on roots method, since the theoretical SNBP can be obtained as a reference. The parameters for this two-bus system are listed in Table 3.2.

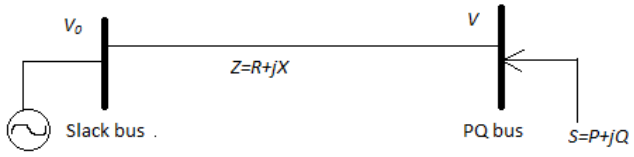

Figure 3.4 Two bus system diagram

Table 3.2 Parameters for the two-bus system

Parameter	R	X	P (injection)	Q(injection)	V_0
Value (pu)	0.0	0.1	-0.15	-0.5	1.0

The PBE for the PQ bus (bus 2) when the load and generation are scaled uniformly by a loading scale factor x is given by (3.64),

$$\frac{V - V_0}{Z} = \frac{S^*_{scaled}}{V^*} \tag{3.64}$$

where V is the PQ bus voltage, V_0 is the slack bus voltage, $Z = R + jX$ is the line impedance and $S_{scaled} = x \times S = x \times (P + jQ)$ is the complex power injection at the PQ bus.

It is convenient to introduce a variable U given by (3.65) and define $\frac{ZS^*_{scaled}}{|V_0|^2} = \sigma$, the PBE equation (3.64) can be rearranged to obtain (3.66).

$$U = \frac{V}{V_0} \tag{3.65}$$

$$U = 1 + \frac{\sigma}{U^*} \tag{3.66}$$

The solutions for (3.66), which is a quadratic equation, can be obtained in closed form:

$$U = \frac{1}{2} \pm \sqrt{\frac{1}{4} + \sigma_R - {\sigma_I}^2 + j\sigma_I} \tag{3.67}$$

where $\sigma_R = \frac{x(XQ+RP)}{|V_0|^2}$ and $\sigma_I = \frac{x(XP-RQ)}{|V_0|^2}$ are the real and imaginary parts of σ, respectively.

These two solutions represent the high-voltage and low-voltage solutions for the two-bus network. The SNBP is the point where the two "branches" meet and that is the point at which the radicand becomes zero. Thus, the SNBP can be calculated by solving the equation shown below:

$$\frac{1}{4} + \sigma_R - {\sigma_I}^2 = 0 \tag{3.68}$$

Substituting parameter values into (3.68), we obtain:

$$\sigma_R = \frac{x(XQ + RP)}{|V_0|^2} = -0.05x$$

$$\sigma_I = \frac{x(XP - RQ)}{|V_0|^2} = -0.15x \tag{3.69}$$

$$\frac{1}{4} + \sigma_R - {\sigma_I}^2 = 9x^2 + 20x - 100 = 0$$

$$x = 2.4025, -4.6248$$

Thus, the exact SNBP (to 5 significant digits) is 2.4025.

When using the scalable formulation to solve this two-bus system using 101 terms with double precision, the poles/zeros obtained from the Padé approximant are shown in Figure 3.5 plotted in the complex plane. While, theoretically, all poles/zeros that *characterize the equation system* should be purely real, precision limitations lead to small imaginary parts. Thus, all poles/zeros obtained numerically are expected to approach the real axis with insignificant imaginary parts. However, as seen in the pole-zero plot of Figure 3.5 when using double precision, there are many spurious pole-zero pairs (Froissart doublets) accumulating on a circle centered at the origin of radius equal to the ROC of the series, which for this problem is the SNBP. In Figure 3.5, the pole/zero that is "near" the real axis and that has the smallest positive real part is the point located at $(2.411, -3.872 \times 10^{-5})$, which would be taken as the estimate of the SNBP. Therefore, the SNBP obtained from roots method with double precision is 2.411, which is quite accurate (to within 0.354%). Note that there is a spurious pole-zero pair at about $\alpha = 1.69$. The corresponding imaginary-to-real part ratio is 0.0969 so this pole-zero pair might be considered to be close enough to the real axis if the tolerance of the imaginary part is selected to be "too large". In that case, roots method would give an incorrect estimation. The position of spurious poles is random and so, using a different order of the Padé approximant may eliminate any particular spurious poles/zero pair, or may create one even closer to the real axis.

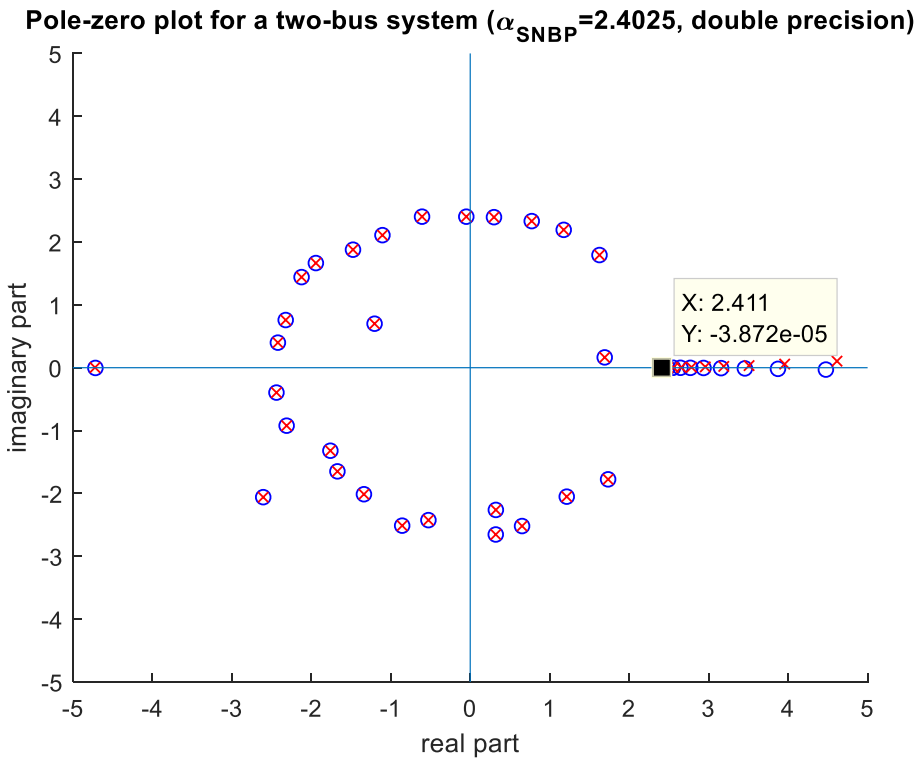

Figure 3.5 The two-bus system pole-zero plot for [50/50] Padé approximant with double precision

While using 200 digits of precision to obtain the poles/zeros of the Padé approximant as shown in Figure 3.6, the spurious-root circle caused by the double-precision limitation as seen in Figure 3.5 disappears and all poles/zeros are much closer to the real axis. The estimated SNBP is 2.406, which is in error by only 0.14%.

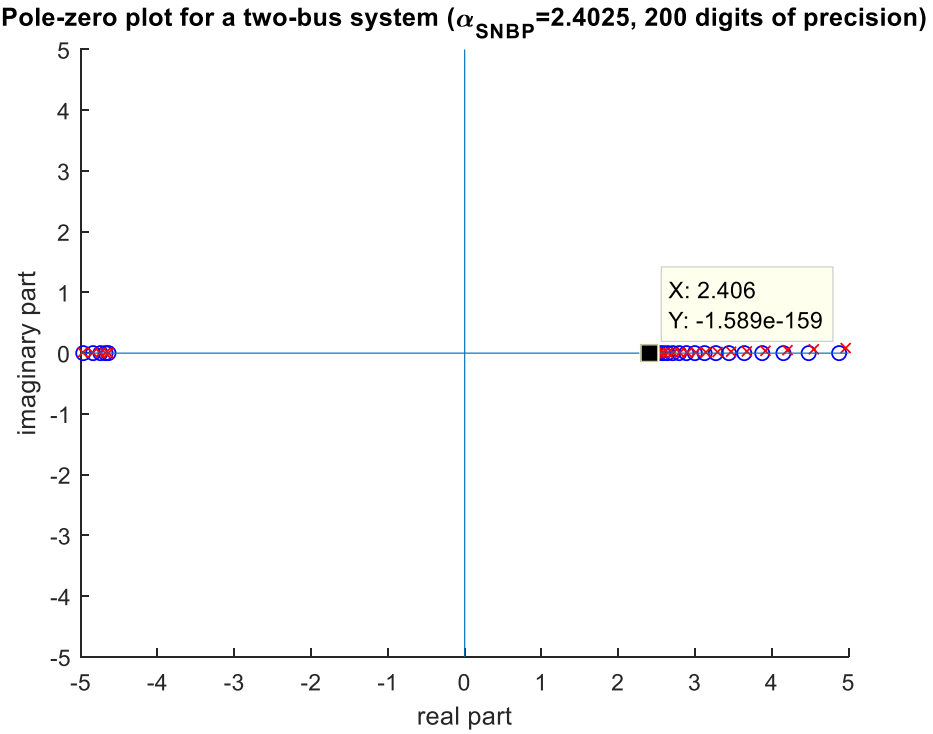

Figure 3.6 The two-bus system pole-zero plot for [50/50] Padé approximant with 200 digits of precision

In [50], the exact location of those zeros for a simple two-bus system case can be obtained through derivation, as shown in (3.70):

$$z_k = \frac{1}{2\left(|\sigma| cos\left(\frac{\pi k}{n+1}\right) - \sigma_R\right)}, k = 1,2, \dots n \tag{3.70}$$

where n is the degree of the numerator polynomial in the Padé approximant which must include n zeros and k represents the kth one in that family of zeros.

To validate the implementation used in this work, the following numerical experiment was conducted on the above two-bus system. In this experiment, 101 terms of power series were calculated and then used to solve for a [50/50] Padé approximant. Thus, the n in (3.70) in this case is 50. The "exact" zeros computed using the above

equation are plotted in Figure 3.7. It can be observed that the zeros obtained from roots method using 200 digits of precision as shown in Figure 3.6 match closely the zeros shown in Figure 3.7, at least visually. The numerical comparison of the zeros values between the true zeros from the theory in (3.70) and that computed with double precision and 200 digits of precision are provided in Table 3.3. The first ten zeros on the positive real axis (listed in order from nearest to farthest from the origin) are listed in that table. As expected, the values of zeros calculated with 200 digits of precision are much closer to the exact values than those obtained using double precision. The imaginary parts of the smallest ten zeros when using 200 digits of precision are also much smaller than when using double precision, with all magnitudes less than 10^{-156}.

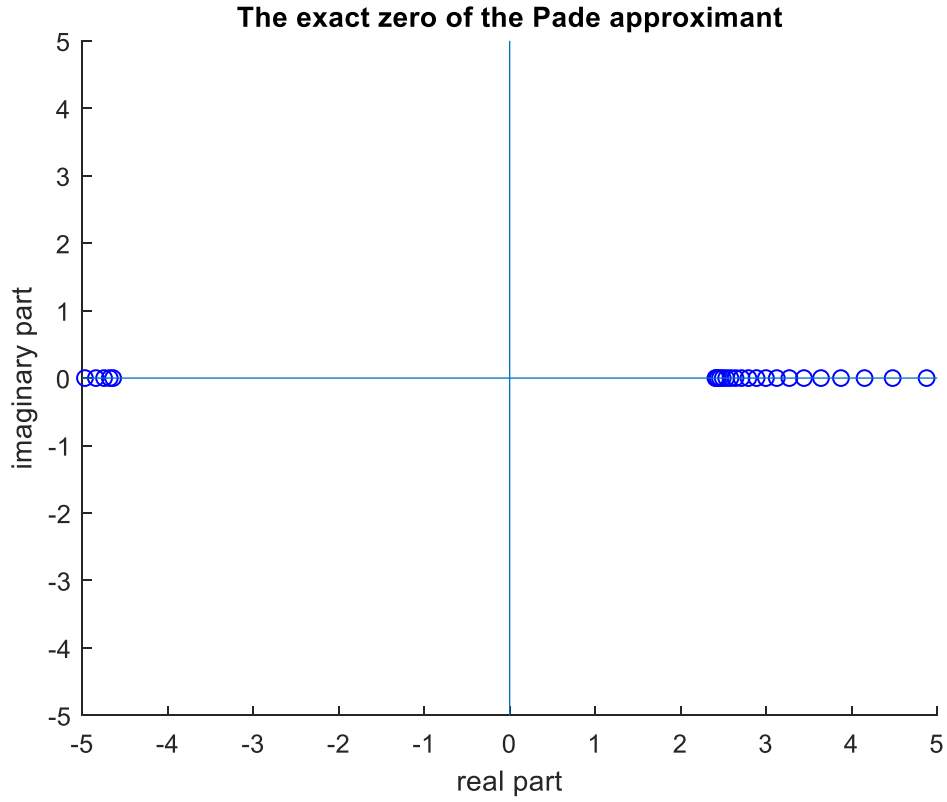

Figure 3.7 The exact zeros of the [50/50] Padé approximant for the 2-bus system

Table 3.3 The zeros on the positive real axis for the two-bus system

No.	Zeros (from	200 digits of precision		Double precision	
		Re(zero)	Im(zero)	Re(zero)	Im(zero)
1	2.4060	2.4060	-1.59×10^{-159}	2.4113	-3.87×10^{-5}
2	2.4164	2.4164	-6.41×10^{-159}	2.4380	-1.66×10^{-4}
3	2.4340	2.4340	-1.46×10^{-158}	2.4840	-4.15×10^{-4}
4	2.4590	2.4590	-2.65×10^{-158}	2.5516	-8.47×10^{-4}
5	2.4916	2.4916	-4.25×10^{-158}	2.6449	-0.0016
6	2.5325	2.5325	-6.31×10^{-158}	2.7698	-0.0027
7	2.5821	2.5821	-8.92×10^{-158}	2.9354	-0.0045
8	2.6413	2.6413	-1.22×10^{-157}	3.1563	-0.0072
9	2.7110	2.7110	-1.62×10^{-157}	3.4556	-0.0116
10	2.7925	2.7925	-2.11×10^{-157}	3.8720	-0.0185

As shown above, the roots method implemented with high precision is able to predict the SNBP more accurately and provide more accurate roots of the Padé approximant. From this example and some previous experiments [51], it was observed that the roots method worked well for predicting the SNBP with double precision on the systems tested provided a reasonable number of series terms was used. However, it has been observed when the system is heavily loaded, a greater number of terms are needed to achieve the same accuracy and the occurrence of spurious pole-zero pairs due

to limited precision might affect the ability of the roots method. In that case, using high precision will play an important role in achieving higher accuracy.

4 EXPLORING THE EFFECT OF HIGH PRECISION ON THE HEM ALGORITHM

4.1 Investigation of precision loss in the HEM algorithm

4.1.1 Precision tests

HEM is theoretically guaranteed to converge provided Stahl's conditions are satisfied. However, the limitation of machine precision can affect the numerical performance as shown in chapter 3. To further investigate in which part of the algorithm the loss of precision is most critical, different precision levels were assigned to different aspects of the HEM algorithm. (We only considered the non-scalable formulation in these numerical experiments.) There exist three places in the HEM algorithm that might accumulate roundoff error during the calculations:

1) Matrix equation solution calculation

In (3.25) and (3.28), the LU factorization of *Y* matrix needs to be performed to calculate voltage series coefficients. Though one LU factorization might not have significant effect on the precision issues in the calculation, the round-off errors in the series coefficients can accumulate because the n^{th} coefficients of voltage series, $V[n]$, are calculated based on $V[n-1]$ using a recurrence relationship. One aspect of the experiments will involve limiting and then enhancing the precision involved in both the factorization and forward/backward substitution phases of the matrix solution. This precision experiment will also reveal any sensitivities to an ill-conditioned *Y* matrix,

which occurs if some branch impedances are much larger or smaller than those of the rest of a system.

2) Calculating the inverse of the voltage power series

To solve for the series coefficients, we introduced a power series $W(\alpha)$, which represents the inverse of the voltage power series as defined in (3.12). The $W(\alpha)$ has to be calculated using the convolution of two power series as shown in (3.32). When the nested convolutions are performed in the process of obtaining the power series coefficients, roundoff error may accumulate.

3) Calculating the numerator/denominator of the Padé approximant

One drawback of the matrix method for calculating the Padé approximant is that as more series terms are included to create a higher-order Padé approximant, the Padé matrix shown in the LHS of (3.41) becomes increasingly more ill-conditioned. The rule of thumb recommends that M guarding digits are usually needed to maintain accuracy for a [L/M] Padé approximant [27].

4.1.2 Precision experiment description

We explore which of the three parts of the HEM algorithm listed above has the most significant effect on solution accuracy by limiting each calculation to 16 digits of precision while the rest of the calculations are performed using higher precision (86 digits of precision in this experiment) and observing which precision-limiting part of algorithm is most severely affecting solution accuracy. For comparison we also show

the accuracy performance when all three-phases of the calculation listed above are completed with 16 digits or 86 digits of precision.

4.1.3 Numerical results on the IEEE 14 bus system

4.1.3.1 The 14 bus system base case

The above described precision limiting tests were conducted on the IEEE 14 bus system. The system load of the base case is 24.57% of the SNBP (estimated at load-scaling factor=4.07, using CPF). The largest PBE mismatches in pu were plotted on a log scale against the number of terms used in the power series as shown in Figure 4.1. The curves labeled 1) “Matrix solution with 16 digit”, 2) “Series inversion with 16 digit” and 3) “Padé approximant with 16 digit” represent the PBE mismatch results when running the entire HEM PF program with 86 digits of precision but 1) using limited 16 digits of precision to perform matrix equation solutions, 2) calculation of the inverse of the power series and 3) calculation of Padé approximant respectively. The labels “All with 86 digit” and “All with 16 digit” stand for the performing all arithmetic with 86 digits and 16 digits precision respectively. The same figure legends will be used for the subsequent figures in this chapter. The voltage solutions obtained by using 86 digits of precision for all calculations in the HEM PF are regarded as the “true” values. The voltage results obtained using lower precision, i.e., 16 digits of precision (either used in only one part of the algorithm or the entire program) were compared with the “true” values and the corresponding maximum voltage errors obtained by considering the

errors of all buses in the model are plotted in Figure 4.2 against the number of terms in the power series.

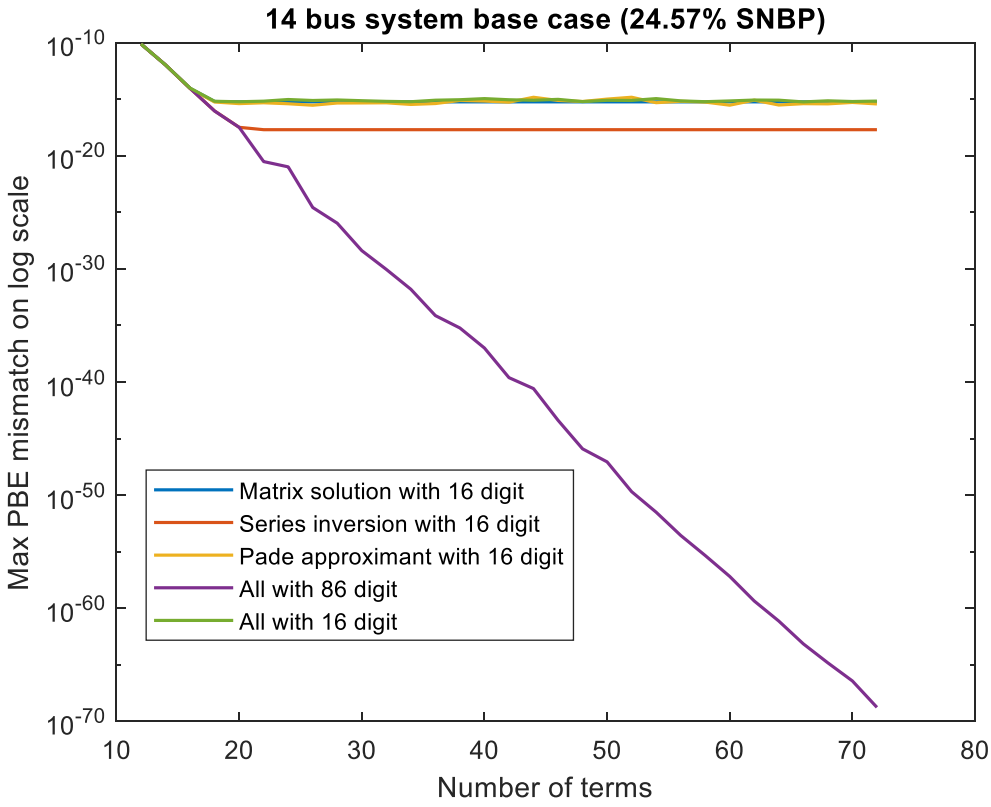

Figure 4.1 Maximum PBE mismatch vs. number of terms in series for the 14 bus system base case

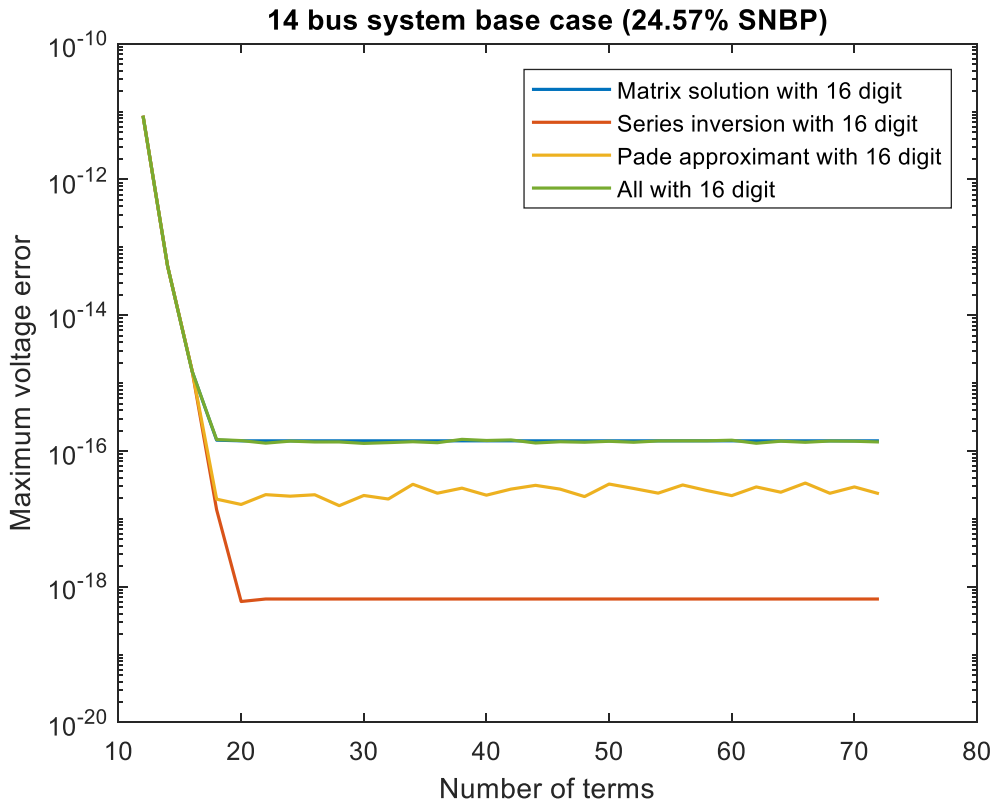

Figure 4.2 Maximum voltage error vs. number of terms in series for the 14 bus system base case

It is observed from Figure 4.1 and Figure 4.2 that for the base case of IEEE 14 bus system, the effects of limited precision on different aspects of the algorithm had a different effect on solution accuracy, as expected. The order of the numerical performance from best to worst (i.e., least to most effect from reduced (16-digit) precision) when limiting one part of the algorithm to lower precision is: Series inversion > Padé approximant > Matrix solution. Therefore, the priority order (more to less important) for assigning increased precision to the aspects of the HEM PF are: Matrix solution > Padé approximant > Series inversion.

The matrix equation solution calculation is shown to cause the most precision loss in the solution; next the algorithm is most sensitive to precision of the Padé approximant, which is counter-intuitive. As we know, when computing the Padé approximant, there can be ill-conditioned problems where small variations in the power series coefficients might lead to huge variations in the Padé approximant coefficients. However, it is shown in [28] and [29] that though the relative errors in the numerator and denominator polynomial coefficients increase as the number of terms, n, increases, the relative errors in the computed Padé approximant is virtually unaffected, if n and α are not too large. This occurs because the ratio of the error in numerator and the error in denominator itself is a reasonable approximation to the Padé approximant [28]. In other words, one can expect to get a reasonably good voltage solution from the Padé approximant even though the coefficients of the denominator and numerator contain some roundoff errors. If we use different levels of precision to calculate the power series (involving both the matrix calculation and power series inversion) and the Padé approximant and then compare the coefficients in numerator and denominator of the Padé approximant and the voltage solutions with their respective "true" values obtained from extremely high precision (250 digits of precision in this experiment), the results we obtained are given in Table 4.1 and

Table 4.2. The number of series terms used here was 32. From Table 4.1 and

Table 4.2, we can observe that the voltage solutions obtained from limited precision are much more accurate than the Padé approximant coefficients, which is consistent with the findings in [28] and [29]. For example, when using 64 and 56 digits of precision to compute the power series and the Padé approximants, respectively, the numerator/denominator coefficient of the Padé approximant matches to 46 digits when compared with its "true" value while the voltage solution can preserve 56 digits of precision.

Table 4.1 Number of "matched-up" digits for Padé coefficients (worst case)

Padé approximant	Power series				
	16 digits	32 digits	56 digits	64 digits	86 digits
16 digits	4	5	5	5	5
32 digits	4	20	22	22	22
56 digits	4	20	44	46	46
64 digits	4	20	44	52	54
86 digits	4	20	44	52	74

Table 4.2 Number of "matched-up" digits for voltage solutions (worst case)

Padé approximant	Power series				
	16 digits	32 digits	56 digits	64 digits	86 digits
16 digits	15	16	16	16	16
32 digits	15	31	32	32	32

56 digits	15	31	55	56	56
64 digits	15	31	55	63	64
86 digits	15	31	55	63	85

The maximum condition number of the Padé coefficient matrices over all buses for IEEE 14 bus system is plotted in Figure 4.3 versus the number of terms included in the power series. The condition number we used here and in subsequent sections in the chapter is the 2-norm condition number, defined as the ratio of the largest to smallest singular values. It is observed that, after around 42 terms, the condition number obtained (calculated using 86 digits of accuracy) when one or all of the three parts of HEM algorithm are executed using 16 digits of precision does not match the condition number calculated when 86 digits of precision are used for the entire HEM PF. This is caused by the accumulated roundoff error in Padé coefficient matrix, either due to the inaccuracy of computed power series using limited precision or the roundoff error generated in the Padé approximant calculation. In some sense, with limited precision, the Padé approximant cannot represent the original system and thus some characteristics are lost.

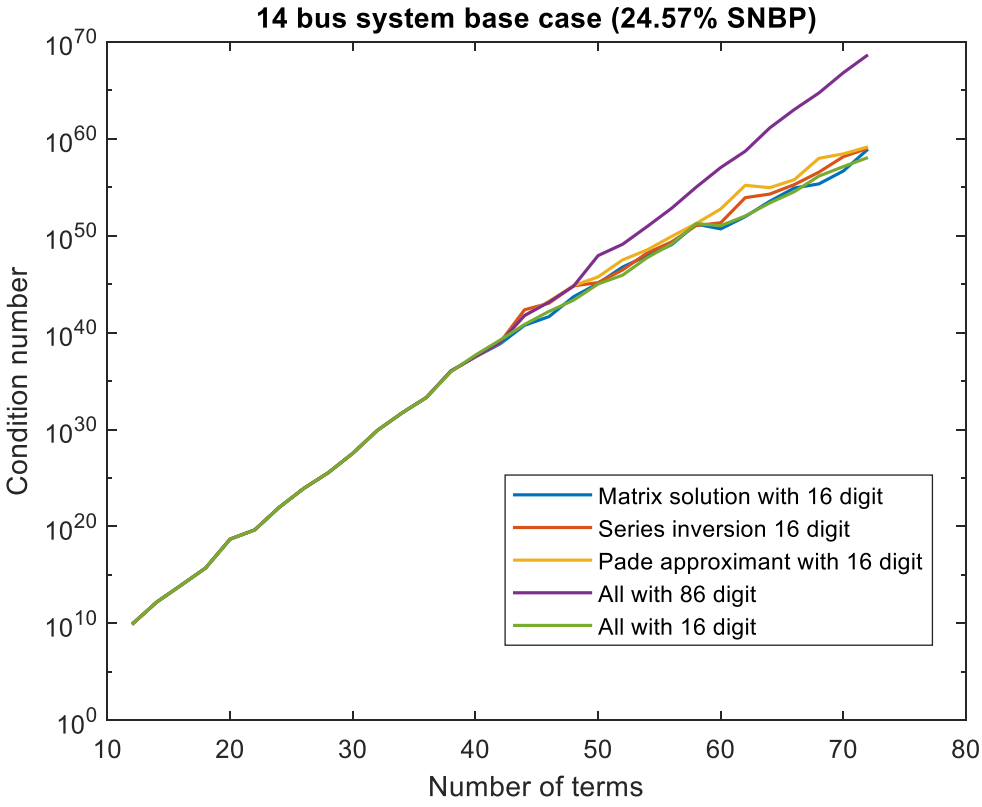

Figure 4.3 Maximum condition number vs. number of terms in series for the 14 bus system base case

4.1.3.2 The 14 bus system near the SNBP

When the 14 bus system is loaded to 98% of its SNBP, the behavior of PBE mismatch and voltage error as number of terms increases are shown in Figure 4.4 and Figure 4.5, respectively. The voltage solution is calculated using [M/M+1] Padé approximant. It is shown that when the system is close to its SNBP, limiting precision in any one part of the algorithm has a similar effect. We can also observe that the convergence rate is much slower as compared to the base case as described in section 4.1.3.1.

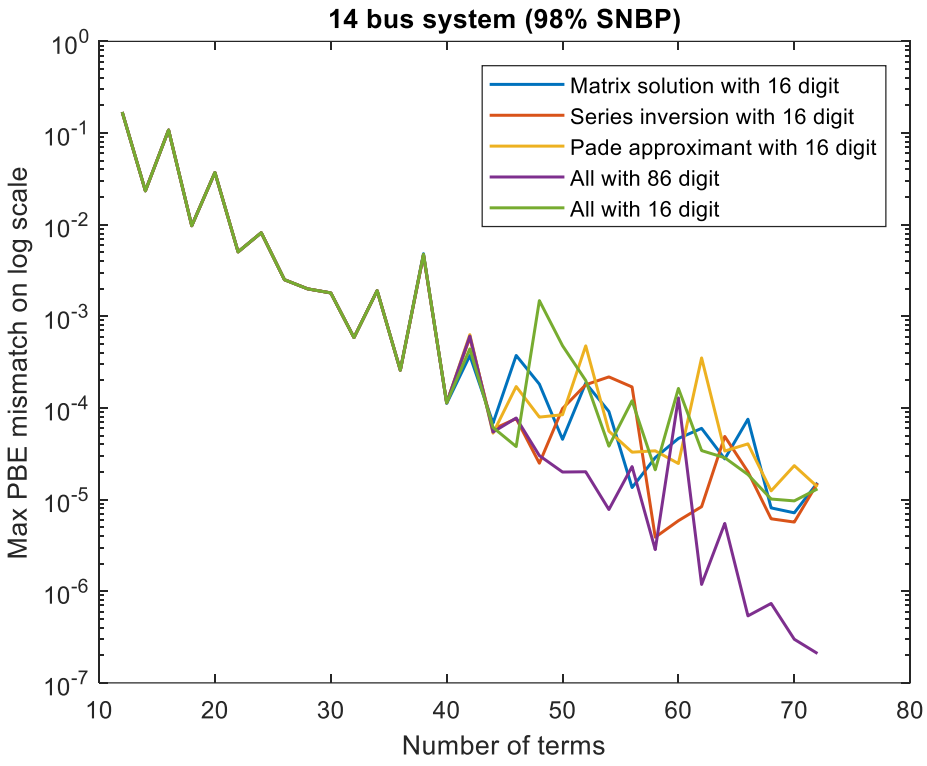

Figure 4.4 Maximum PBE mismatch vs. number of terms in series for the 14 bus system loaded to 98% of its SNBP

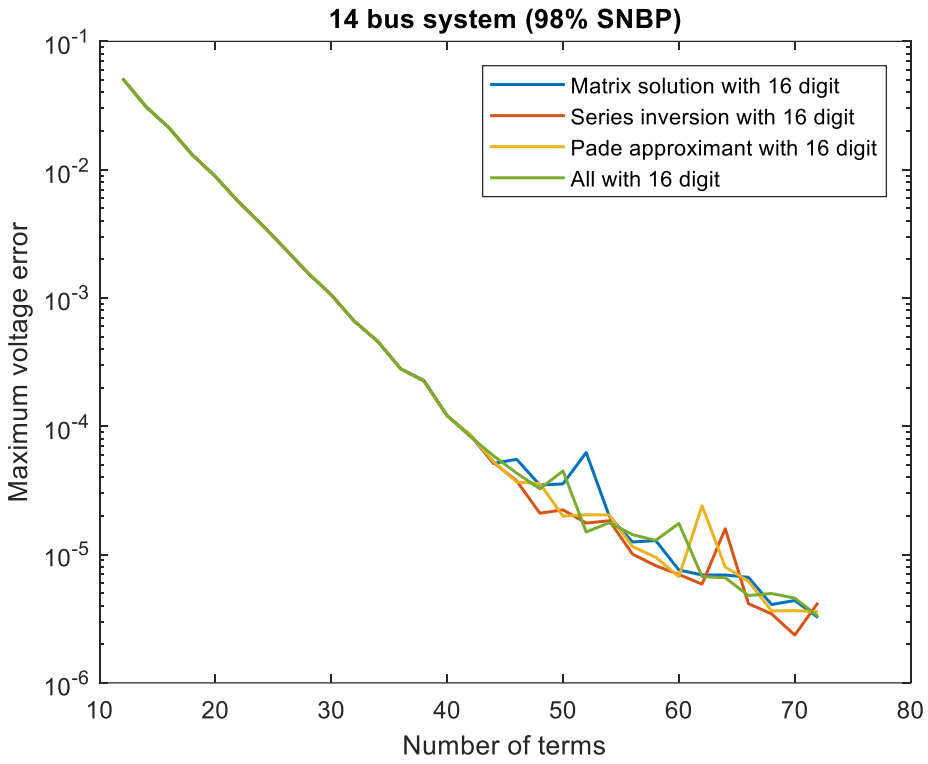

Figure 4.5 Maximum voltage error vs. number of terms in series for the 14 bus system loaded to 98% of its SNBP

Figure 4.6 shows the maximum condition number of the Padé coefficient matrices over all buses for this 14 bus system. As shown in Figure 4.6, the breakpoint in the geometric behavior of the condition number occurs at around 46 terms and after the breakpoint, each line that represents the limiting precision in one or all of the three aspects appears to be relatively flat. In other words, the condition number seems to remain constant as the number of terms increases.

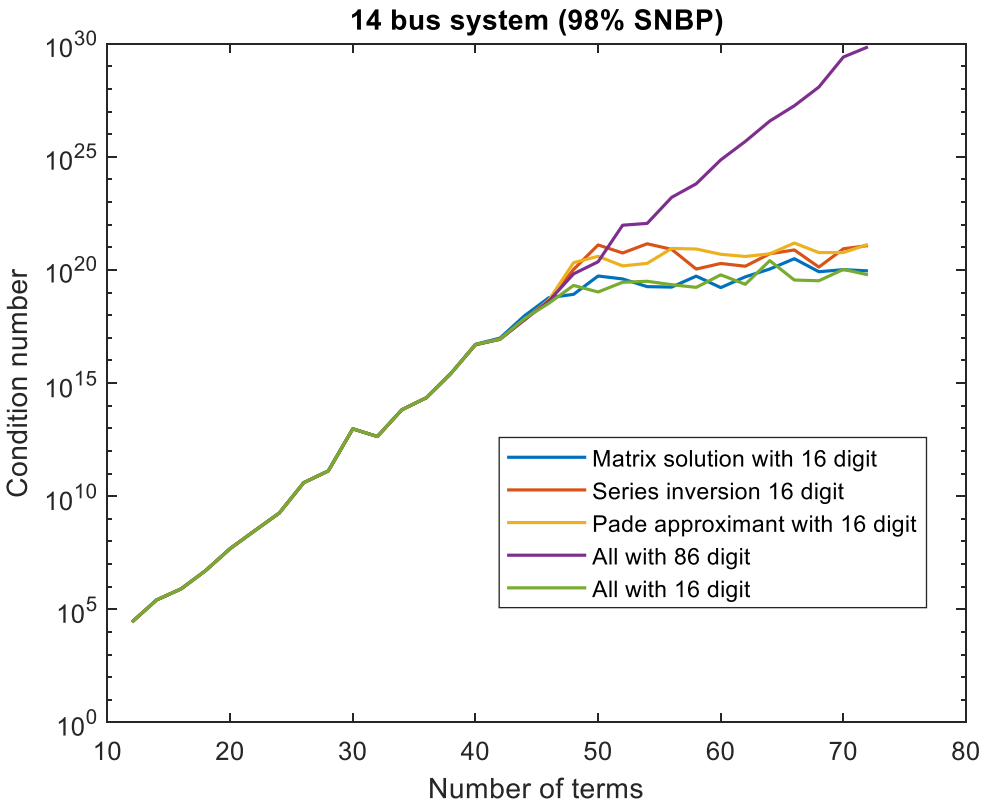

Figure 4.6 Maximum condition number vs. number of terms in series for the 14 bus system loaded to 98% of its SNBP

4.1.3.3 The 14 bus system at different loading conditions

The condition number for the 14 bus system at different loading conditions (24.57%, 50%, 75%, 85% and 98% of the SNBP loading) when using 16 digits or 86 digits of precision everywhere in the algorithm was plotted in Figure 4.7. It is seen that as the system load increases, the condition number decreases. Also, the difference in the behavior of condition number of the Padé matrices when using 16 digits of precision versus 86 digits of precision for each loading condition beyond the breakpoint has an interesting behavior. The angle between the two lines increases as load increases, which means the roundoff error due to precision limitations has a more significant effect as

the load increases. The difference in the condition number value for different loading conditions might be related to the properties of power series coefficients. Figure 4.8 shows the magnitude of power series coefficients for bus number 2 at different loading scaling values given in percentage of the SNBP.

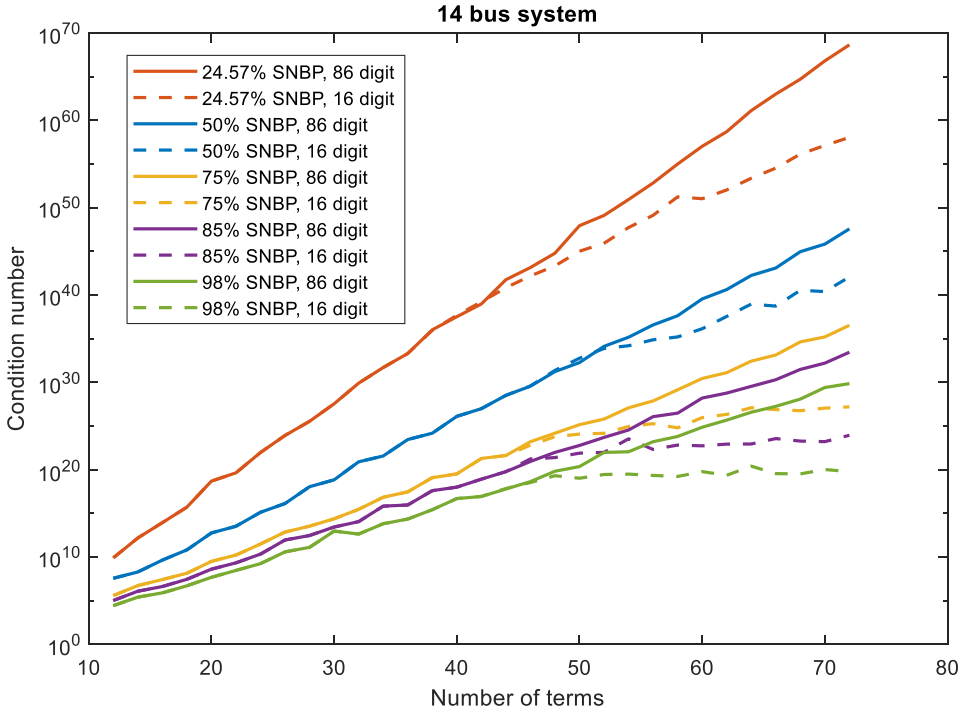

Figure 4.7 Maximum condition number vs. number of terms in series for the 14 bus system at different loading conditions

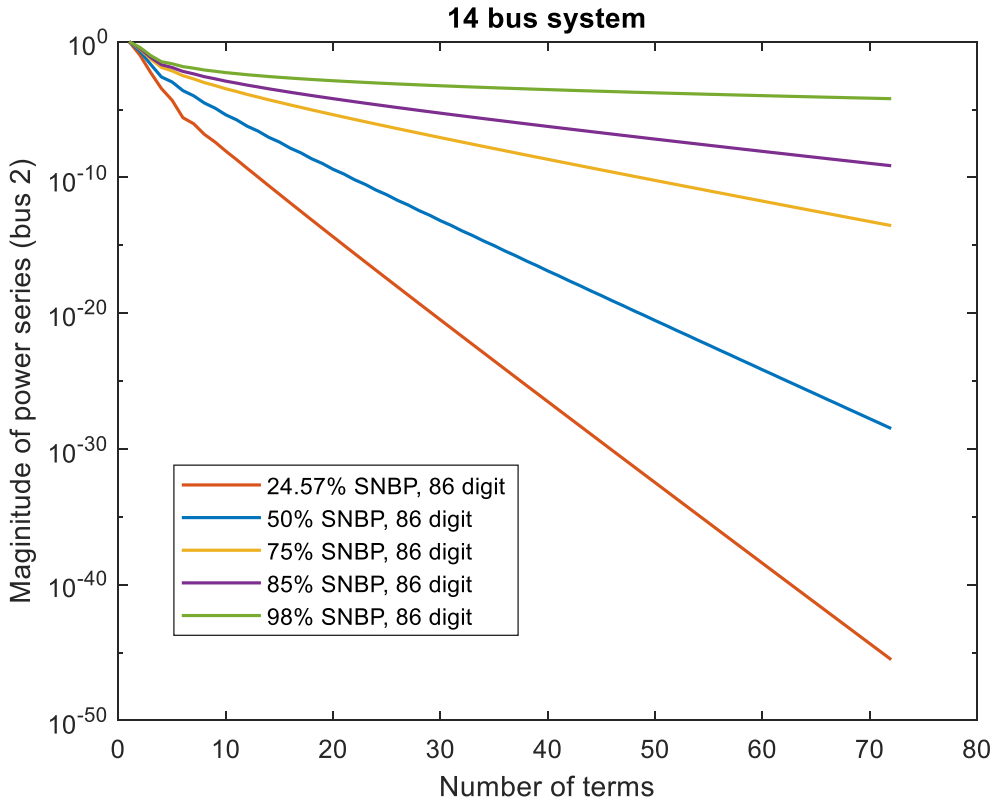

Figure 4.8 Magnitude of power series vs. number of terms in series for the 14 bus system at different loading conditions

4.1.4 Conclusion

The HEM algorithm is broken into three distinct calculation procedures where the roundoff error might accumulate in different ways and at different rate: matrix (equation solution) calculation, series inversion and Padé approximant calculation. The numerical tests on the IEEE 14 bus system show that limiting precision in any one of the above aspects has a similar effect. This numerical experiment was also conducted on IEEE 30 bus system and IEEE 118 bus system and similar results were observed (not shown). The conclusion reached is that one must increase precision everywhere in the program to improve numerical performance.

4.2 Convergence issues for the 43 bus system

An ill-conditioned 43 bus system [30] is used to test the numerical performance of the HEM method using the non-scalable formulation. The system has large R/X ratio branches and is heavily loaded. The loading level of the system is 98.15% of its SNBP loading. The SNBP of the 43 bus system is at $\alpha = 1.018$, obtained using HEM and the roots method while using 16 digits of precision in this calculation. The maximum PBE mismatch with double precision is plotted in Figure 4.9 against the number of terms used in the power series. It can be observed that the HEM PF with double precision (16 digits) tends toward convergence early on in the recursion procedure but then fails to converge after 30 terms. The smallest mismatch (taken from the set of the largest mismatches over all buses in the system over number of series terms from 12 to 92) obtained was 5×10^{-5} pu.

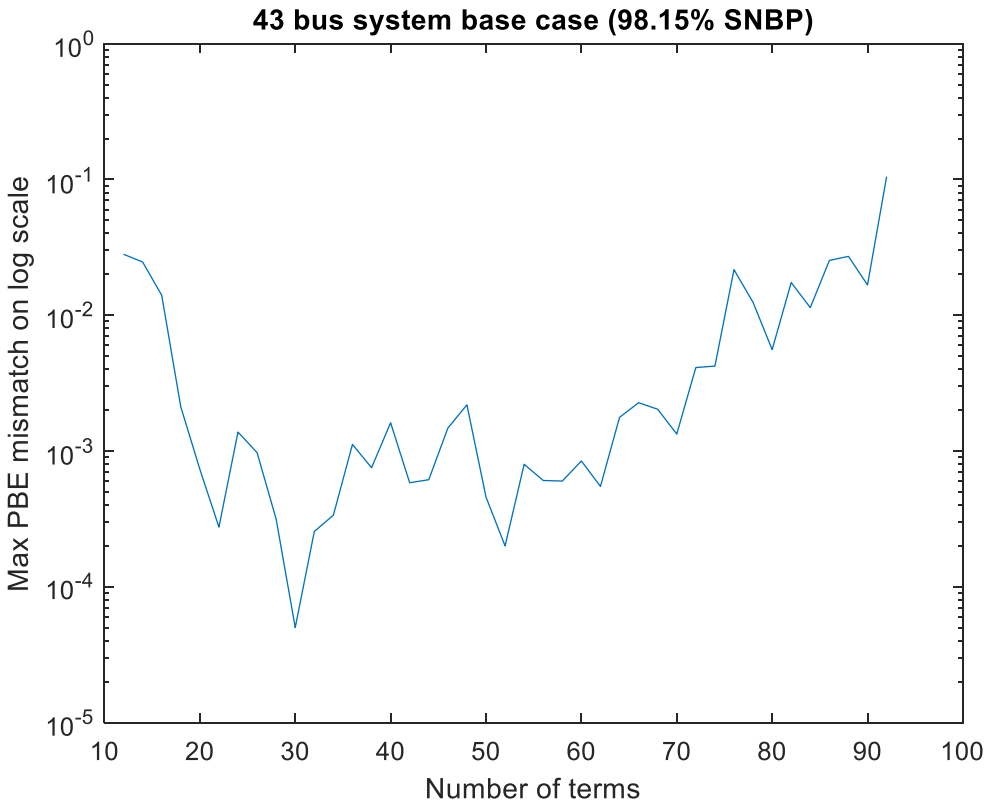

Figure 4.9 Maximum PBE mismatch vs. number of terms in series for the 43 bus system with double precision

4.2.1 Using high precision to enhance numerical performance

One can increase precision to improve the numerical performance of HEM. As shown in Figure 4.10, the PF solution with 86 digits of precision can converge as the number of terms increases. The PBE mismatch error can be as small as 10^{-15} pu with a maximum of 112 terms.

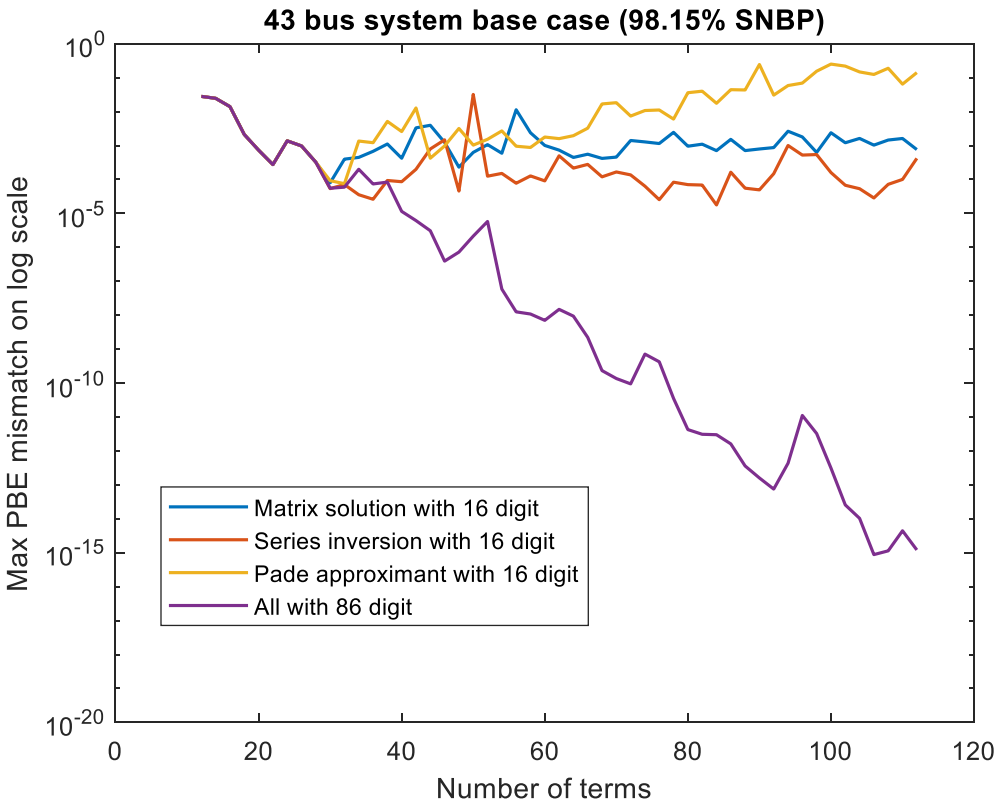

Figure 4.10 Maximum PBE mismatch vs. number of terms in series for the 43 bus system when implementing different precision to each part of HEM algorithm

The voltage error and condition number for the 43 bus system are shown in Figure 4.11 and Figure 4.12, respectively. It is observed that the precision limitations in any aspect of the problem causes the convergence to stall. Precision limitations in the calculation of the Padé approximant (the yellow solid line in Figure 4.11 and Figure 4.12) in particular lead to severe loss of precision and divergence in the Padé approximant after around 70 terms. This indicates that the Padé approximant might be the weakest place in HEM algorithm if a large number of terms are used.

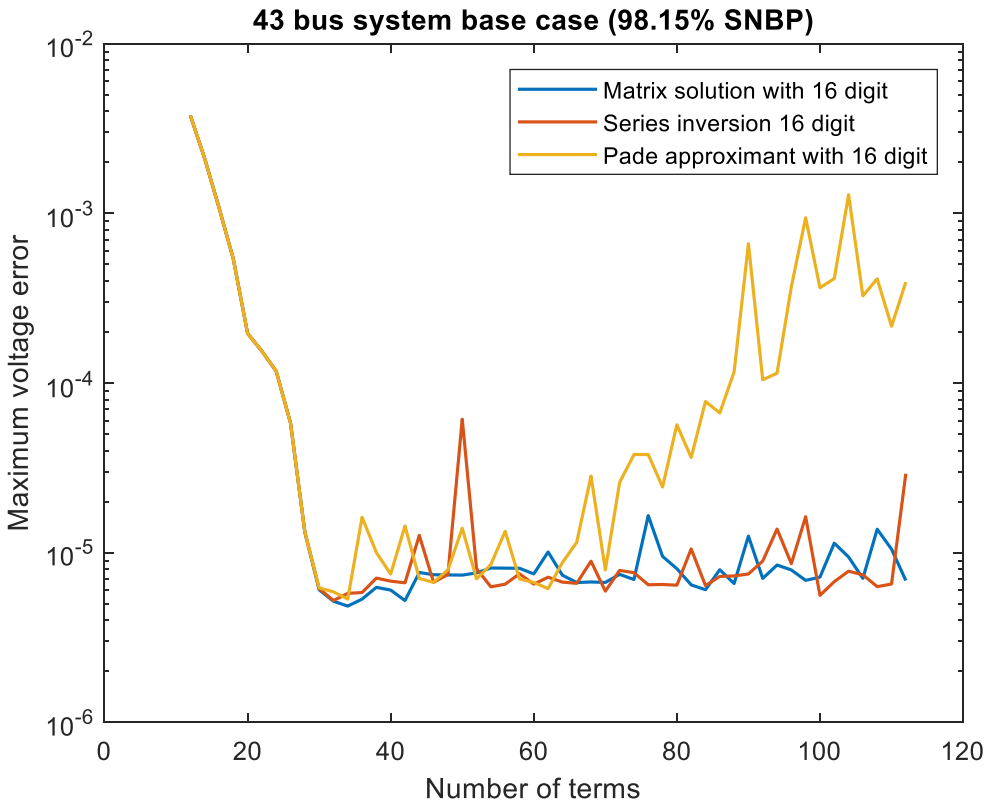

Figure 4.11 Maximum voltage error vs. number of terms in series for the 43 bus system when implementing different precision to each part of HEM algorithm

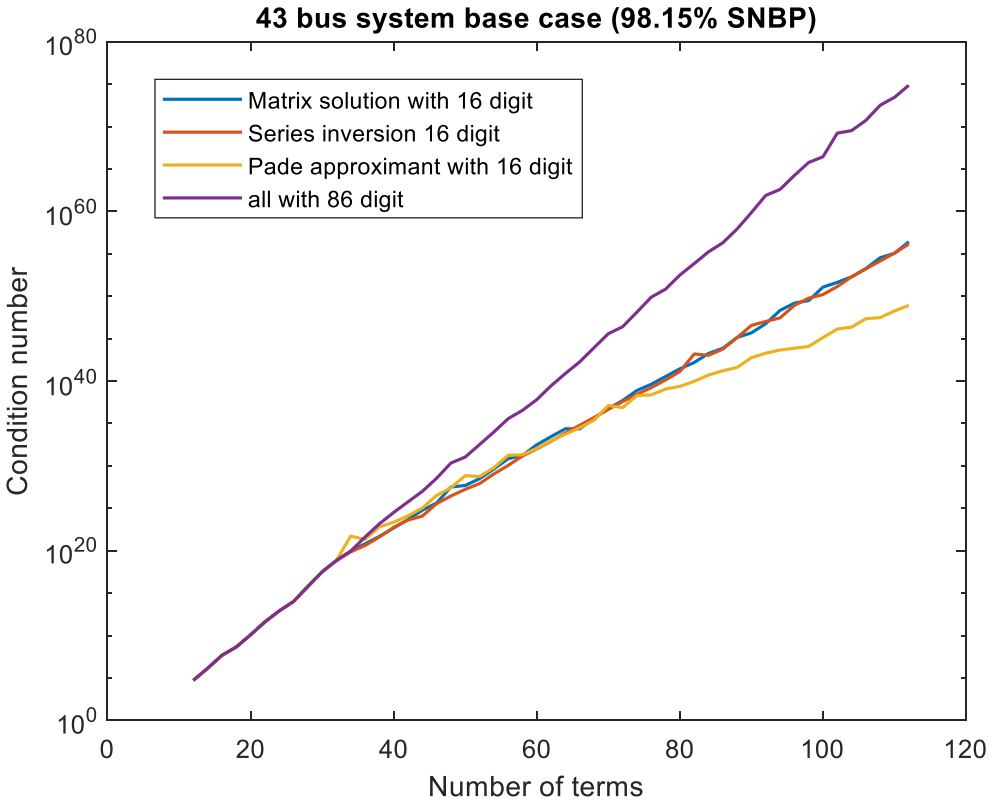

Figure 4.12 Maximum condition number vs. number of terms in series for the 43 bus system when implementing different precision to each part of HEM algorithm

4.2.2 Using Padé-Weierstrass technique to enhance numerical performance

Though using higher precision can improve the numerical performance, it could be computationally expensive. The Padé-Weierstrass (P-W) method proposed in [31] can be an alternative. This method allows one to calculate the power series in several steps using conformal mapping. At each stage, one can obtain an accurate partial solution at a value $0 < \alpha_0 < 1$. Then the calculation procedure is repeated recursively until one is able to get a converged solution at $\alpha = 1$ at some P-W stage, k. For example, if the parameter α_0 for the first $k-1$ stages is $\alpha_{0m}, m = 1,2,\ldots k-1$, and the partial solution obtained for each stage is $V(\alpha_{0m}), m = 1,2,\ldots k-1$, then the final voltage

solution is $V = V(\alpha_{01}) \cdot V(\alpha_{02}) \ldots \cdot V(\alpha_{0k-1}) \cdot V(1)$ (the α_{0k} parameter for the last stage, kth stage, is 1) .

The P-W method was used to solve the PF problem for the 43 bus system. We selected the parameter α_0 for each stage by checking the voltage update error using binary search. This update error is calculated as the difference between two successive Padé approximants. The number of terms used to select α_0 is 32 terms and the voltage update error tolerance is 10^{-11}. Only two stages are performed to get a converged solution for the 43 bus system. The α_0 in the first stage is selected to be 0.6406.

The PBE mismatch and voltage update error using only one P-W step and two P-W steps are shown in Figure 4.13 and Figure 4.14, respectively. Note that using only one P-W step in the P-W method, is exactly the same as solving PF problem using the non-scalable formulation, i.e., the blue solid line in Figure 4.13 is identical to the line in Figure 4.9. As shown in Figure 4.13 and Figure 4.14, the P-W method is able to eliminate the convergence issue for the 43 bus system.

Figure 4.13 Voltage update error vs. number of terms in series using P-W method

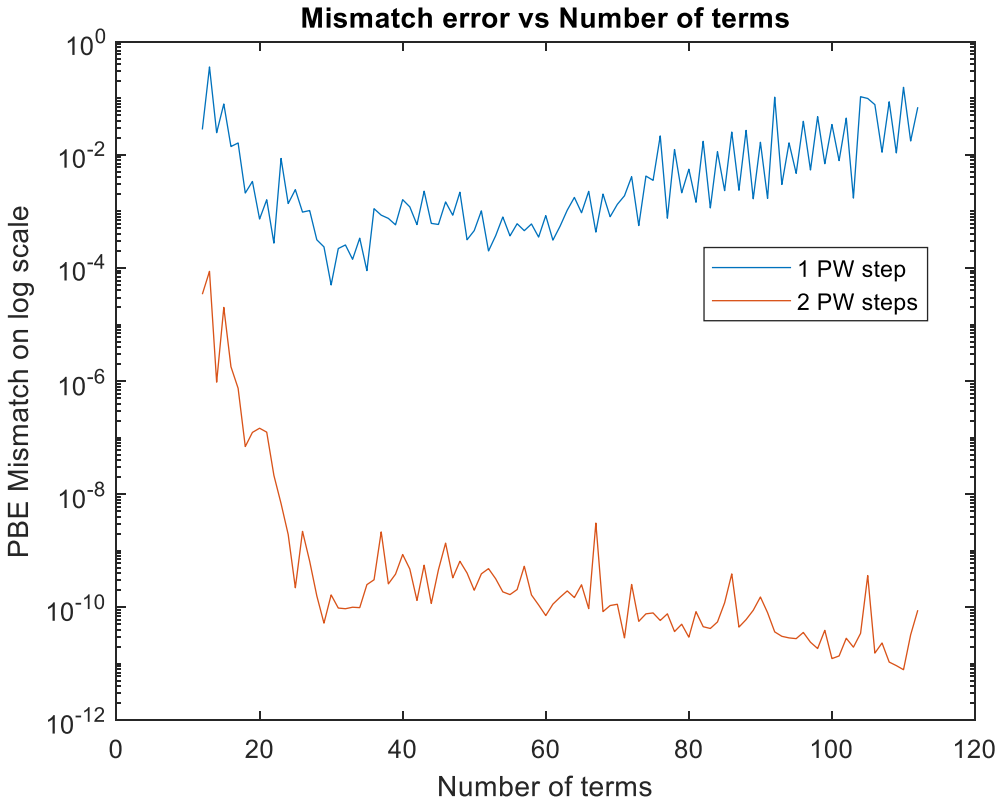

Figure 4.14 PBE mismatch vs. number of terms in series using P-W method

5 COMPARISON OF THE SCALABLE AND THE NON-SCALABLE FORMULATIONS

When embedding the (possibly) complex-valued parameter α into the PBE, there are infinitely many embedding formulations that satisfies the requirements of HEM. However, different formulations result in different algebraic curves and have different branching points, which could affect the numerical convergence of the Padé approximants. The comparison of two common embedding formulations, scalable and non-scalable formulation as demonstrated in section 3.3 and section 3.2 respectively, were discussed in this chapter. The numerical performance of the two formulations were tested on a 43 bus system and a 145 bus system.

5.1 Reference state solution for scalable formulation

As described in section 3.2.2, the reference state for the non-scalable form presented in that section can be obtained through observation. The reference state is $V[0] = 1$ and $Q[0] = 0$, which is the exact theoretical value without any roundoff error in calculation. For the scalable form, however, recurrence calculations need to be performed to solve the so-called pre-reference state power flow to obtain the reference state as demonstrated in section 3.3.1. Since the calculation of the power series starts from the reference state, it is important to investigate the effect of the accuracy in reference state on the accuracy in final voltage solution. The accuracy tests were performed on IEEE 14 bus system and the process is shown below:

1) The “true” value of the reference state and final voltage solution is taken as that obtained using high precision (100 digits of precision in this experiment)
2) The reference state was obtained using double precision and a different number of terms in power series (n from 2 to 8 in this experiment).
3) For each reference state, double precision was used to calculate the final voltage solution as accurate as possible.
4) The maximum error for reference state and final voltage solution was calculated in two ways: the magnitude of the difference between the complex-valued voltage and the complex-valued “true” solution; PBE mismatch error.

The maximum PBE mismatch error for the final solution was plotted against the maximum PBE mismatch error for the reference state as shown in Figure 5.1. The maximum voltage error for the final solution was plotted against the maximum voltage error for the reference state in Figure 5.2. It can be observed that the accuracy in the reference state has a significant effect on the accuracy in final voltage solution and the relationship is almost linear. These plots show that the final solution can be no more accurate than the reference state. Therefore, when the numerical experiments are conducted to compare the properties of the scalable and non-scalable formulations, one must ensure that the reference state of the scalable form is accurate enough.

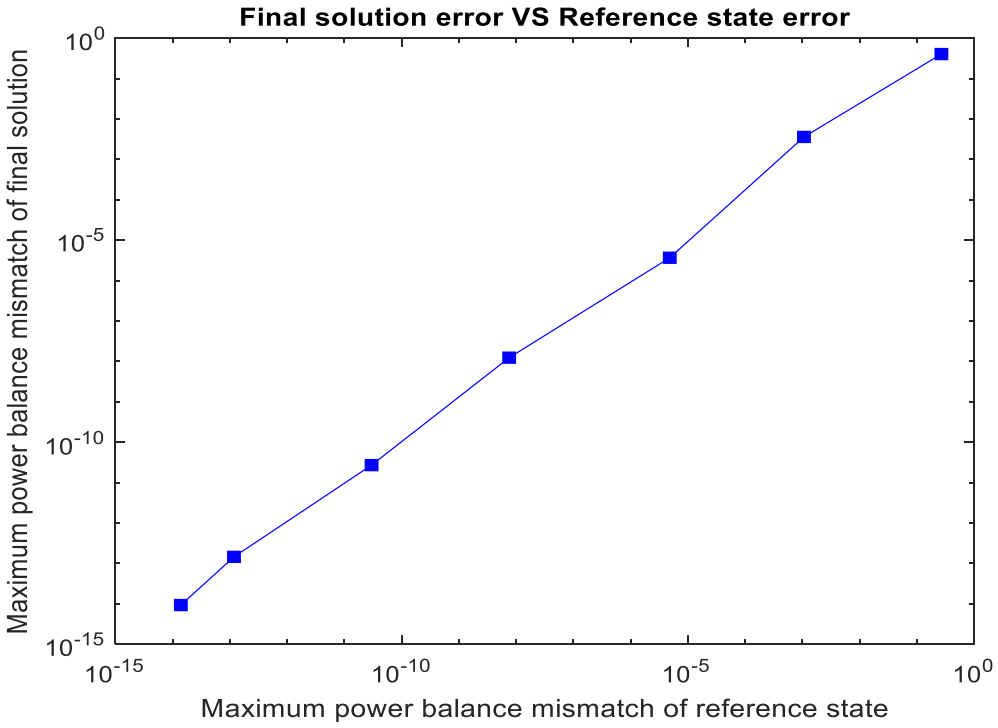

Figure 5.1 Maximum PBE mismatch for the final voltage solution vs. maximum PBE mismatch for the reference state

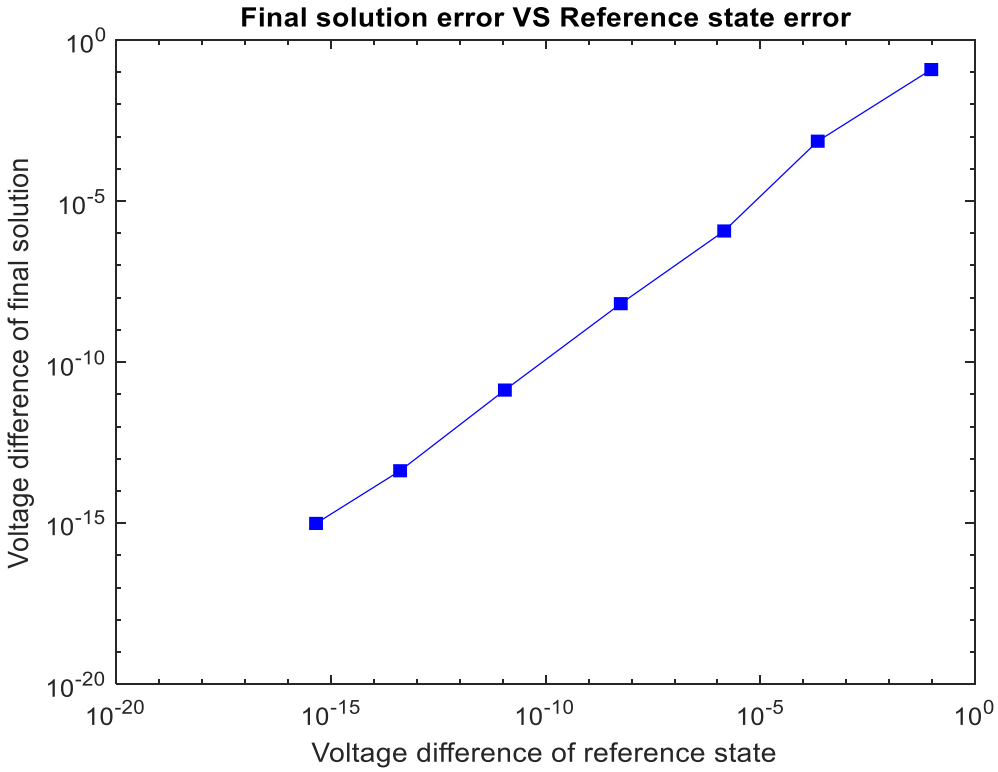

Figure 5.2 Maximum voltage error for the final voltage solution vs. maximum voltage error for the reference state

5.2 Comparison of the scalable and non-scalable formulations on the 43 bus system

The numerical performance of the scalable form and non-scalable forms was tested on a problematic system, the 43 bus system [30]. We observed that the two formulations show different numerical properties, which are discussed in the following subsections.

5.2.1 Bus power mismatch

Figure 5.3 shows the behavior of the PBE mismatch as the number of terms in series increases for the 43 bus system using the scalable form and non-scalable form. It can be observed that when using the non-scalable formulation, the PF fails to converge after around 30 terms while when using the scalable formulation, the PF solution continues

converging through 200 terms and the PBE mismatch error decreases to as small as 10^{-6} pu using a 100 MVA base.

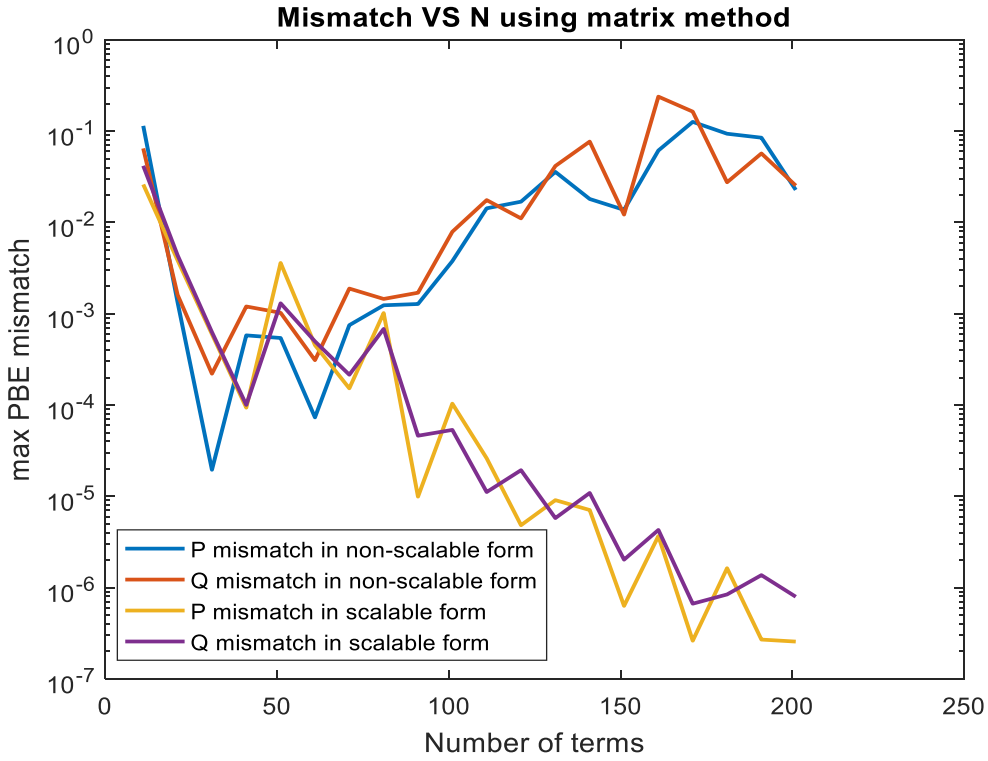

Figure 5.3 Maximum PBE mismatch vs. number of terms in series for the 43 bus system using scalable/non-scalable form and matrix method

In Figure 5.3, we use the matrix method to calculate the Padé approximant. As shown earlier, for the matrix method, which is an $O(N^3)$ method, the solution of the Padé matrix equation for the coefficients of the denominator polynomial (as shown in (3.41)) may become ill-conditioned and thus cause precision loss. To avoid the effect of inaccuracy caused by the matrix method, we repeated this experiment using a Padé approximant method with $O(N^2)$ complexity, the eta method, which is computationally efficient and does not require matrix factorization. This method does not produce a rational function representation of the curve; rather it produces the value of the function

at the loading of interest. The hope was the less computationally complex method would incur less roundoff error and therefore have better performance as the number of series terms increased; however, the eta method produced similar results to those of the matrix method, as shown in Figure 5.4.

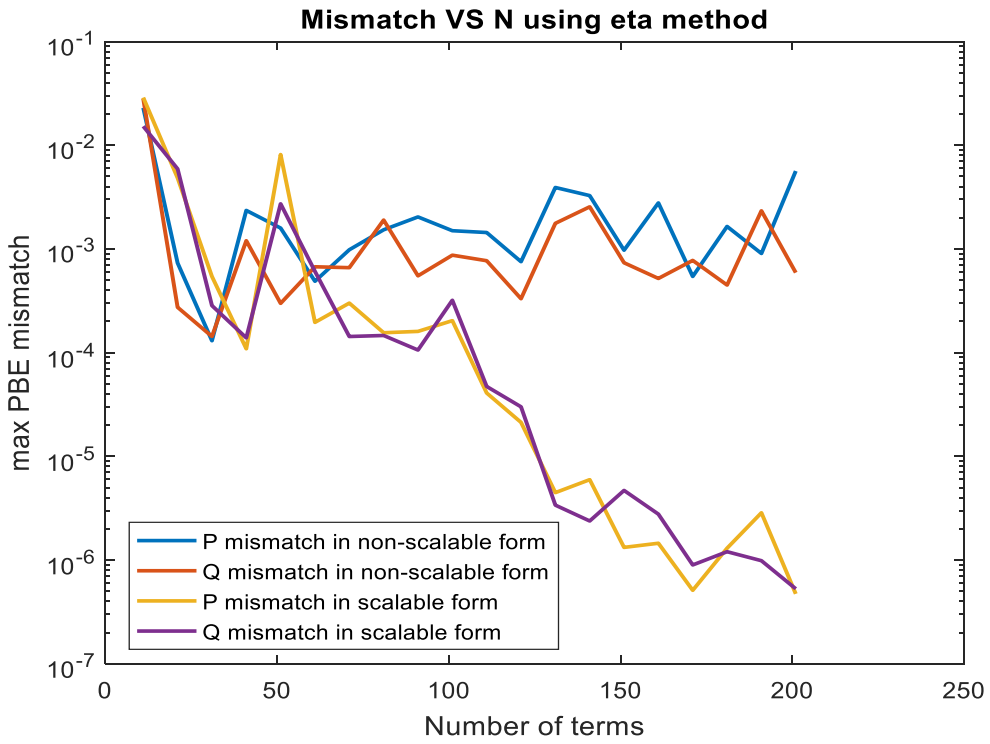

Figure 5.4 Maximum PBE mismatch vs. number of terms in series for the 43 bus system using scalable/non-scalable form and eta method

5.2.2 Voltage error

We obtained the voltage solution for the scalable and non-scalable forms using 16 digits and 86 digits of precision. The voltage error was obtained by calculating the difference between the complex-valued voltage with 16 digits of precision and the complex-valued voltage with 86 digits of precision (regarded as the "true" solution). The voltage error results for the scalable and the non-scalable form are shown in Figure

5.5 and Figure 5.6 respectively. Similar to section 5.2.1, it is shown that the HEM with the scalable form produces a converged solution for the 43 bus system while the voltage error values obtained from the HEM formulation using the non-scalable form fails to improve beyond about 30 series terms.

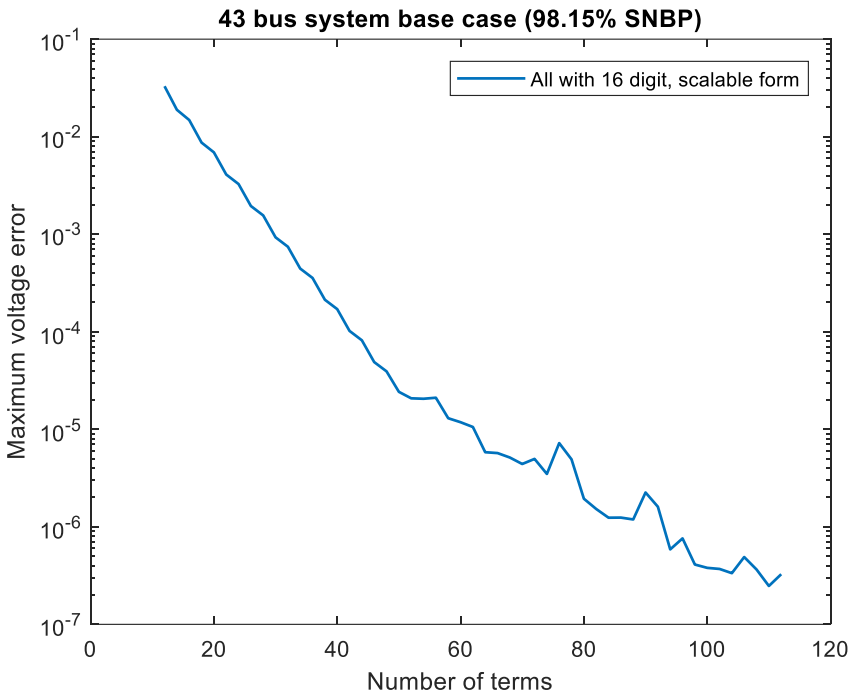

Figure 5.5 Maximum voltage error vs. number of terms in series for the 43 bus system using scalable formulation

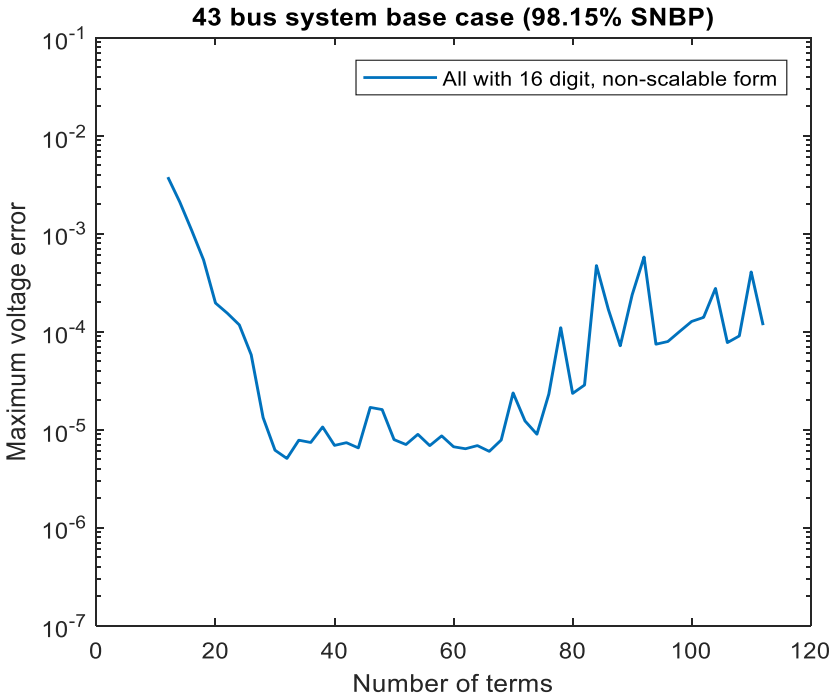

Figure 5.6 Maximum voltage error vs. number of terms in series for the 43 bus system using non-scalable formulation

5.2.3 Series coefficient behavior

The voltage power series obtained from the scalable and non-scalable formulations also have different behavior. The magnitude of the power series for the scalable form as shown in Figure 5.7 oscillates and has a tendency to decrease while the power series for the non-scalable form as shown in Figure 5.8 diverges quickly and approaches the behavior of a geometric series after 5 terms.

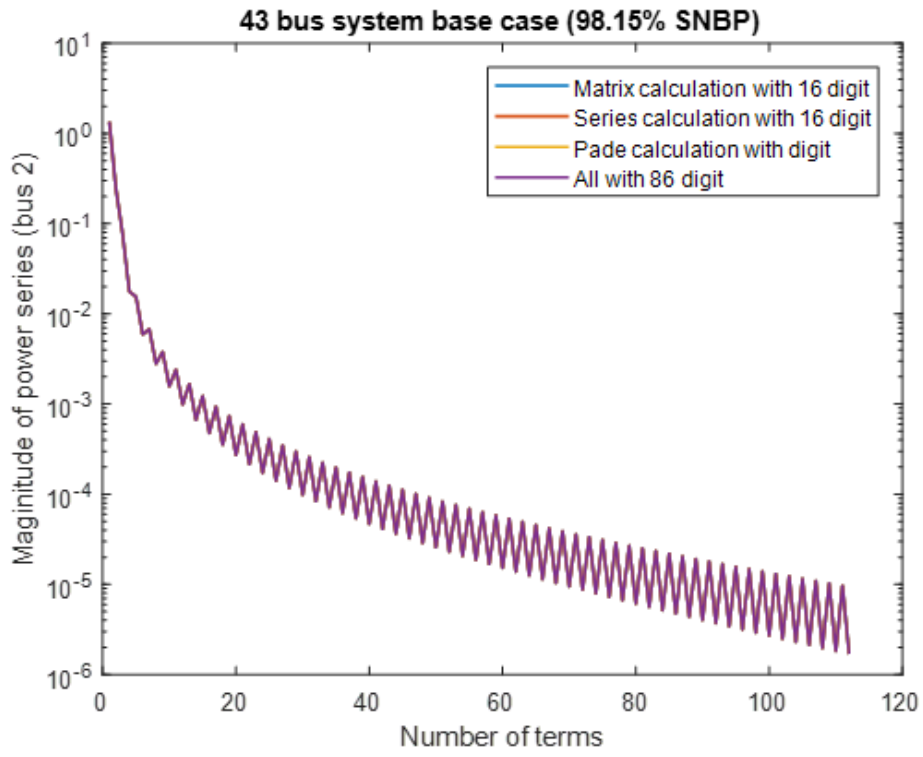

Figure 5.7 Magnitude of power series vs. number of terms in series at bus 2 for the 43 bus system using scalable formulation

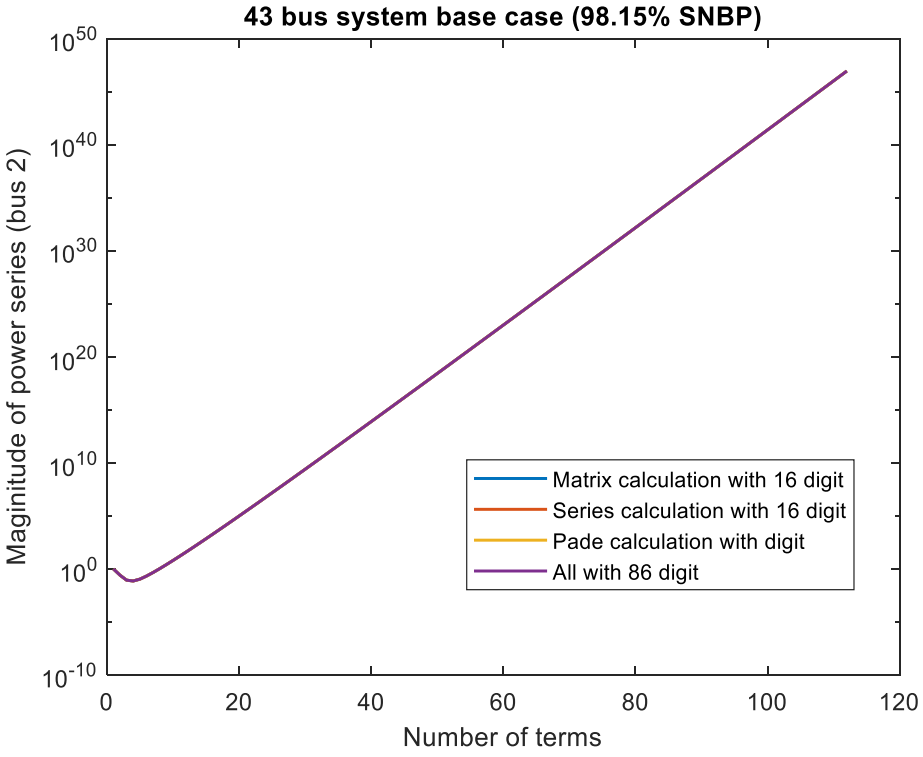

Figure 5.8 Magnitude of power series vs. number of terms in series at bus 2 for the 43 bus system using non-scalable formulation

5.2.4 Poles and zeros

The distribution of poles/zeros for the scalable and non-scalable formulations are also different. Plotted in Figure 5.9 and Figure 5.10 are the poles/zeros of the [55/56] Padé approximant at bus 2, calculated with 16 digits of precision, using the scalable and non-scalable formulations, respectively. The spurious poles/zero pairs (known as Froissart doublets) for the scalable formulation, as shown in Figure 5.9, are accumulating on a circle centered at the origin but because they are not close to the real axis, one can still obtain a converged solution using scalable formulation. However, for the non-scalable formulation, the spurious poles/zeros that are near the real axis at around 0.3 could lead to convergence issue. The radius of convergence (ROC) of the power series for the non-scalable form in this case is approximately 0.3.

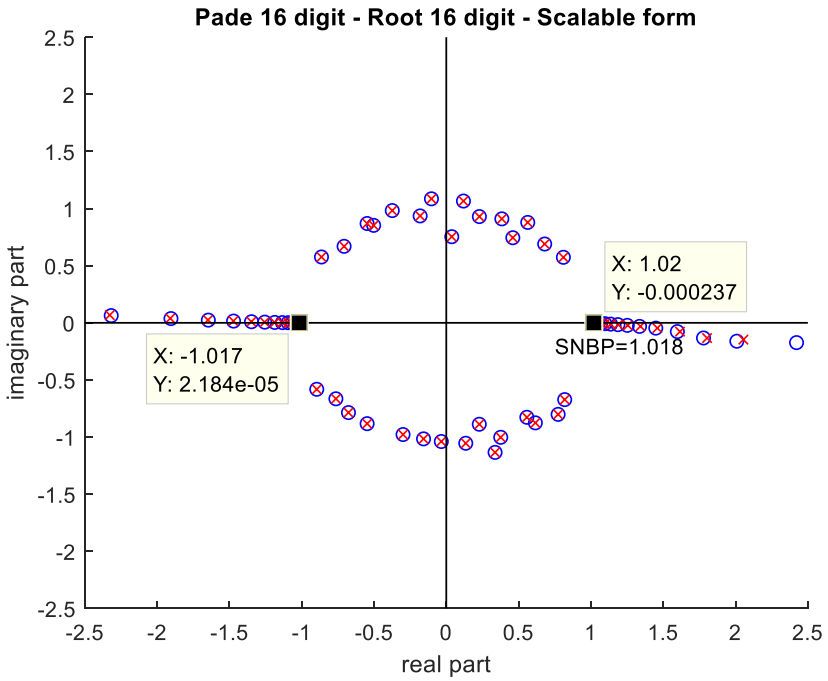

Figure 5.9 The 43 bus system pole-zero plot for [55/56] Padé approximant with scalable form and double precision

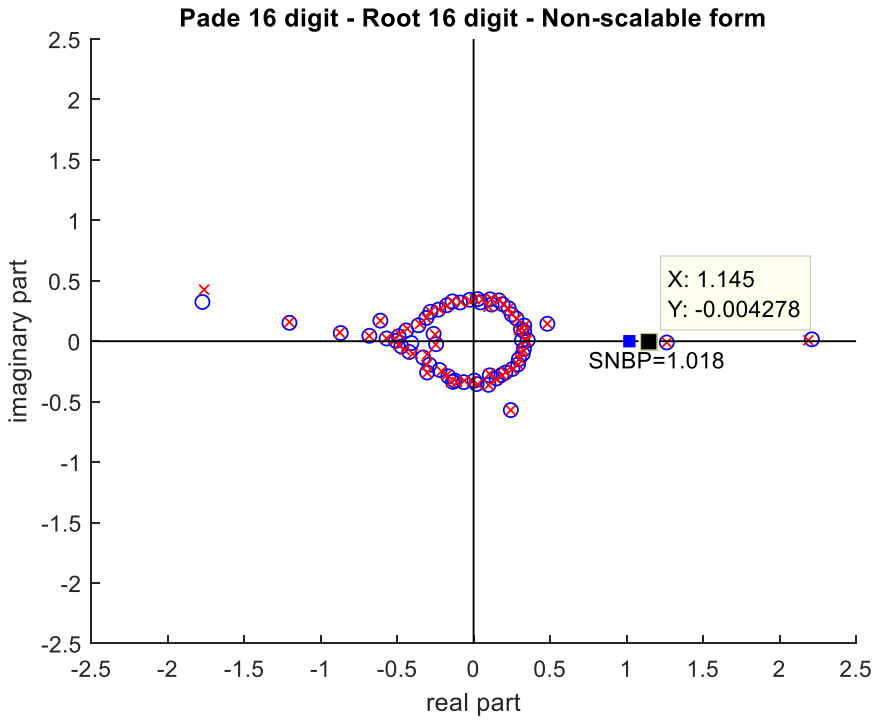

Figure 5.10 The 43 bus system pole-zero plot for [55/56] Padé approximant with non-scalable form and 16 digits of precision

When using 250 digits of precision to perform the HEM PF, the poles/zeros for the Pade approximants obtained for the scalable and non-scalable formulations are shown in Figure 5.11 and Figure 5.12 respectively. The spurious poles/zeros caused by roundoff error disappear. While the poles/zeros for the scalable form are all on or near the real axis, for the non-scalable from, some poles/zeros are located at a branch perpendicular to the real axis at around $\alpha = 2.2$.

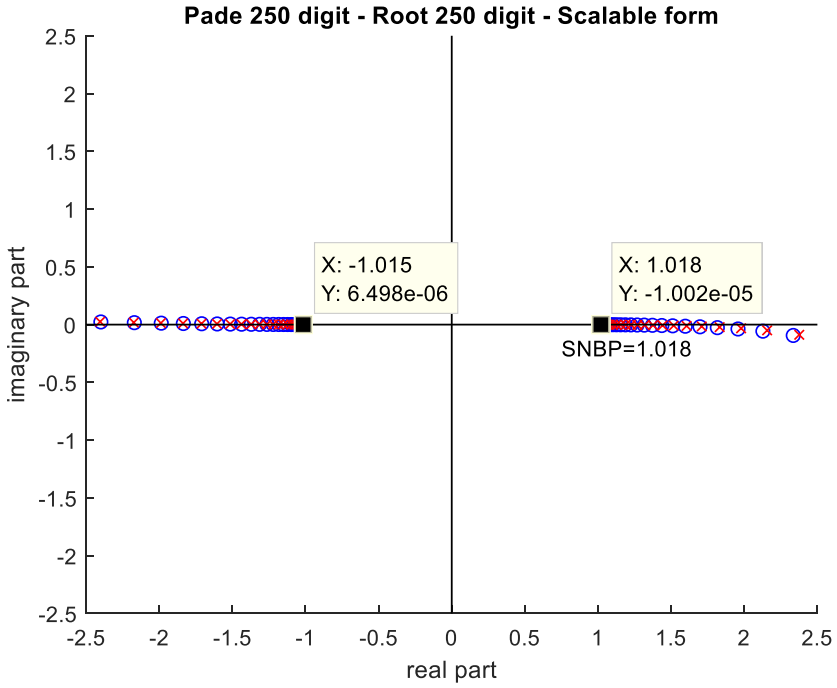

Figure 5.11 The 43 bus system pole-zero plot for [55/56] Padé approximant with scalable form and 250 digits of precision

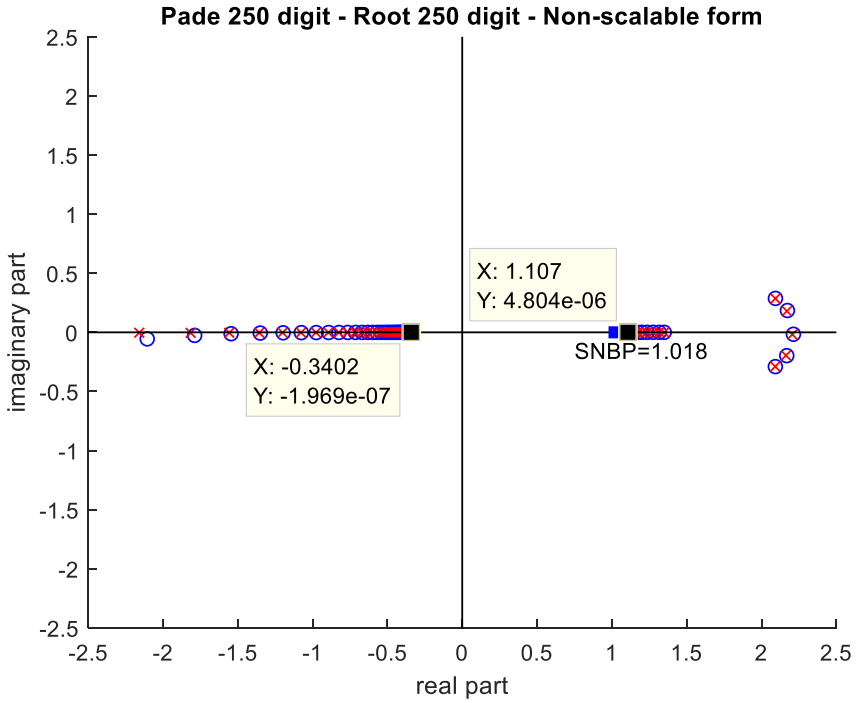

Figure 5.12 The 43 bus system pole-zero plot for [55/56] Padé approximant with non-scalable form and 250 digits of precision

5.3 Comparison of the scalable and non-scalable formulations on the 145 bus system

The IEEE 145 bus system, which contains 50 generators, is one test case for dynamic stability analysis. Here we only focus on solving the power flow problem (used to establish initial conditions for the dynamic simulation) for this system using the scalable or non-scalable formulation. When using the non-scalable formulation with 40 terms, HEM is able to give a convergent solution. The PBE mismatch is 5.8×10^{-6} pu on a 100 MVA base. The error in the voltage magnitude and voltage angle compared with the PF solution from MATPOWER (using a convergence tolerance of 10^{-8}) is 8.1×10^{-8} pu and 4.9×10^{-6} degree. However, the HEM scalable form fails to converge because one cannot get a convergent reference state solution from the so-called pre-reference state power flow. The pole/zero plot for the Padé approximants obtained for bus 10 from the pre-reference state PF is shown in Figure 5.13. The smallest positive-real-valued pole/zero is 0.3. Thus, one cannot obtain a converged solution at $\alpha = 1$ because it is beyond a branch point. The physical explanation to this is: The reference state represents the no load/no power solution. In that case, all real/reactive power can only be delivered by the slack bus. Because the shunt conductance of the 145 bus system is relatively large, the slack bus cannot deliver such a large amount of real power to buses electrically far from the slack bus and thus leads to voltage collapse.

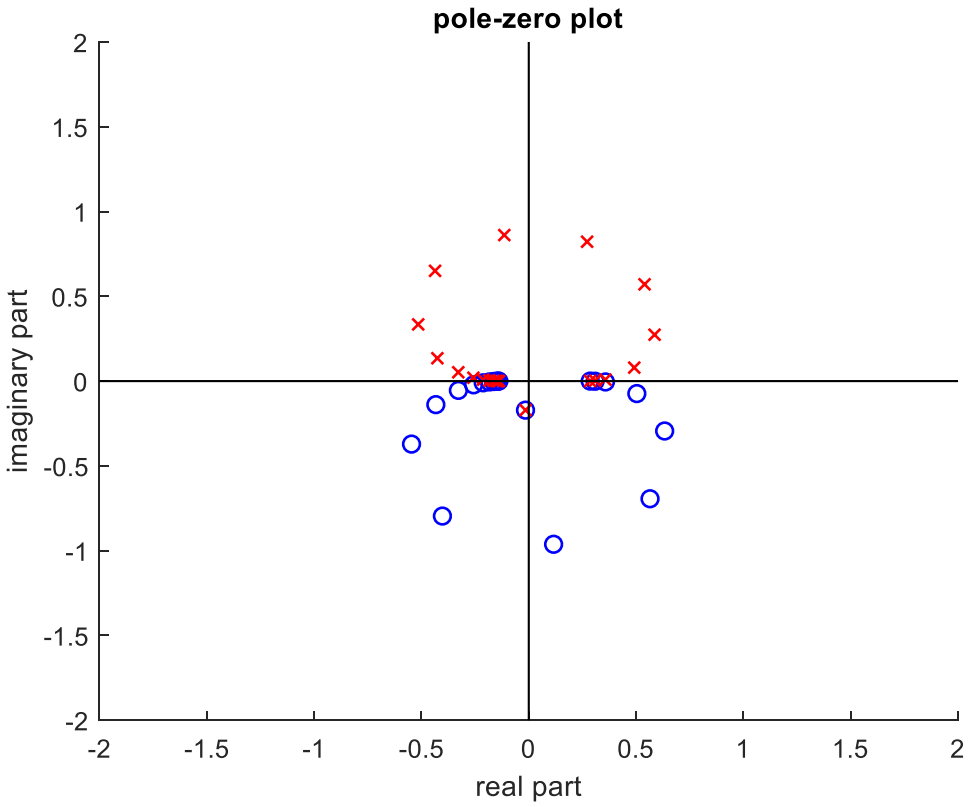

Figure 5.13 The 145 bus system pole-zero plot for Padé approximant in the pre-reference state power flow for scalable form

6 HEM-BASED METHODS TO ESTIMATE THE SNBP FROM LOCAL MEASUREMENTS

6.1 Local-measurement-based methods of estimating the steady-state voltage stability margin

Local-measurement-based methods use local measurements (voltage and current) at the bus-of-interest to build a Thévenin equivalent network, i.e., a voltage source connected through a Thévenin impedance as shown in Figure 6.1.

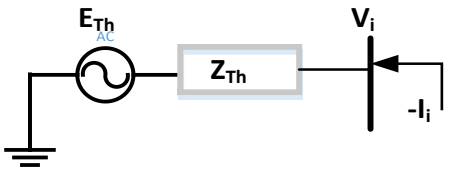

Figure 6.1 Thévenin equivalent at the bus of interest

From Figure 6.1,

$$E_{th} - I_i Z_{th} = V_i \tag{6.1}$$

where E_{th} is the Thévenin voltage, Z_{th} is the Thévenin impedance, V_i is the load voltage and I_i is the load current. The values of V_i and I_i can be obtained from measured data. The equivalent load impedance at bus i can be calculated by (6.2),

$$Z_L = \frac{V_i}{I_i} \tag{6.2}$$

Assuming that, during a short sampling interval the change of the operating conditions of the external system are small and can be ignored, the parameters of the Thévenin equivalent will remain constant during the sampling period. At least two

distinct measurement data points are needed to estimate the Thévenin network parameters. Because measurements are contaminated with noise, more data points in the sampling window are taken to give a more accurate estimate of the Thévenin equivalent parameters. Some approaches such as the least squares approach and Kalman Filter can be used for their estimation. If we only consider two distinct measurements here for simplicity, the Thévenin parameters are given by (6.3) and (6.4).

$$Z_{th} = (V_1 - V_2)/(I_2 - I_1) \tag{6.3}$$

$$E_{th} = (V_1 I_2 - V_2 I_1)/(I_2 - I_1) \tag{6.4}$$

It is well known that if the voltage source is constant and the load power factor is fixed, the maximum real power is delivered to the load when the magnitude of the Thévenin impedance matches the magnitude of the load impedance, i.e., $|Z_{th}| = |Z_L|$, which can be derived as follows:

Consider the load to be represented by an equivalent impedance Z_L as shown in Figure 6.2.

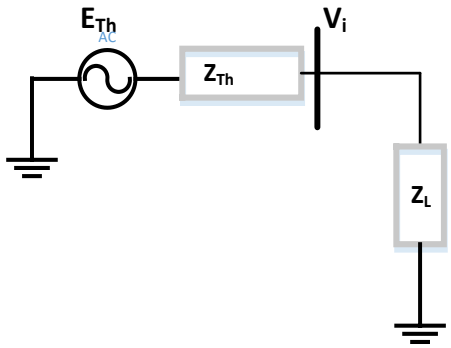

Figure 6.2 Thévenin impedance and load impedance

The real power delivered to the load is given by:

$$P_L = |I_L|^2 R_L \tag{6.5}$$

The load current in the Thévenin equivalent network is given by:

$$I_L = \frac{E_{Th}}{(Z_{Th} + Z_L)} \tag{6.6}$$

Using (6.5) and (6.6), we get:

$$P_L = \left|\frac{E_{Th}}{(Z_{Th} + Z_L)}\right|^2 R_L = \frac{|E_{Th}|^2}{(R_{Th} + R_L)^2 + (X_{Th} + X_L)^2} R_L \tag{6.7}$$

Assuming the power factor angle of the load, ϕ, is kept fixed, the load impedance can be written as:

$$Z_L = R_L + jX_L = R_L + jR_L \tan(\phi) \tag{6.8}$$

Equation (6.7) can thus be written as:

$$P_L = \frac{|E_{Th}|^2 R_L}{(R_{Th} + R_L)^2 + (X_{Th} + R_L \tan\phi)^2} \tag{6.9}$$

The derivative of P_L with respect to R_L is given by (keeping in mind that E_{th} and Z_{th} are assumed to be constant):

$$\begin{aligned} &\frac{dP_L}{dR_L} = \\ &|E_{Th}|^2 \frac{\left((R_{Th} + R_L)^2 + (X_{Th} + R_L \tan\phi)^2\right)}{\left((R_{Th} + R_L)^2 + (X_{Th} + R_L \tan\phi)^2\right)^2} \\ &-|E_{Th}|^2 \frac{R_L\left(2(R_{Th} + R_L) + 2(X_{Th} + R_L \tan\phi)\tan\phi\right)}{\left((R_{Th} + R_L)^2 + (X_{Th} + R_L \tan\phi)^2\right)^2} \end{aligned} \tag{6.10}$$

When the power delivered to the load is maximum, the derivative of P_L with respect to R_L is zero. Equating the RHS of (6.10) to zero, we get:

$$\begin{aligned} &(R_{Th} + R_L)^2 + (X_{Th} + R_L \tan\phi)^2 \\ &= R_L\left(2(R_{Th} + R_L) + 2(X_{Th} + R_L \tan\phi)\tan\phi\right) \end{aligned} \tag{6.11}$$

Equation (6.11) can be expanded as follows:

$$R_{Th}^2 + R_L^2 + 2R_{Th}R_L + X_{Th}^2 + R_L^2 \tan^2\phi + 2X_{Th}R_L \tan\phi = 2R_L R_{Th} + 2R_L^2 + 2R_L X_{Th} \tan\phi + 2R_L^2 \tan^2\phi \quad (6.12)$$

Equation (6.12) can be further simplified to get the final impedance magnitude matching condition for a constant source connected to a fixed power factor load.

$$R_{Th}^2 + X_{Th}^2 = R_L^2 + R_L^2 \tan^2\phi$$
$$\therefore |Z_{Th}|^2 = |Z_L|^2 \quad (6.13)$$
$$\therefore |Z_{Th}| = |Z_L|$$

Hence, once the Thévenin equivalent parameters are obtained, assuming the power-factor of the load remains constant, steady-state voltage collapse occurs when $|Z_{th}| = |Z_L|$.

Consider a simple four-bus system as shown in Figure 6.3 with the bus-of-interest being bus number 3. When using the scalable formulation with the embedded complex parameter α, the voltage is a function of α, since the α acts as a load-scaling factor. When the system is at the voltage collapse point, the corresponding α value is the load scaling factor at the SNBP. The parameters for this system are provided in Table 6.1.

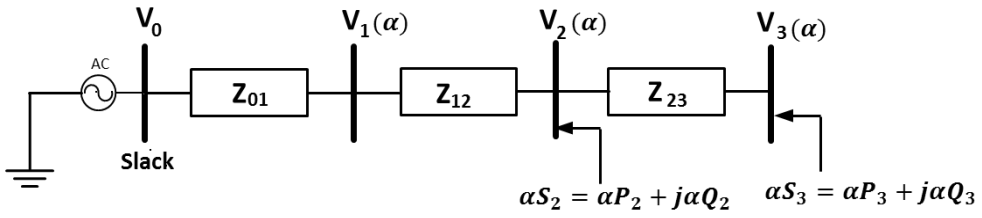

Figure 6.3 Four-bus system

Table 6.1 System parameters for the four-bus system

Parameter name	Value	Parameter name	Value
S_2	50.0+10.0j (MVA)	Z_{23}	0.01j ($\Omega-$ pu)
S_3	10.0+5.0j (MVA)	V_0	1.0 pu
Z_{01}	0.01+0.1j ($\Omega-$ pu)	MVA_{base}	100 MVA
Z_{12}	0.02+0.2j ($\Omega-$ pu)		

To obtain the Thévenin equivalent using this measurement-based method, distinct pseudo-measurements at two values of the load-scaling factor, α, are obtained by solving two power-flow problems using HEM when (a) all injections are scaled by α and (b) all these same injections are perturbed by 1% of their respective base-case injections. Then the Z_L and Z_{th} values are calculated from these two pseudo-measurements using (6.2) and (6.3), respectively. The magnitudes of Z_L and Z_{th} at bus 3 are plotted in Figure 6.4. It is seen that as the load-scaling factor increases, the $|Z_L|$and $|Z_{th}|$ approach each other and are very close to each other at the SNBP (estimated at load-scaling factor = 5.0243, using CPF).

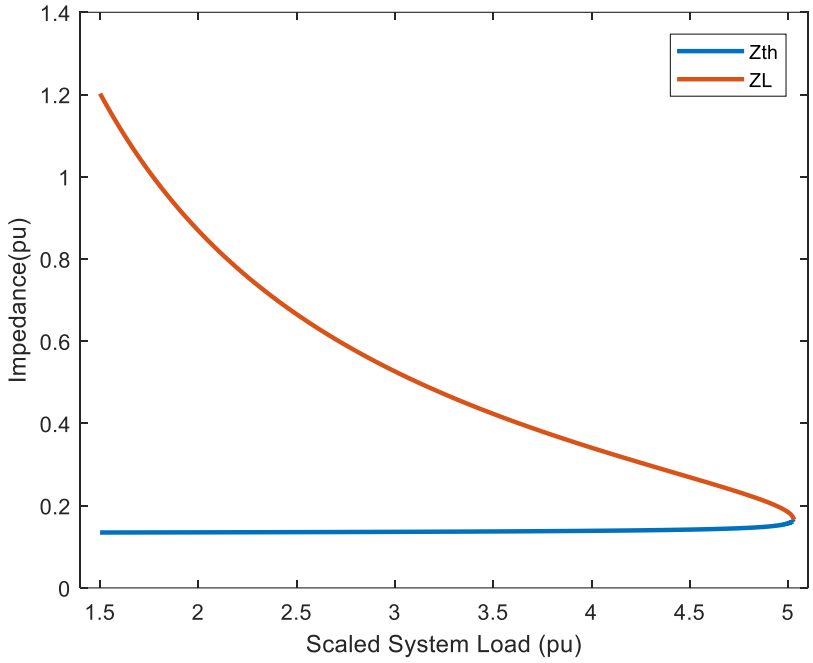

Figure 6.4 Magnitude of Z_L and Z_{th} at bus number 3 vs. the loading scaling factor

In the following section, this Thévenin equivalent (TE) based method will be extended to adapt to HEM.

6.2 HEM-based method to estimate the SNBP using local measurements

As demonstrated in section 6.1, the classical local-measurement-based methods of estimating the steady voltage stability margin are based on the concept of impedance matching between the Thévenin equivalent (TE) of the system and load impedance. The main advantage of these methods is that they only require local measurements and the concept is simple and relatively easy to implement. However, the assumption that the rest of the system does not change as load increases during a short period of time prevents projecting the nonlinear behavior of the loads and generation sources in the system over scaled loading conditions. The HE-reduction, which is essentially a

nonlinear variation of a linearization-based network reduction method, i.e., Ward reduction, can preserve the voltage from the base case up to the SNBP of the system if the operating conditions change along a so-called α line, which has been shown in [52], [53]. Therefore, building a nonlinear Thévenin-like network using HE reduction might have the following advantages compared to conventional TE-based methods:

- It allows the nonlinear behavior the original system impedances and sources to be projected for scaled loading conditions.
- Fitting a polynomial function for the voltage at the bus-of-interest using measurements in certain range (will be discussed in section 6.3) can also give more information about the expected voltage under different operating conditions.
- It can give an accurate estimate of SNBP (assuming no discrete changes in the system occur, such generators going on VAr limits).

6.2.1 Developing a Thévenin-like network using HE reduction

Consider the four-bus system shown in Figure 6.3 as an example. The bus-of-interest is bus number 3. To obtain the Thévenin-like network, the first step is to reduce the original nonlinear system to a two-bus nonlinear network that only contains the slack bus and the bus-of interest, i.e., bus 3 in this example, using HEM-based nonlinear reduction techniques [52]. The reduced network is shown in Figure 6.5. The external buses bus 1 and bus 2 are eliminated and the functions $I_{0\_inj}(\alpha)$ and $I_{3\_inj}(\alpha)$ that

represent the appropriate portions of the external (nonlinear) current injections from buses 1 and 2 are moved to the boundary buses, i.e., bus 0 and bus 3, respectively, for this system. The series impedance Z_s is a constant and is the same as the impedance obtained from Ward reduction. The voltage at bus 3 is given by:

$$V_3(\alpha) = V_0 + \left[\frac{\alpha S_3^*}{V_3^*(\alpha^*)} + I_{3_{inj}}(\alpha)\right] Z_s \tag{6.14}$$

Then to preserve the power injection at the bus-of-interest, bus 3, the current injection generated from HE reduction at bus 3, $I_{3\_inj}(\alpha)$, should be moved. If we define a voltage source $V_s(\alpha)$ as given below, (which is derived by doing a Thévenin-to-Norton-to-Thévenin source conversion at the slack bus):

$$V_s(\alpha) = V_0 + I_{3\_inj}(\alpha) Z_s \tag{6.15}$$

Equation (6.14) now becomes:

$$V_3(\alpha) = V_s(\alpha) + \frac{\alpha S_3^*}{V_3^*(\alpha^*)} Z_s \tag{6.16}$$

Thus, the two-bus network according to (6.16), as shown in Figure 6.6, is the Thévenin-like network consisting of a variable voltage source $V_s(\alpha)$, connected to the bus-of-interest bus 3 through a constant impedance Z_s.

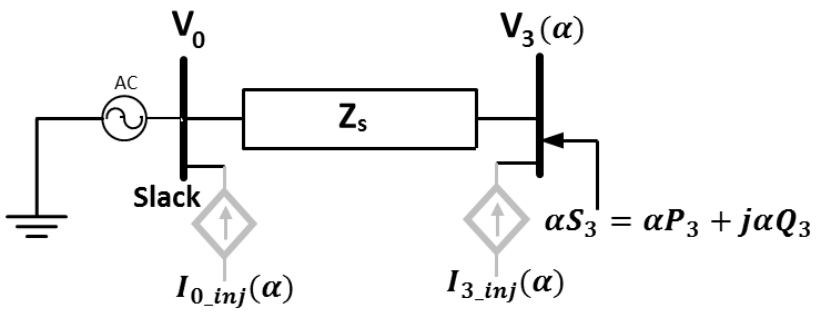

Figure 6.5 HE-reduced network

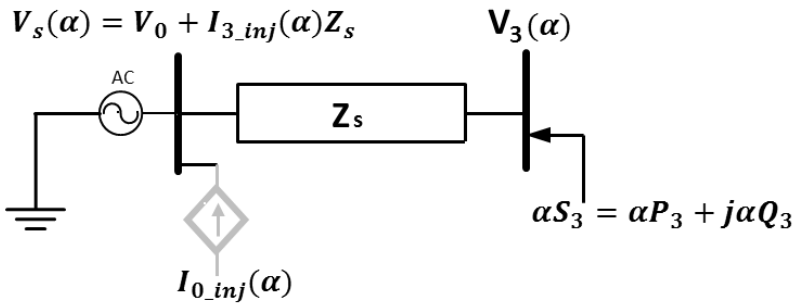

Figure 6.6 Thévenin-like network from the HE reduction

Note that during the derivation, the load current and load voltage are preserved. Even though a part of the external current injection has been moved to the slack bus, the power delivered to the load bus in the reduced network is the same as that in the original full network.

6.2.2 Developing the Maximum Power Transfer Theorem for the Thévenin-like network

It is known that for the Thévenin equivalent network, in which the voltage source and Thévenin impedance are assumed to be constant, the maximum power transfered to the load occurs when the magnitude of the load impedance is equal to the magnitude of the Thévenin impedance i.e. $|Z_{th}| = |Z_L|$. However, in the Thévenin-like network developed in section 6.2.1, the voltage source is a function of the load scaling factor α. Hence the assumption of a constant voltage source is no longer valid, thus the impedance matching condition $|Z_{source}| = |Z_L|$ is no longer true at the maximum power transfer point. Therefore, it is important to derive the maximum power transfer theorem (MPTT) that works for this nonlinear HE-reduced network. Using the same

approach as that used for linear networks, i.e., equating the derivative of the real power with respect to the load resistance to zero, the derivation is described below.

The power delivered to the load in the Thévenin-like network shown in Figure 6.6, is given by (6.17) which is similar to (6.9), with the only difference being that the E_{th} is replaced by $V_s(\alpha)$ which is the nonlinear voltage source in the Thévenin-like network and R_{th},X_{th} are replaced by R_s, X_s which are the resistive and reactive components of the series impedance Z_s.

$$P_L = \frac{|V_S(\alpha)|^2 R_L(\alpha)}{\left(R_S + R_L(\alpha)\right)^2 + \left(X_S + X_L(\alpha)\right)^2} \tag{6.17}$$

Assuming that the power factor angle of the load, ϕ, is kept fixed, the load impedance can be written as:

$$Z_L(\alpha) = R_L(\alpha) + jX_L(\alpha) = R_L(\alpha) + jR_L(\alpha)\tan(\phi) \tag{6.18}$$

Equation (6.17) can thus be written as:

$$P_L = \frac{|V_S(\alpha)|^2 R_L(\alpha)}{\left(R_S + R_L(\alpha)\right)^2 + \left(X_S + R_L(\alpha)\tan(\phi)\right)^2} \tag{6.19}$$

The derivative of P_L with respect to R_L is given by:

$$\begin{aligned}\frac{\partial P_L}{\partial R_L(\alpha)} = & \\ & \frac{\left\{\frac{\partial|V_S(\alpha)|^2}{\partial R_L(\alpha)} R_L(\alpha) + |V_S(\alpha)|^2\right\}\left\{\left(R_S + R_L(\alpha)\right)^2 + \left(X_S + R_L(\alpha)\tan(\phi)\right)^2\right\}}{\left(\left(R_S + R_L(\alpha)\right)^2 + \left(X_S + R_L(\alpha)\tan(\phi)\right)^2\right)^2} \\ & - \frac{|V_S(\alpha)|^2 R_L(\alpha)\left\{2\left(R_S + R_L(\alpha)\right) + 2\left(X_S + R_L(\alpha)\tan(\phi)\right)\tan(\phi)\right\}}{\left(\left(R_S + R_L(\alpha)\right)^2 + \left(X_S + R_L(\alpha)\tan(\phi)\right)^2\right)^2}\end{aligned} \tag{6.20}$$

When the power delivered to the load is maximum, the derivative of P_L with respect to R_L is zero. Equating (6.20) to zero, we get:

$$\begin{aligned}&\left\{\frac{\partial|V_S(\alpha)|^2}{\partial R_L(\alpha)}R_L(\alpha)+|V_S(\alpha)|^2\right\}\left\{\left(R_S+R_L(\alpha)\right)^2+\left(X_S+R_L(\alpha)\tan(\phi)\right)^2\right\}=\\&|V_S(\alpha)|^2R_L(\alpha)\left\{2\left(R_S+R_L(\alpha)\right)+2\left(X_S+R_L(\alpha)\tan(\phi)\right)\tan(\phi)\right\}\end{aligned} \tag{6.21}$$

Equation (6.21) can be rearranged as follows:

$$\begin{aligned}&\left\{\frac{\partial|V_S(\alpha)|^2}{\partial R_L(\alpha)}R_L(\alpha)\right\}\left\{\left|Z_S+Z_L(\alpha)\right|^2\right\}=\\&|V_S(\alpha)|^2R_L(\alpha)\left\{2\left(R_S+R_L(\alpha)\right)+2\left(X_S+R_L(\alpha)\tan(\phi)\right)\tan(\phi)\right\}\\&-|V_S(\alpha)|^2\left\{\left(R_S+R_L(\alpha)\right)^2+\left(X_S+R_L(\alpha)\tan(\phi)\right)^2\right\}\end{aligned} \tag{6.22}$$

The terms of the right-hand side expression can be expanded to obtain:

$$\begin{aligned}&\left\{\frac{\partial|V_S(\alpha)|^2}{\partial R_L(\alpha)}R_L(\alpha)\right\}\left\{\left|Z_S+Z_L(\alpha)\right|^2\right\}=\\&|V_S(\alpha)|^2\left\{\begin{aligned}&2R_SR_L(\alpha)+2R_L^2(\alpha)+2X_SR_L(\alpha)\tan(\phi)+2R_L^2(\alpha)\tan^2(\phi)\\&-\left\{R_S^2+R_L^2(\alpha)+2R_SR_L(\alpha)+X_S^2+R_L^2(\alpha)\tan^2(\phi)+2X_SR_L(\alpha)\tan(\phi)\right\}\end{aligned}\right\}\end{aligned} \tag{6.23}$$

Equation (6.23) is then reduced to (6.24):

$$\begin{aligned}&\left\{\frac{\partial|V_S(\alpha)|^2}{\partial R_L(\alpha)}R_L(\alpha)\right\}\left\{\left|Z_S+Z_L(\alpha)\right|^2\right\}=\\&=|V_S(\alpha)|^2\left\{R_L^2(\alpha)+R_L^2(\alpha)\tan^2(\phi)-R_S^2-X_S^2\right\}\\&=|V_S(\alpha)|^2\left\{\left|Z_L(\alpha)\right|^2-\left|Z_S\right|^2\right\}\end{aligned} \tag{6.24}$$

Equation (6.24) can be rearranged to the final maximum power transfer condition given by (6.25).

$$\frac{\partial|V_S(\alpha)|^2}{\partial R_L(\alpha)}\frac{R_L(\alpha)}{|V_S(\alpha)|^2}=\frac{\left|Z_L(\alpha)\right|^2-\left|Z_S\right|^2}{\left|Z_S+Z_L(\alpha)\right|^2} \tag{6.25}$$

The validity of the condition given by (6.25) is verified using the four-bus system shown in Figure 6.3. The SNBP of the system is 5.0243 and the bus-of-interest is bus

3. In Figure 6.7 the LHS and RHS of (6.25) for the four-bus system are plotted against the load-scaling factor varying up to the SNBP. It is seen that the LHS and RHS are numerically very close to each other at the SNBP.

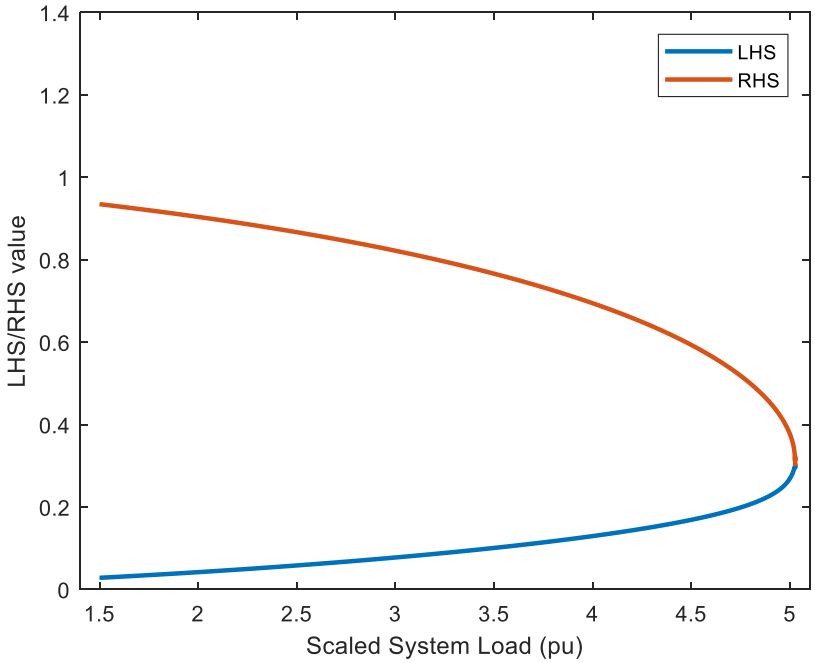

Figure 6.7 LHS and RHS of (6.25) at bus number 3 vs. the loading scaling factor

6.3 Different numerical methods for estimating the SNBP from measurements

In section 6.2.2, the maximum power transfer theorem (MPTT) was developed to estimate the SNBP for the nonlinear reduced network. Therefore, in this section, numerical experiments using noiseless pseudo-measurements to estimate the SNBP from the MPTT given by (6.25) will be conducted. The effects of noise in the measurements will be discussed in later sections.

6.3.1 Fit a function of α from measurements

Since the main process in these experiments is to build the functions of α for each component in (6.25) using noiseless data, different possible approaches to fit a general function of α from measurements will be first discussed in this section.

For a given function of α, $f(\alpha)$, as shown in Figure 6.8, a number of pseudo-measurements in the sample range (for example, 60%-70% of the SNBP in this figure) were generated and a curve fit to the samples in this range with the goal of projecting the value of $f(\alpha)$ beyond the sample range, up to the SNBP. The measurements can be used to fit either a polynomial or a Padé approximant to $f(\alpha)$. Three different approaches for fitting $f(\alpha)$, the Matlab built-in Padé fit, self-coded Padé fit and polynomial fit are discussed as follows:

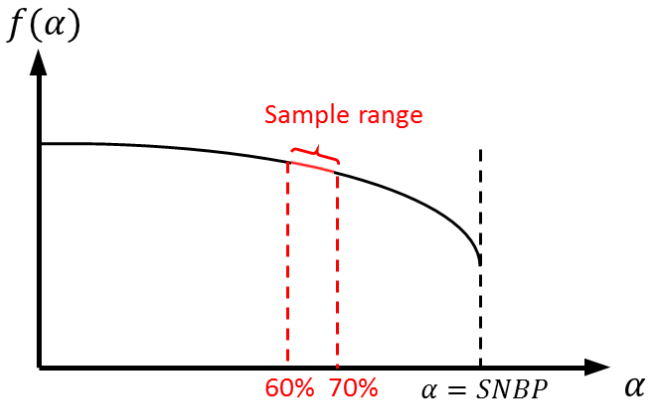

Figure 6.8 Function of α vs. loading-scale factor

i. Self-coded Padé fit

In this case, a rational function of the following form was assumed.

$$f(\alpha) = \sum_{i=0}^{N} c_i\,\alpha^i = \frac{\sum_{i=0}^{M} a_i\,\alpha^i}{\sum_{i=0}^{M+1} b_i\,\alpha^i} = [M/M+1]_{f_\alpha} \quad 2M+2 = N \tag{6.26}$$

$$b_0 = 1$$

where N is the degree of the Maclaurin series of $f(\alpha)$, M and M+1 are the degrees of the numerator and denominator polynomial of the Padé approximant, respectively. For a total of $N_{measure}$ measurements sampled over the range of loading values selected for training, $(\alpha_{k,}\, k = 1,2,\ldots,N_{measure})$, the corresponding overdetermined set of equations shown in (6.27) was solved to calculate the unknown Padé approximant coefficients α_i, and b_i. Note that the Padé approximant coefficients, α_i and b_i, are written in ascending order of exponents of α.

$$\sum_{i=0}^{M} a_i\,\alpha_k^i - f(\alpha_k)\left(\sum_{i=1}^{M+1} b_i\,\alpha_k^i\right) = f(\alpha_k) \tag{6.27}$$

ii. Matlab built-in Padé fit

Similar to the above approach, a set of linear overdetermined equations was solved to directly obtain the coefficients of the Padé approximant. The only difference is that the coefficients, α_i and b_i are written in descending order of exponents of α as given by (6.28).

$$\sum_{i=M}^{0} a_i\,\alpha_k^i - f(\alpha_k)\left(\sum_{i=M+1}^{1} b_i\,\alpha_k^i\right) = f(\alpha_k) \tag{6.28}$$

Though the self-coded Padé fit and Matlab built-in Padé fit are theoretically identical, the subtle difference in the order of coefficients could lead to very different numerical performance. Thus, both of them will be tested in a subsequent section.

iii. Polynomial fit

In this approach, the measurements are used to fit a polynomial to $f(\alpha)$, i.e., to obtain the c_i coefficients in (6.26). The set of equations used to calculate the coefficients is indicated in (6.29):

$$\sum_{i=0}^{N} c_i \, \alpha_k^i = f(\alpha_k) \tag{6.29}$$

6.3.2 Four numerical methods for estimating the SNBP from measurements

As demonstrated in section 6.3.1, there are three approaches to fit the measurements for $f(\alpha)$, while fitting the measuerments for each component in (6.25) is more complicated. For example, for $|V_s(\alpha)|^2$ in (6.25), one can choose to directly fit the polynomial or Padé approximant to the Macluarin series for $|V_s(\alpha)|^2$ by squaring of the magnitude of the source voltage measurements or by fitting the polynomial or Padé approximant to $V_s(\alpha)$ from source voltage measurements and then obtain $|V_s(\alpha)|^2$ calculated from the polynomial or Padé approximant of $V_s(\alpha)$ evaluated at different loading-scale factors. Therefore, there are a number of combinations of which pseudo-measurements are used to fit each constituent term in (6.25) and which fitting technique discribed in section 6.3.1 is applied.

Because the Padé approximant is sensitive to roundoff error in the calculations and because the differences in numerical performance of different methods might become significant when building the networks using noisy measurements, it is important to find the best method for estimating the SNBP based on MPTT from measured data. Therefore, four possible numerical methods are discussed in the following section. Their numerical performance was tested on the IEEE 118 bus system. Noiseless pseudo-measuements were generated for loadings in the range of 60%-70% of the maximum system load (SNBP) using MATPOWER and a power-mismatch convergence tolerance of 10^{-8} (For the Best Component method demonstrated in section 6.3.2.2, the tested system is the modified 118 bus system and the sample range is 70%-80% of the SNBP). In each case, 200 measurements were used to fit 61 terms of a polynomial or [30/30] Padé approximant to each component in (6.25). The SNBP is estimated based on the following two approaches: The SNBP point is taken as the eareliest point where either 1) the LHS and RHS values of (6.25) cross each other, or 2) LHS and RHS values were initially converging and then began to diverge.

6.3.2.1 Built-In/Self-Coded method

The MPTT equation given by (6.25) consists of six different components: Z_s, $R_L(\alpha)$, $Z_L(\alpha)$, $|V_s(\alpha)|^2$, $\partial|V_s(\alpha)|^2/\partial\alpha$ and $\partial R_L(\alpha)/\partial\alpha$ from here on abbreviated $\partial|V_s(\alpha)|^2$ and $\partial R_L(\alpha)$, respectively. The variable Z_s is the source impedance of the Thévenin-like network obtained from HEM/Ward network reduction and it is a constant

value. Thus there is no need to calculate Z_s from measurements. $R_L(\alpha)$ is the resistive component of the load impedance $Z_L(\alpha)$. Once $Z_L(\alpha)$ is obtained, $R_L(\alpha)$ can be calculated by taking the real part of $Z_L(\alpha)$. Therefore, there are only four components that need attention: $Z_L(\alpha)$, $|V_s(\alpha)|^2$, $\partial|V_s(\alpha)|^2$ and $\partial R_L(\alpha)$.

One simple approach is to directly get $Z_L(\alpha)$, $|V_s(\alpha)|^2$, $\partial|V_s(\alpha)|^2$ and $\partial R_L(\alpha)$ as Padé approximants from their respective measurements, though sometimes this was handled differently. For example, the function$|V_s(\alpha)|^2$, was built by fitting a Padé approximant to samples of V_s to yield $V_s(\alpha)$ and then $|V_s(\alpha)|^2$ was calculated by evaluating the square of the magnitude of $V_s(\alpha)$. The implemention details are summarized in Table 6.2. Note that the measurement $\partial|V_s(\alpha)|^2$ is obtained by calculating the increment in $|V_s|^2$ divided by the increment in loading-scale factor, i.e., $\Delta|V_s|^2/\Delta\alpha$. The $\Delta\alpha$ should be small enough so that the $\partial|V_s|^2$ measurement can accurately represent the derivative of $|V_s|^2$ with respect to α in the original system but at the same time making sure there are sufficient distance between two successive points to identify the voltage change. In this experiment, the $\Delta\alpha$ is chosen to be 10^{-6}. Similar approach is used to get ∂R_L measurements.

Table 6.2 Built-In/Self-Coded method

Components	Pseudo-measurements	Algorithm for fitting measurements
Z_s	Source impedance from HEM/Ward network reduction	
$R_L(\alpha)$	Real part of $Z_L(\alpha)$	
$Z_L(\alpha)$	Z_L	Built-In/Self-Coded Padé-fit Z_L
$\lvert V_s(\alpha)\rvert^2$	V_s	1. Built-In/Self-Coded Padé-fit V_s 2. Get $\lvert V_s\rvert^2$
$\partial\lvert V_s(\alpha)\rvert^2$	$\partial\lvert V_s\rvert^2$ $\left(\frac{\lvert V_{s1}\rvert^2-\lvert V_{s2}\rvert^2}{\Delta\alpha}\right)$	Built-In/Self-Coded Padé-fit $\partial\lvert V_s\rvert^2$
$\partial R_L(\alpha)$	∂R_L $\left(\frac{\lvert R_{L1}\rvert^2-\lvert R_{L2}\rvert^2}{\Delta\alpha}\right)$	Built-In/Self-Coded Padé-fit ∂R_L

The LHS and RHS of MPTT equation for the IEEE 118 bus system with the bus-of-interest being bus 44 and bus 67 are plotted against α in Figure 6.9 and Figure 6.10 respectively. The SNBP of the 118 bus system is 3.187, obtained using the CPF. Bus 44 and bus 67 are one weak bus and one strong bus in the 118 bus system respectively (indentified by the voltage changes for load changes near the SNBP). It is seen that for the weak bus bus 44, both the Built-In and Self-Coded methods can give an accurate estimation of the SNBP, which are 3.179 and 3.181, respectively, with only 0.25% and 0.19% errors, respectively. However, in Figure 6.10, neither Built-In nor the Self-Coded methods give a prediction of the SNBP for the strong bus, bus 67, regardless of whether we used the crossover or the divergence criterion. In other words, the Built-In

and Self-Coded methods work well for weak buses but can not work for strong buses in the system.

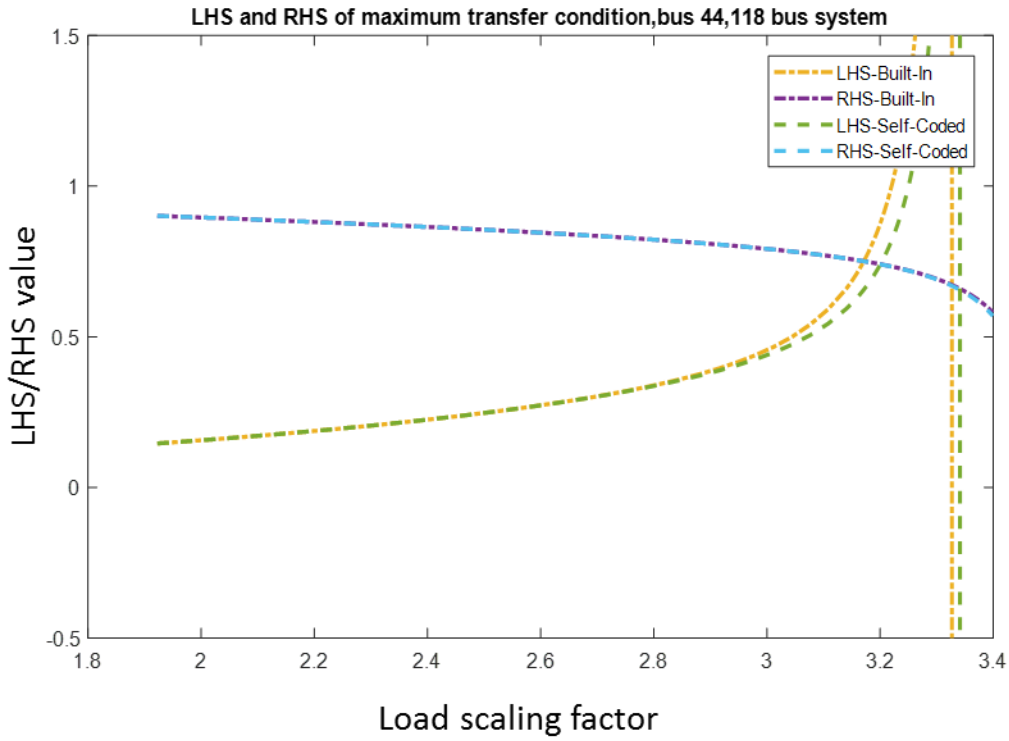

Figure 6.9 LHS and RHS of (6.25) at weak bus number 44 vs. the loading scaling factor for the IEEE 118 bus system

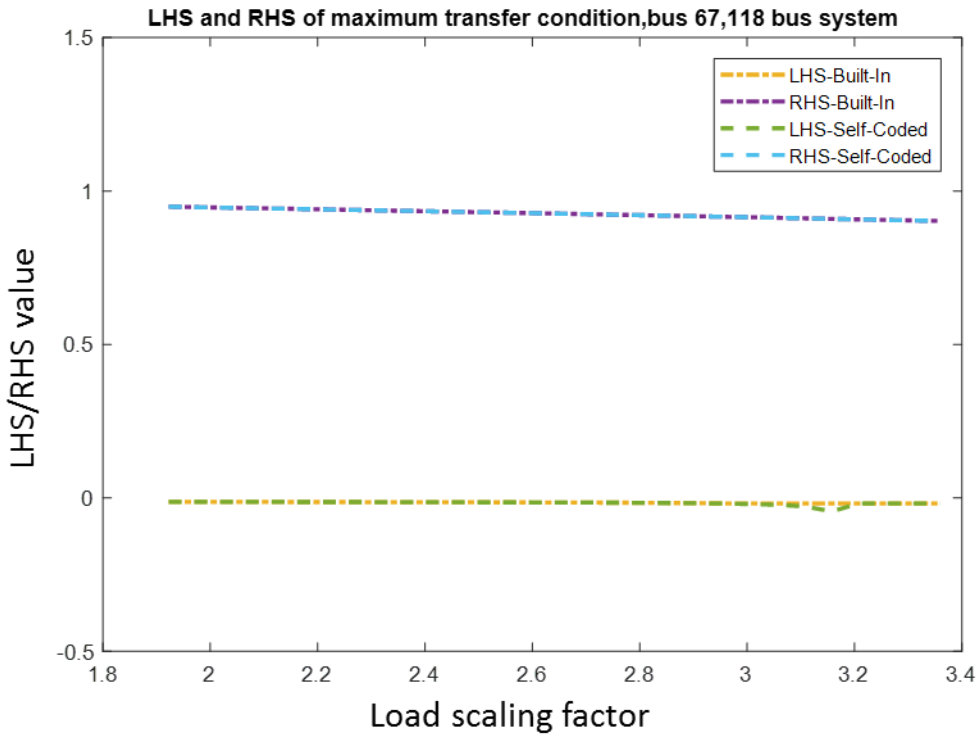

Figure 6.10 LHS and RHS of (6.25) at strong bus number 67 vs. the loading scaling factor for the IEEE 118 bus system

6.3.2.2 Best Component method

In this method, for each constituent of (6.25) ($Z_L(\alpha)$, $|V_s(\alpha)|^2$, $\partial|V_s(\alpha)|^2$ and $\partial R_L(\alpha)$), all of the different ways of fitting the measurements previously mentioned are considered. Note that the 118 bus system here is modified by adding S=1+1j MVA to bus 30, bus 37 and bus 38. The loading value at the SNBP for this modified 118 bus system is 3.172. The loading range for training data obtained as pseudo-measurements is 70%-80% of the SNBP.

First of all, accurately we calculate the "true" value of those variables in the 80%-100% loading range using a 220-digit HEM implementation to obtain the accurate reference values for this range. Then the predictions of these four components are

compared with their "true" values in the 90%-100% range. For each component, the representation that most accurately fit the true value was selected as the best way. The best algorithm for building each component is listed in Table 6.3.

Table 6.3 Best Component method

Components	Pseudo-measurements	Best algorithm for fitting measurements
Z_s	Source impedance from HEM/Ward network reduction	
$R_L(\alpha)$	Real part of $Z_L(\alpha)$	
$Z_L(\alpha)$	Z_L	Built-In Padé-fit Z_L
$\lvert V_s(\alpha)\rvert^2$	$\lvert V_s\rvert^2$	Self-Coded Padé-fit V_s
$\partial\lvert V_s(\alpha)\rvert^2$	$\partial\lvert V_s\rvert^2$ $\left(\frac{\lvert V_{s1}\rvert^2-\lvert V_{s2}\rvert^2}{\Delta\alpha}\right)$	Self-Coded Padé-fit $\partial\lvert V_s\rvert^2$
$\partial R_L(\alpha)$	∂R_L $\left(\frac{\lvert R_{L1}\rvert^2-\lvert R_{L2}\rvert^2}{\Delta\alpha}\right)$	Self-Coded Padé-fit ∂R_L

Some of the simultation results examining the results of the Best Component method are discussed in this section. The LHS and RHS of the MPTT equation for the modified 118 bus system with the buses-of-interest being buses 22 and 67 are plotted against α in Figure 6.11 and Figure 6.12 respectively. The curves labeled 1) "LHS-mp220", 2) "LHS-Built-In", 3) "LHS-Self-Coded" and 4) "LHS-Best-Component" represent the LHS of MPTT value of Padé approximant 1) from network reduction using 220 digit precision, 2) from measurements using the Built-In method, 3) from measurements using the Self-Coded method and 4) from measurements using the Best Component method. The legend beginning with "RHS-" stands for the RHS of the

MPTT value of the Padé approximant. For bus 22, which is a weak bus in the system, the Best Component method is shown to be better than the Buit-In and the Self-Coded methods, but not significantly better. This slightly superior performance has also been seen for some other weak buses when the measurement range remains to be 70%-80%. However, this method does not work well for a strong bus since there is no point where the LHS and RHS cross each other or diverge and thus no prediction can be made as shown in Figure 6.12 (the yellow and purple line).

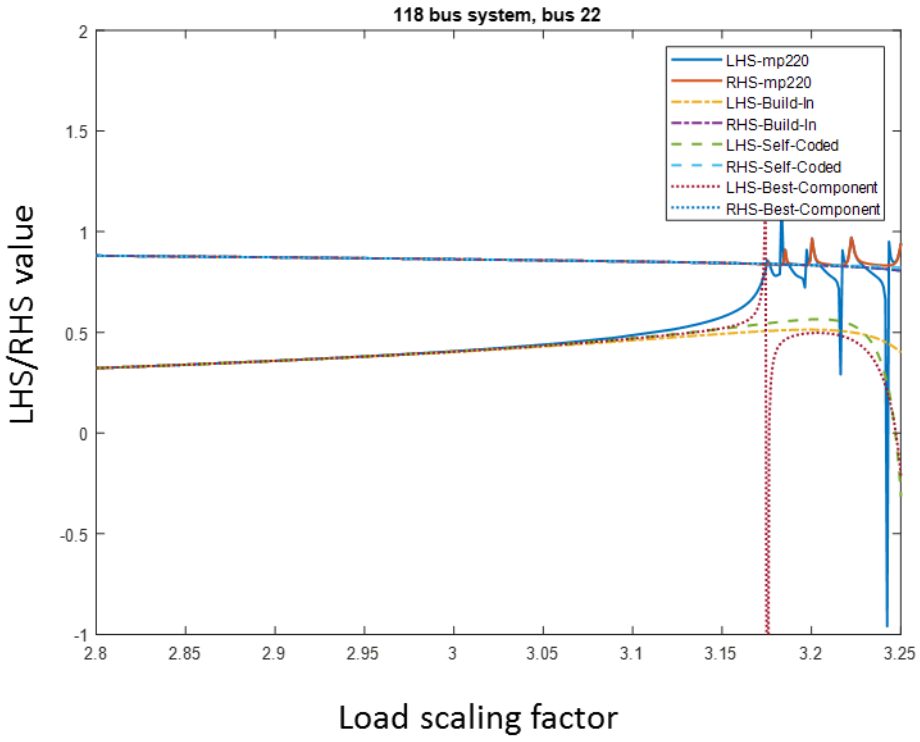

Figure 6.11 LHS and RHS of (6.25) at weak bus number 22 vs. the loading scaling factor for the modified 118 bus system

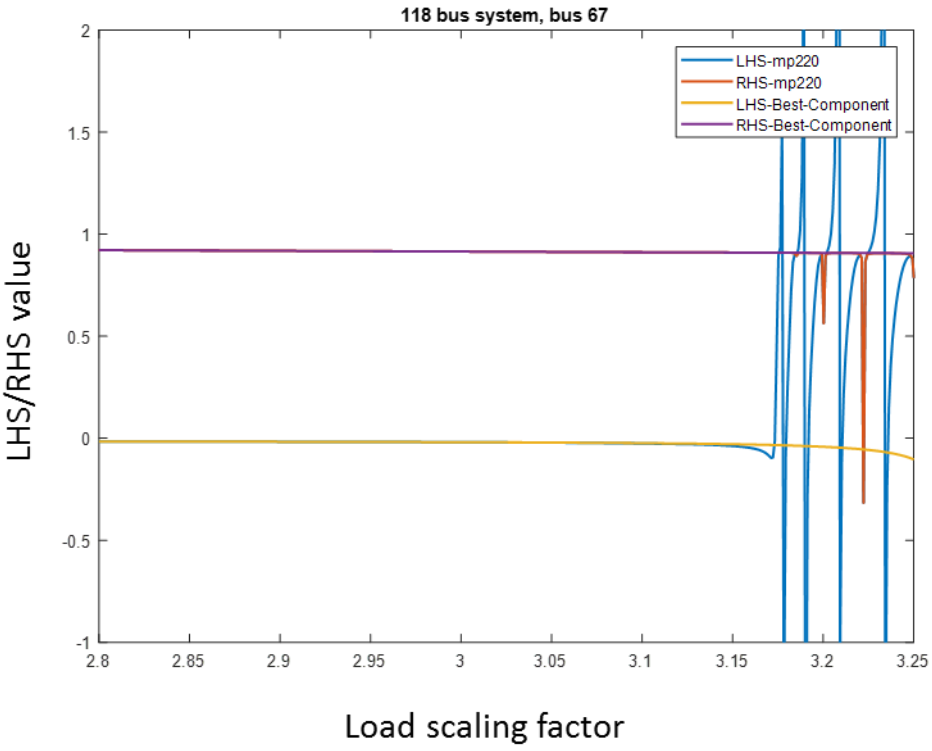

Figure 6.12 LHS and RHS of (6.25) at strong bus number 67 vs. the loading scaling factor for the modified 118 bus system

6.3.2.3 Polynomial Method

The Polynomial Method generates polynomials (rather than Padé approximants) of all functions of α in (6.25). To do that, each component in (6.25) needs to be reformulated to adapt to polynomial form. The process is described below:

The load voltage $V_L(\alpha)$ can be obtained as a Maclaurin series as given by (6.30) from HEM network reduction.

$$V_L(\alpha) = V_L[0] + V_L[1]\alpha + \cdots + V_L[n]\alpha^n + \cdots \tag{6.30}$$

The Maclaurin series for $Z_L(\alpha)$ is given by

$$Z_L(\alpha) = \frac{V_L(\alpha) \cdot V_L^*(\alpha)}{\alpha S^*} \tag{6.31}$$

Note that if the expression for $Z_L(\alpha)$ on the RHS of (6.31) is expanded as a power series

using (6.30), one will get a term with a negative exponent of α. The expression for $R_L(\alpha)$ will also have a term with a negative exponent of α. To avoid the negative exponent, the values of the load impedance and load resistance at different values of α can be obtained using the value of $\alpha Z_L(\alpha)$ and $\alpha R_L(\alpha)$ respectively. The corresponding Maclaurin series are given below:

$$\alpha Z_L(\alpha) = \frac{V_L(\alpha) \cdot V_L^*(\alpha^*)}{S^*} \tag{6.32}$$

$$\alpha R_L(\alpha) = Re\big(\alpha Z_L(\alpha)\big) \tag{6.33}$$

The value of $\partial R_L(\alpha)$ at different values of α can be obtained using the value of $\partial[\alpha R_L(\alpha)]/\partial\alpha$ as shown below:

$$\begin{aligned} &\frac{\partial \alpha R_L(\alpha)}{\partial \alpha} = \alpha \frac{\partial R_L(\alpha)}{\partial \alpha} + R_L(\alpha) \\ &\therefore \frac{\partial R_L(\alpha)}{\partial \alpha} = \frac{\left(\frac{\partial \alpha R_L(\alpha)}{\partial \alpha} - R_L(\alpha) \right)}{\alpha} \end{aligned} \tag{6.34}$$

By multiplying the top and bottom of (6.25) on both sides by α^2, one can obtain:

$$\frac{\partial |V_s(\alpha)|^2}{|V_s(\alpha)|^2} \frac{\alpha \cdot [\alpha R_L(\alpha)]}{\alpha \cdot [\alpha \partial R_L(\alpha)]} = \frac{|\alpha Z_L(\alpha)|^2 - \alpha^2 |Z_s|^2}{|\alpha Z_s + \alpha Z_L(\alpha)|^2} \tag{6.35}$$

Substitute (6.34) into the above equation, the modified MPTT equation for Polynomial Method is obtained, as given by (6.36).

$$\frac{\partial |V_s(\alpha)|^2}{|V_s(\alpha)|^2} \frac{\alpha \cdot [\alpha R_L(\alpha)]}{\alpha \cdot \partial[\alpha R_L(\alpha)] - \alpha R_L(\alpha)} = \frac{|\alpha Z_L(\alpha)|^2 - \alpha^2 |Z_s|^2}{|\alpha Z_s + \alpha Z_L(\alpha)|^2} \tag{6.36}$$

It can be observed that the reformulated equation given by (6.36) consists of six parts: ① $|\alpha Z_L(\alpha)|^2 - \alpha^2 |Z_s|^2$, ② $|\alpha Z_s + \alpha Z_L(\alpha)|^2$, ③ $\alpha \cdot [\alpha R_L(\alpha)]$,④ $\alpha \cdot \partial[\alpha R_L(\alpha)] - \alpha R_L(\alpha)$, ⑤ $|V_s(\alpha)|^2$, ⑥ $\partial |V_s(\alpha)|^2$. The next step is to figure out how

to get polynomials for ①-⑥ in (6.36) from pseudo-measurements, which are shown below:

①$|\alpha Z_L(\alpha)|^2 - \alpha^2|Z_s|^2$:

The n^{th} degree polynomial for $\alpha Z_L(\alpha)$ can be caluclated from αZ_L measurements over a range of loading values ($\alpha_k, k = 1,2, \dots N_{measure}$) using the polynomial fit techinique. The polynomial expression for $\alpha Z_L(\alpha)$, also named as $Z_1(\alpha)$, is shown in (6.37).

$$\alpha Z_L(\alpha) = Z_1(\alpha) = Z_1[0] + Z_1[1]\alpha + Z_1[2]\alpha^2 + \cdots + Z_1[n]\alpha^n \tag{6.37}$$

Once $\alpha Z_L(\alpha)$ is obtained, the $|\alpha Z_L(\alpha)|^2$, also labeled $Z_2(\alpha)$, can be calculated using (6.38):

$$\begin{aligned} |\alpha Z_L(\alpha)|^2 = Z_2(\alpha) &= Z_1(\alpha) \cdot Z_1^*(\alpha^*) \\ &= Z_2[0] + Z_2[1]\alpha + Z_2[2]\alpha^2 + \cdots + Z_2[2n]\alpha^{2n} \end{aligned} \tag{6.38}$$

Note that the $|\alpha Z_L(\alpha)|^2$ is represented as a 2n-degree polynomial instead of being truncated to an nth degree polynomial to avoid losing information from $Z_1(\alpha)$. The varible Z_s represents the source impedance obtained by network reduction and is a constant. Therefore, ① is obtained by adding (6.38) with the 2nd order term $\alpha^2|Z_s|^2$, is given by (6.39).

$$\begin{aligned} &|\alpha Z_L(\alpha)|^2 - \alpha^2|Z_s|^2 \\ &\quad = Z_2[0] + Z_2[1]\alpha + (Z_2[2] - |Z_s|^2)\alpha^2 + \cdots + Z_2[2n]\alpha^{2n} \end{aligned} \tag{6.39}$$

② $|\alpha Z_s + \alpha Z_L(\alpha)|^2$:

Similarly, the expression $\alpha Z_s + \alpha Z_L(\alpha)$ is obtained by adding (6.37) with a 1st order term αZ_s as given by (6.40).

$$|\alpha Z_L(\alpha)|^2 - \alpha^2|Z_s|^2 = Z_2[0] + Z_2[1]\alpha + (Z_2[2] - |Z_s|^2)\alpha^2 + \cdots + Z_2[2n]\alpha^{2n} \quad (6.40)$$

Then ② can be calculated using the following equation:

$$|\alpha Z_s + \alpha Z_L(\alpha)|^2 = Z_3(\alpha) = [\alpha Z_s + \alpha Z_L(\alpha)] \cdot [\alpha Z_s + \alpha Z_L(\alpha)]^* = Z_3[0] + Z_3[1]\alpha + \cdots Z_3[2n]\alpha^{2n} \quad (6.41)$$

③ $\alpha \cdot [\alpha R_L(\alpha)]$:

The polynomial for $\alpha R_L(\alpha)$ is calculated by taking the real part of $\alpha Z_L(\alpha)$, and then multiply it with α. The process is shown below:

$$\alpha R_L(\alpha) = R_1(\alpha) = Re\big(\alpha Z_L(\alpha)\big) = R_1[0] + R_1[1]\alpha + \cdots R_1[n]\alpha^n \quad (6.42)$$

$$\alpha \cdot [\alpha R_L(\alpha)] = \alpha R_1(\alpha) = R_1[0]\alpha + R_1[1]\alpha^2 + \cdots + R_1[n]\alpha^{n+1} \quad (6.43)$$

④ $\alpha \cdot \partial[\alpha R_L(\alpha)] - \alpha R_L(\alpha)$

The polynomial for $\partial[\alpha R_L(\alpha)]$ is obtained by taking the derivative of $\alpha R_L(\alpha)$ with respect to α as shown below:

$$\partial[\alpha R_L(\alpha)] = R_2(\alpha) = \frac{\partial R_1(\alpha)}{\partial \alpha} = R_2[0] + R_2[1]\alpha + \cdots R_2[n-1]\alpha^{n-1} \quad (6.44)$$

Then ④ is given by:

$$\alpha \cdot \partial[\alpha R_L(\alpha)] - \alpha R_L(\alpha) = \quad (6.45)$$

$$= \alpha \cdot (R_2[0] + R_2[1]\alpha + \cdots R_2[n-1]\alpha^{n-1}) - (R_1[0] + R_1[1]\alpha + \cdots R_1[n]\alpha^n)$$

$$= -R_1[0] + (R_2[0] - R_1[1])\alpha + \cdots + (R_2[n-1] - R_1[n])\alpha^n$$

⑤ $|V_s(\alpha)|^2$:

The n^{th} order polynomial for $V_s(\alpha)$ is obtained from the source voltage measurements using the polynomial fit technique and then ⑤ is obtained by using (6.46).

$$|V_s(\alpha)|^2 = V_s(\alpha) \cdot V_s^*(\alpha^*) \tag{6.46}$$

⑥ $\partial|V_s(\alpha)|^2$:

The term ⑥ is obtained by taking the derivative of the polynomial for ⑤ with respect to α.

The MPTT results using the Polynomial Method for weak bus 44 and strong bus 67 are plotted in Figure 6.13 and Figure 6.14 respectively. The labels "LHS-MODEL-Polynomial" and "RHS-MODEL-Polynomial" represent the LHS and RHS values, respectively, of (6.36) obtained using network reduction techniques [52]. The labels "LHS-Polynomial" and "RHS-Polynomial" represent the LHS and RHS values of (6.36), respectively, obtained by fitting measurements to a polynomial. Observe that the Polynomial Method can give a reasonable estimate (by using the divergence criterion in this case) when obtaining the power series from network reduction. However, when using the polynomials obtained from measurements, this method does not extrapolate the LHS well far away from the training data range. Therefore, use of the Polynomial Method is not feasible for predicting the SNBP.

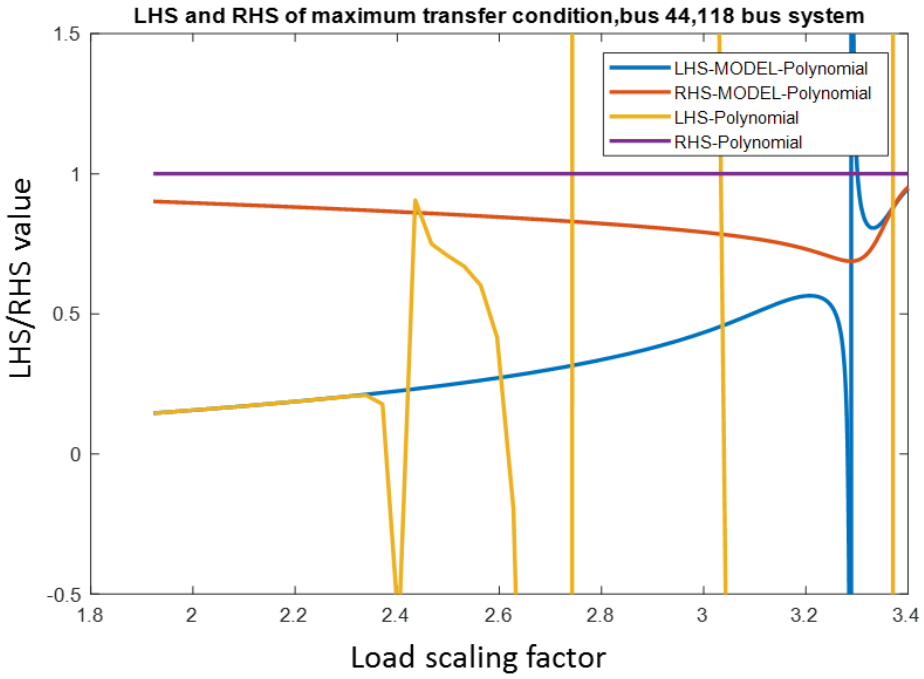

Figure 6.13 LHS and RHS of (6.36) at weak bus number 44 vs. the loading scaling factor for the IEEE 118 bus system

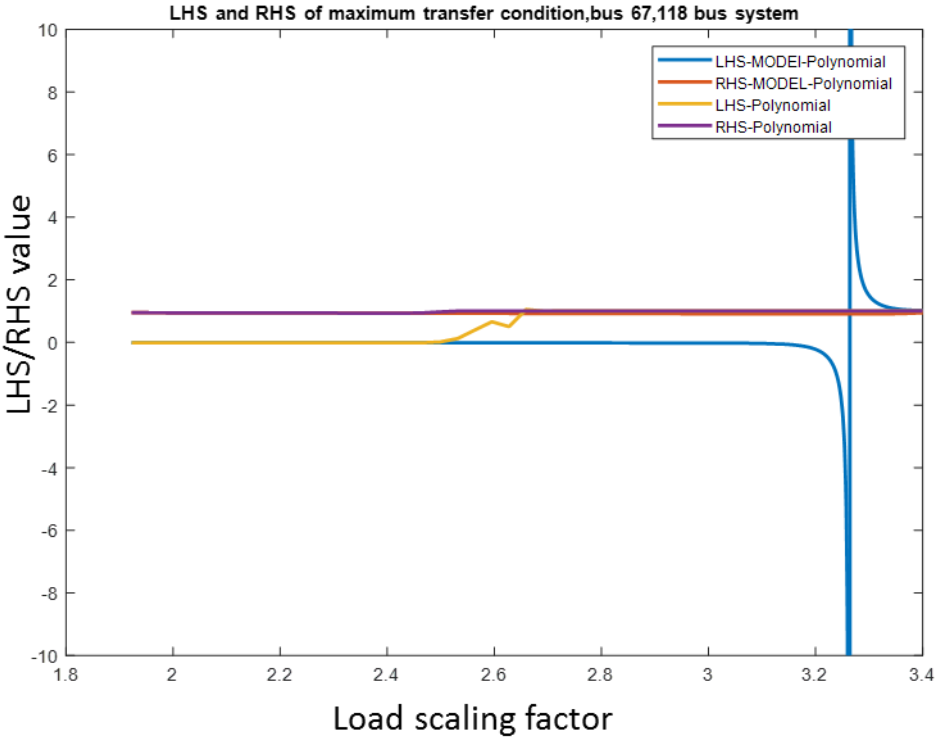

Figure 6.14 LHS and RHS of (6.36) at strong bus number 67 vs. the loading scaling factor for the IEEE 118 bus system

6.3.2.4 $Z_{th}(\alpha)$ method

The idea of the $Z_{th}(\alpha)$ method is similar to conventional TE-based method. The rest of the system is modeled as a voltage source connected through a Thévenin impedance as shown in Figure 6.15. Note that unlike the Thévenin-like network, in which the impedance Z_s from HE-reduction is constant, the Thévenin impedance in Figure 6.15 is a function of α. It can be calculated based on its definition:

$$Z_{th}(\alpha) = -\frac{\frac{\partial V_L(\alpha)}{\partial \alpha}}{\frac{\partial I_L(\alpha)}{\partial \alpha}} = -\frac{\partial V_L(\alpha)}{\partial\left(\frac{\alpha S^*}{V_L^*(\alpha^*)}\right)} = -\frac{\partial V_L(\alpha)\cdot V_L^*(\alpha^*)\cdot V_L^*(\alpha^*)}{S^*\left(V_L^*(\alpha^*) - \alpha\cdot\partial V_L^*(\alpha^*)\right)} \tag{6.47}$$

The load impedance $Z_L(\alpha)$ is given by:

$$Z_L(\alpha) = \frac{V_L(\alpha)\cdot V_L^*(\alpha^*)}{\alpha S^*} \tag{6.48}$$

The potential advantage of this approach is that at the SNBP, the magnitude of the Thévenin impedance is equal to the magnitude of the load impedance, i.e., $|Z_{th}(\alpha)| = |Z_L(\alpha)|$ and the test for the SNBP is much simpler.

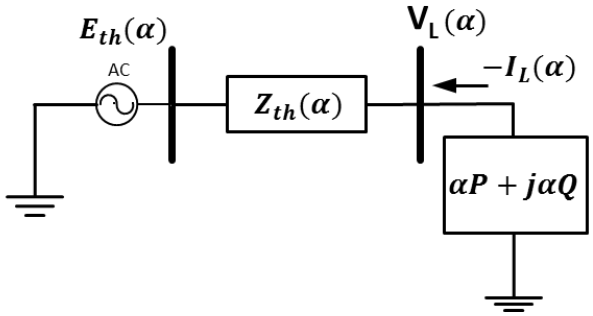

Figure 6.15 Two-bus equivalent diagram for $Z_{th}(\alpha)$ method

Plotted in Figure 6.16 is the magnitude of $Z_{th}(\alpha)$ and $Z_L(\alpha)$ vs. load-scaling factor for the IEEE 118 bus system with bus-of-interest being bus 48, a strong bus in the system. It is inferred that for strong buses, $Z_{th}(\alpha)$ method may reliably have a crossover while the Built-In/Self-Coded methods or Best Component method do not. Thus the $Z_{th}(\alpha)$ method can give a prediction of SNBP for strong buses while the Built-In/Self-Coded methods or Best Component method do not, because the LHS and RHS do not cross each other or diverge. However, this method gives a non-conservative estimate of SNBP. (In Figure 6.16, the estimate is around 3.3 while the SNBP loading value for the system is 3.187.) In addtion, uses the same assumption as TE-based method, namely that the voltage source remains constant during the sampling period. Therefore, this method will not be considered in later research work in this report. But it might show benefits when using noisy measurements.

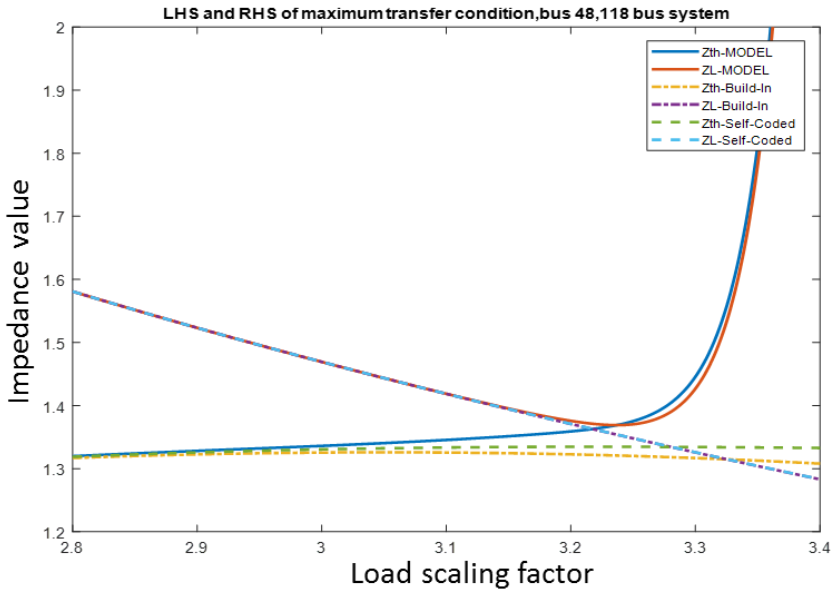

Figure 6.16 Magnitude of Z_L and Z_{th} at strong bus number 48 vs. the loading scaling factor for the IEEE 118 bus system

6.4 Validating the Maximum Power Transfer Theorem

As shown in section 6.3, when different numerical methods (including network reduction techniques which should be accurate to within roundoff error) are applied to MPTT, the SNBP could be predicted with acceptable accuracy for so-called weak buses, but not for so-called strong buses. To prove that the problem was not with the equation, but the precision with which the equation was evaluated, extended precision (250 digit) was used in generating the constituents of (6.25) for strong buses using network reduction techniques. As shown in Figure 6.17, when extended precision is used for strong buses, the LHS and RHS of (6.25) indeed are equal at the SNBP. (The calculated SNBP for the (non-modified) 118 bus system using extended precision is 3.189). Note that there is a “blip” in the LHS curve when using double precision and it might affect the accuracy of SNBP estimation in some cases. This behavior will be further discussed in later sections.

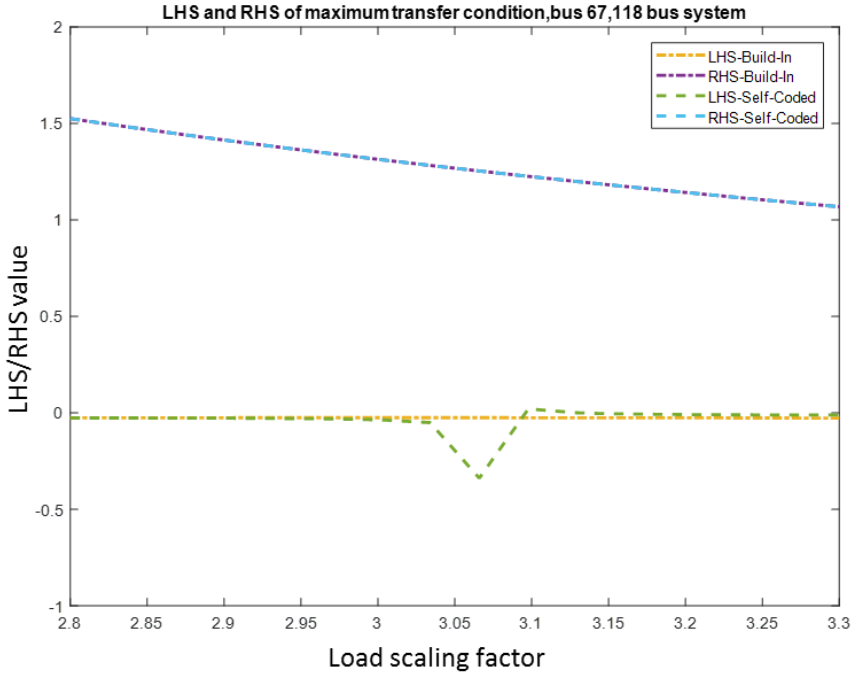

(a) Double precision

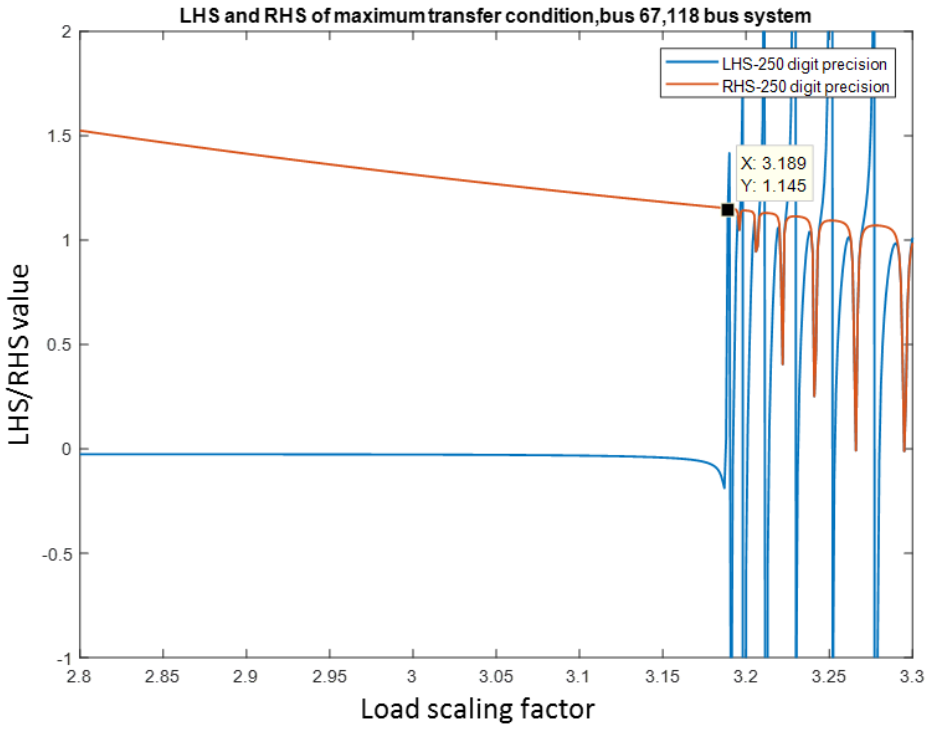

(b) 250 digits of precision

Figure 6.17 LHS and RHS of (6.25) at strong bus number 67 vs. the loading scaling factor for the IEEE 118 bus system

6.5 Numerical comparison of different methods using noiseless measurements

In the above section, the MPTT was validated by implementing it using high precision and, in section 6.3, different numerical methods were investigated to estimate the SNBP based on the MPTT from measurements. However, it was shown that, regardless of the method used, when only double precision is used the method cannot predict the SNBP using data from strong buses. Hence, to be effective, SNBP prediction algorithm should be applied to PMU buses that are close to weak buses in the system. Also it was observed from the above numerical experiments that the Built-In, Self-Coded and Best Component methods are promising if applied to weak buses, but their effectiveness is still not clear. Therefore, more extensive tests were conducted using these three methods with 11 weak buses on the 118 bus system in the following sections.

6.5.1 Modified 118 bus system

The tested 118 bus system is modified by adding S=1+1jMVA to bus 30, bus 37 and bus 38 in order to increase the number of testable weak buses in the system. (Because there is no real or reactive power load at those PQ buses in the original system, the MPTT could not be applied to those buses.) The loading value at the SNBP for this modified 118 bus system is 3.172, obtained using the CPF.

6.5.2 Finding the ten weakest buses from modal analysis

Arguably, the most well-known method of determining the weak buses of a system is modal analysis [54], which will be used here to determine the ten weakest buses of the modified 118 bus system.

The modal analysis method calculates the eigenvalue and eigenvector of the reduced Jacobian matrix based on the relation between the incremental bus voltage magnitudes and their respective incremental reactive power injections. The smallest eigenvalue can be used to estimate the stability margin and the participation factor calculated from the left and right eigenvectors corresponding to the critical mode helps provide insight about which bus loads may have significant impact on the system voltage stability. The buses with relatively large participation factors in the smallest eigenvalue are determined to be the weak buses in the system. Since modal analysis is based on a linear approximation of the system model, the order of the buses from the weakest to the strongest might change as the operating condition changes.

The top ten weakest buses (in decreasing order of weakness) obtained from modal analysis using VSAT [55] and our own MATLAB program for the modified 118 bus system are listed in Table 6.4 when the loading of the system is close to its SNBP. Note that when using VSAT to identify the weakest buses, we can only scale the system load up to 2.35 because VSAT can not give a converged solution beyond that. It can be observed that there is a one-to-one correspondence between VSAT and MATLAB program except for the 10^{th} weakest bus, i.e., the strongest one among the 10 weakest

buses. Thus, this shows that, in this case, the order of the top ten weakest buses changes slightly as the loading changes. The first nine weakest buses (identical for VSAT and MATLAB) and the 10th weakest buses both for VSAT and MATLAB, totaling eleven buses, are selected to be tested in the following section.

Table 6.4 Ten weakest buses for the modified 118 bus system using modal analysis

	VSAT (loading=2.35)		MATLAB (loading=3)	
Smallest eigenvalue	2.947722		3.035	
No.	Bus	Part.Fac.	Bus	Part.Fac
1	21	1	21	1
2	22	0.80834	22	0.83712
3	20	0.47027	20	0.46517
4	44	0.05503	44	0.04171
5	43	0.02785	43	0.0195
6	45	0.01984	45	0.01658
7	23	0.01407	23	0.01603
8	38	0.00313	38	0.00218
9	30	0.0006	30	0.00085
10	37	0.00016	17	0.00012

6.5.3 Numerical results

Numerical tests were conducted on the Built-In, Self-Coded and Best Component methods for the eleven weakest buses in the modified 118 bus system with different ranges of noiseless pseudo-measurements. In each experiment, 200 measurements were

used to fit a [30/30] Padé approximant for each variable. The SNBP was predicted either by the crossover or divergence behavior of the LHS and RHS values of the MPTT equation.The numerical results are shown as follows, where “Average error” is the average of the absolute value of the errors:

a. Measurements in the range of 50%-60% of the SNBP

In this experiment, the measurements in the 50%-60% training range were used to fit the Padé approximant. The percent error in SNBP for the 11 weakest buses using the three numerical methods are listed in Table 6.5 and the absolute value of the errors is shown in Figure 6.18.

Table 6.5 Percent error in SNBP estimation for measurements in the 50%-60% training range for the modified 118 bus system

Bus no.	Numerical methods			Average error over all methods
	Built-In	Self-Coded	Best Component	
21	4.17087	6.882093	8.237705	6.430223
22	12.16898	2.301387	2.04918	5.506515
20	2.175284	9.174023	6.052963	5.800757
44	-1.25158	0.29319	-0.05359	0.532787
43	-0.02207	0.576923	0.608449	0.40248
45	-1.8285	5.422446	5.453972	4.234973
23	-5.64313	12.54729	13.11475	10.43506
38	-2.60404	-0.81021	-1.50378	1.639344
30	0.063052	5.611602	-3.97226	3.215637
37	-0.90479	6.472257	7.796343	5.057797
17	-2.71122	13.52459	18.63178	11.62253
Average error over all buses	3.04941	5.783274	6.134071	4.988918

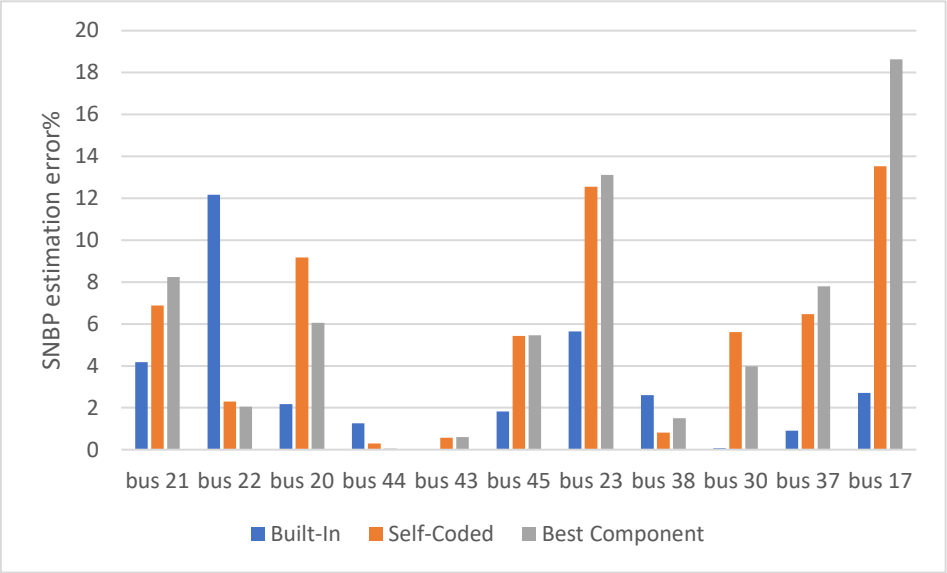

Figure 6.18 Percent error in SNBP estimation for measurements in the 50%-60% training range

b. Measurements in the range of 60%-70% of the SNBP

The numerical results of SNBP estimation using measurements in the 60%-70% training range are shown in Table 6.6 and Figure 6.19.

Table 6.6 Percent error in SNBP estimation for measurements in the 60%-70% training range for the modified 118 bus system

Bus no.	Numerical methods			Average error over all methods
	Built-In	Self-Coded	Best Component	
21	6.431274	4.854981	7.124842	6.137032
22	0.189155	-0.09458	-0.15763	0.147121
20	10.40353	8.228247	8.732661	9.12148
44	-8.62863	0.955233	1.144388	3.576082
43	0.797604	2.689155	2.058638	1.848466
45	-2.60404	0.513871	0.513871	1.210593
23	-14.029	4.287516	7.093317	8.469945
38	0.545397	-2.60404	-2.60404	1.917823
30	-5.42245	4.602774	3.87768	4.6343
37	2.657629	3.225095	3.571879	3.151534
17	2.900378	9.962169	8.417402	7.093317
Average error over all buses	4.964462	3.819787	4.117849	4.300699

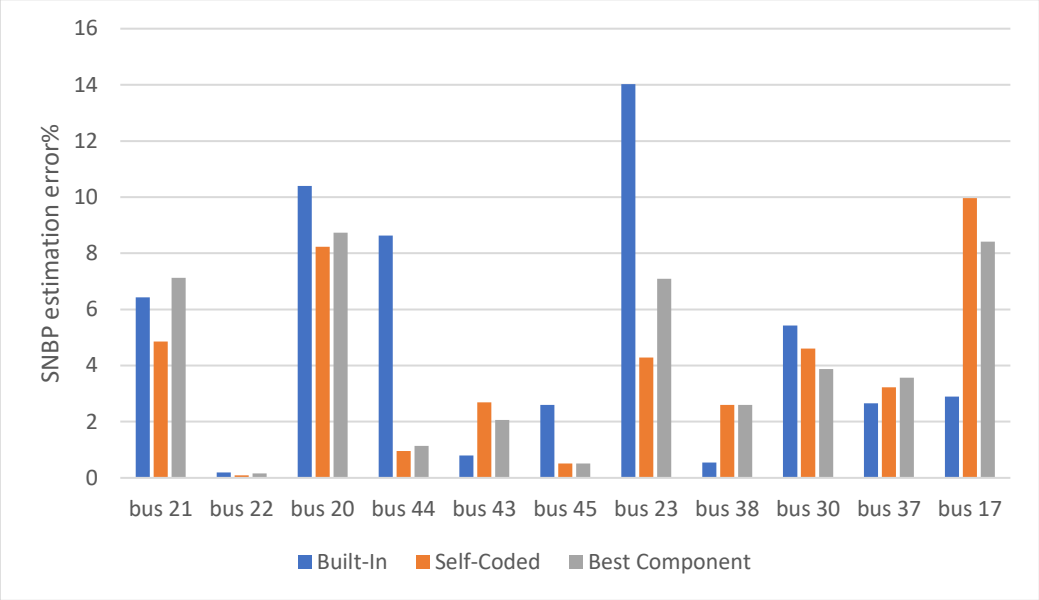

Figure 6.19 Percent error in SNBP estimation for measurements in the 60%-70% training range

c. Measurements in the range of 70%-80% of the SNBP

The numerical results of the SNBP estimation using measurements in the 70%-80% training range are shown in Table 6.7 and Figure 6.20.

Table 6.7 Percent error in SNBP estimation for measurements in the 70%-80% training range for the modified 118 bus system

Bus no.	Numerical methods			Average error over all methods
	Built-In	Self-Coded	Best Component	
21	0.094578	-0.44136	-0.50441	0.346784
22	1.481715	1.261034	0.031526	0.924758
20	1.680328	1.806431	0.040984	1.175914
44	-0.49496	-1.44073	-1.59836	1.178016
43	1.081337	-0.02207	-0.24275	0.448718
45	0.513871	0.040984	0.040984	0.198613
23	2.909836	1.869483	1.995586	2.258302
38	-0.36885	-0.46343	-0.58953	0.473939
30	0.135561	-0.84174	-0.84174	0.606347
37	0.671501	1.20744	1.302018	1.060319
17	2.373897	1.428121	1.428121	1.74338
Average error over all buses	1.073312	0.983893	0.783274	0.946826

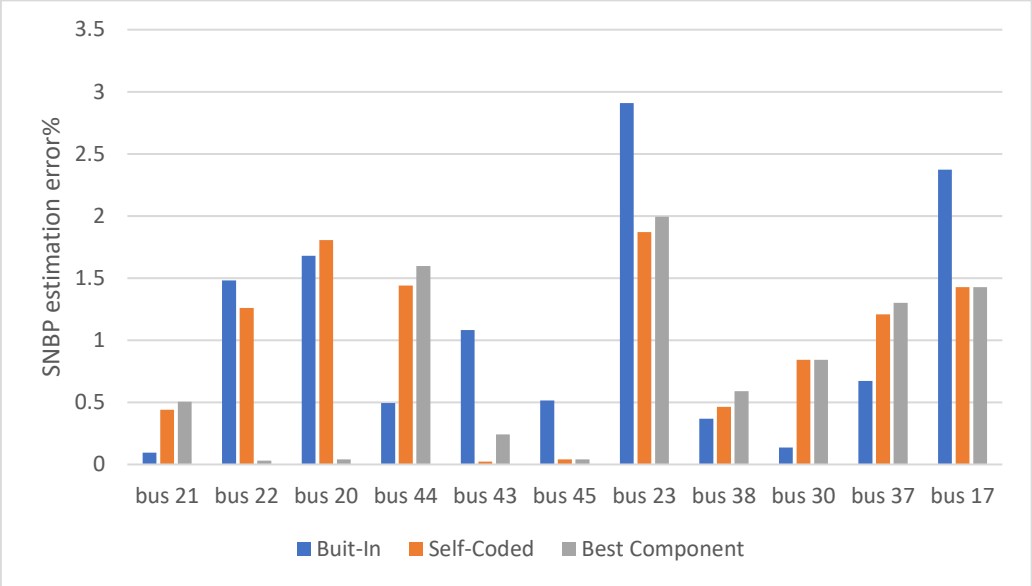

Figure 6.20 Percent error in SNBP estimation for measurements in the 70%-80% training range

6.5.4 Conclusion

From the above numerical results, it can be observed that the average errors in SNBP estimation using the three different methods are: 3%-6% for measurements in the 50%-60% range; 3%-5% for measurements in the 60%-70% range; about 1% for measurements in the 70%-80%. If simply taking the average of the average of the absolute values of the errors for the three methods, the approximate errors for each training data range are shown in Figure 6.21. It can be seen that the closer the measured data is to the SNBP, the smaller is the error in the SNBP estimate.

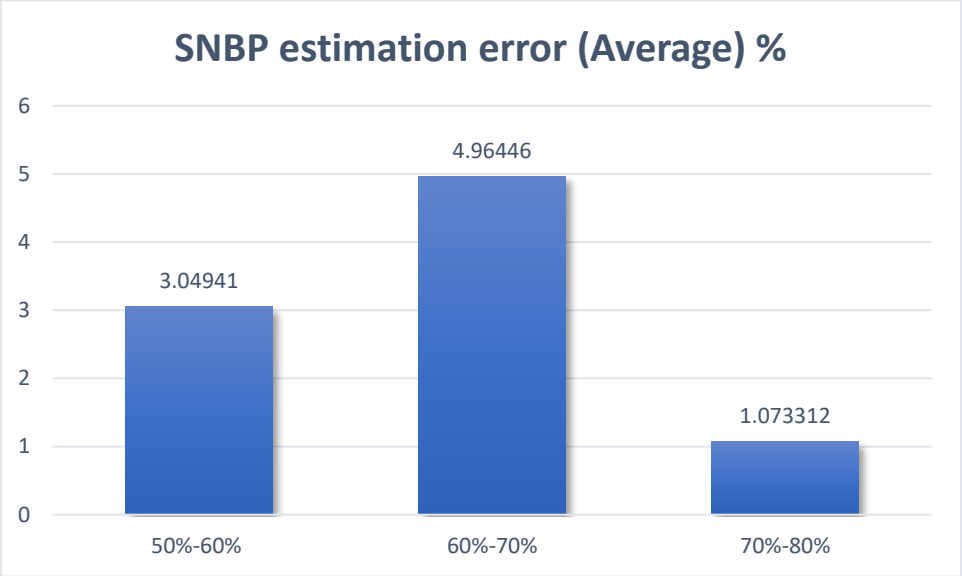

Figure 6.21 Percent error in SNBP estimation for different training data range (average the absolute value of errors)

If we average over the 11 weakest buses (no absolute value), the Built-In method gives the best results as shown in Figure 6.22. Other methods may be competitive if more sophisticated algorithms of outlier detection are used.

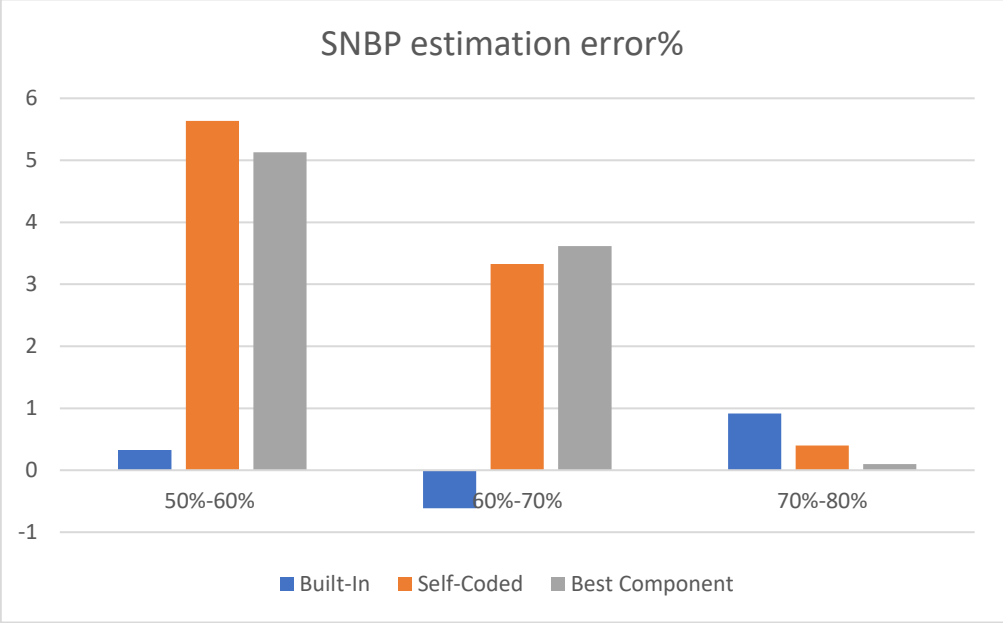

Figure 6.22 Percent error in SNBP estimation for different training data range (average errors)

6.5.5 More analysis on the numerical results

When the range of the measurement is 60%-70% of the SNBP, the numerical results as shown in Figure 6.19 show that the errors in SNBP estimation using the Built-In method for most buses are less than 7%, which is acceptable. However, the estimation error at bus 23 is 14.029%. (The estimated SNBP is 2.727 while the true SNBP of the system is 3.172), which obviously is an outlier. Hence, in order to improve the accuracy of our method for estimating the SNBP, we will focus on finding the cause of this outlier. Bus 43, for which the estimation error is only 0.797%, is also included in the following tests for comparison.

If we generate the MPTT plot for bus 23 as shown in Figure 6.23 (a), it can be observed that the yellow line which represents the LHS of (6.25) has a spike at around 2.727 and this point will be detected as the SNBP by the divergence criteria, which is incorrect. Then by analyzing each component in the LHS of (6.25) ($\partial|V_s|^2, \partial R_L(\alpha), R_L(\alpha)$ and $|V_s|^2$), we find that the cause comes from $\partial|V_s|^2$ as shown in Figure 6.24 (a).

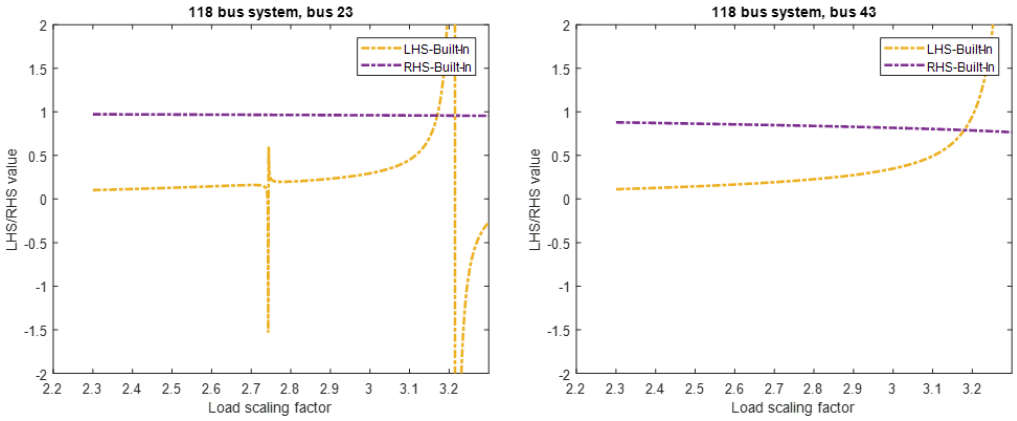

(a) Bus 23 (b) Bus 43

Figure 6.23 LHS and RHS of (6.25) at bus 23 or bus 43 vs. loading scaling factor

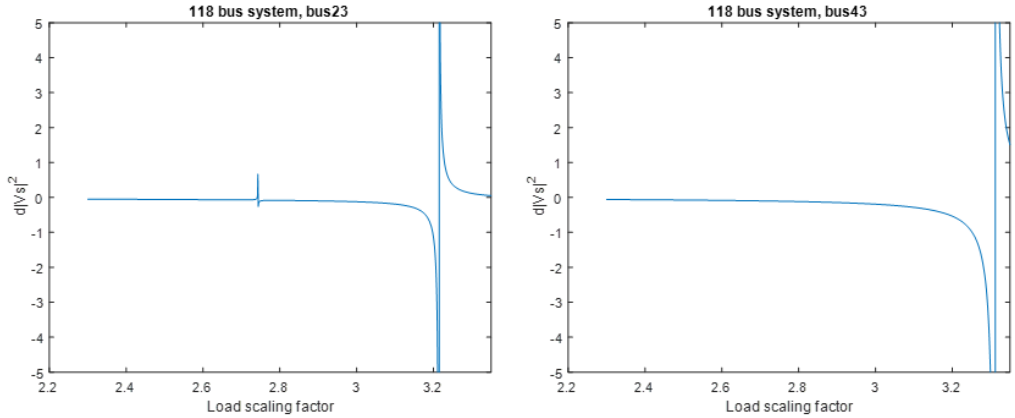

(a) Bus 23 (b) Bus 43

Figure 6.24 $\partial|V_s(\alpha)|^2$ at bus number 23 or bus 43 vs. loading-scaling factor

To dive further into determining the root cause of blip in Figure 6.24 (a), the poles and zeros of the Padé approximants of $\partial|V_s|^2$ for bus 23 and bus 43 are plotted in Figure 6.25. It can be seen that there are a number of poles/zeros accumulating on the real axis in the range [1.9, 2.22], which is the measured data range. Since we only focus on the range beyond the measured data range for estimating the SNBP, these poles/zeros will not affect the estimation. And the pole/zero that is located at around 3.4 should be the actual root of the Padé approximant obtained from measurements and will be taken as the estimated SNBP if using the roots method. (Using the roots method, an estimated

SNBP of 3.4 is significantly inaccurate, which is why the MPTT is used.) Observe that for bus 23, there is a pole-zero pair in the range between the boundary of the measured data range and the root of the Padé approximant, located at around 2.73 (also inaccurate if the roots method were to be used) and this pole-zero pair will affect the behavior of the LHS and RHS of (6.25). Therefore, when we search for the estimated SNBP detected by crossover or divergence behavior starting from the boundary of the measured data range, the estimation of the SNBP is 2.727, which is incorrect. More discussion on the poles and zeros of the Padé approximant obtained from measurements will be conducted in section 6.6, as will suggested remedies for this problem. As will be seen in section 6.6, this pole-zero pair for bus 23 is caused by round-off error.

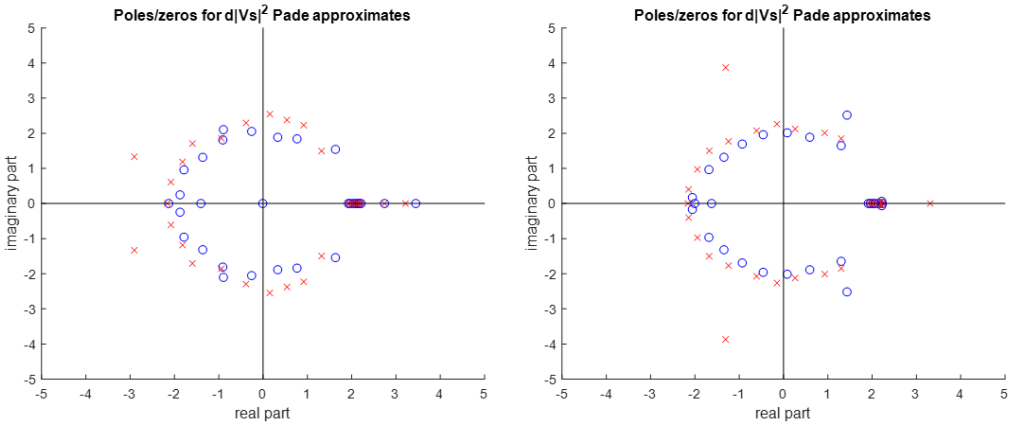

(a) Bus 23 (b) Bus 43

Figure 6.25 Pole-zero plot for $\partial|V_s(\alpha)|^2$ at bus number 23 and bus 43

6.6 Using the roots method to estimate the SNBP

In addition to using the MPTT, one can use the roots (poles/zeros) of the voltage Padé approximant to estimate the SNBP using the so-called roots method. As seen in

section 6.5.5, the location of the poles/zeros of the Padé approximant is an effective way to analyze numerical issues. Hence the numerical performance of the roots method will be discussed in the following section.

6.6.1 The effect of order of Padé approximant

The pole-zero plots for different orders of [*M*/*M*+1] Padé approximants of V_L at bus 23 are plotted in Figure 6.26 using various numbers of series term (*n*). The range of the measurements used to fit the Padé approximant is 60%-70% of the SNBP, which is 1.9032 to 2.2204 in α values. The total number of measurements is 200. It is seen from Figure 6.26 (a) that when the number of terms, n, used to calculate the Padé approximants is insufficient, like *n*=4 in this case, there is no pole/zero on the real axis and thus no SNBP prediction can be made using the roots method. Looking at Figure 6.26 (b) (c) and (d),we observe that the pole/zero that is located at around 3.4 is viewed to be the actual root of Padé approximants of V_L fitted from measurements and will be referred to "the meaningful" pole/zero in the rest of the work. It was observed that the location of the meaningful pole/zero changes slightly as *n* changes. However, as *n* increases, beyond a certain threshold, as seen in Figure 6.26 (c), poles/zeros occur on the real axis inside and just beyond the training data range, i.e., [1.9032, 2.2204]. This type of poles/zeros will be referred to "training range" poles/zeros. When *n*=20, those training range poles/zeros are all within the training data range and thus will not affect the accuracy of the SNBP estimation. When *n* increases to 50, as shown in Figure 6.26

(d), many poles/zeros accumulating on a circle centered at the origin, which will be referred to as "the circle" poles/zeros in the following sections. Also, observe in Figure 6.26 (d) that there is an (approximately real-valued) near-training-range pole/zero located at 2.312, which is beyond the training data range and would be taken as the estimated SNBP from roots method, leading to inaccuracy in SNBP prediction.

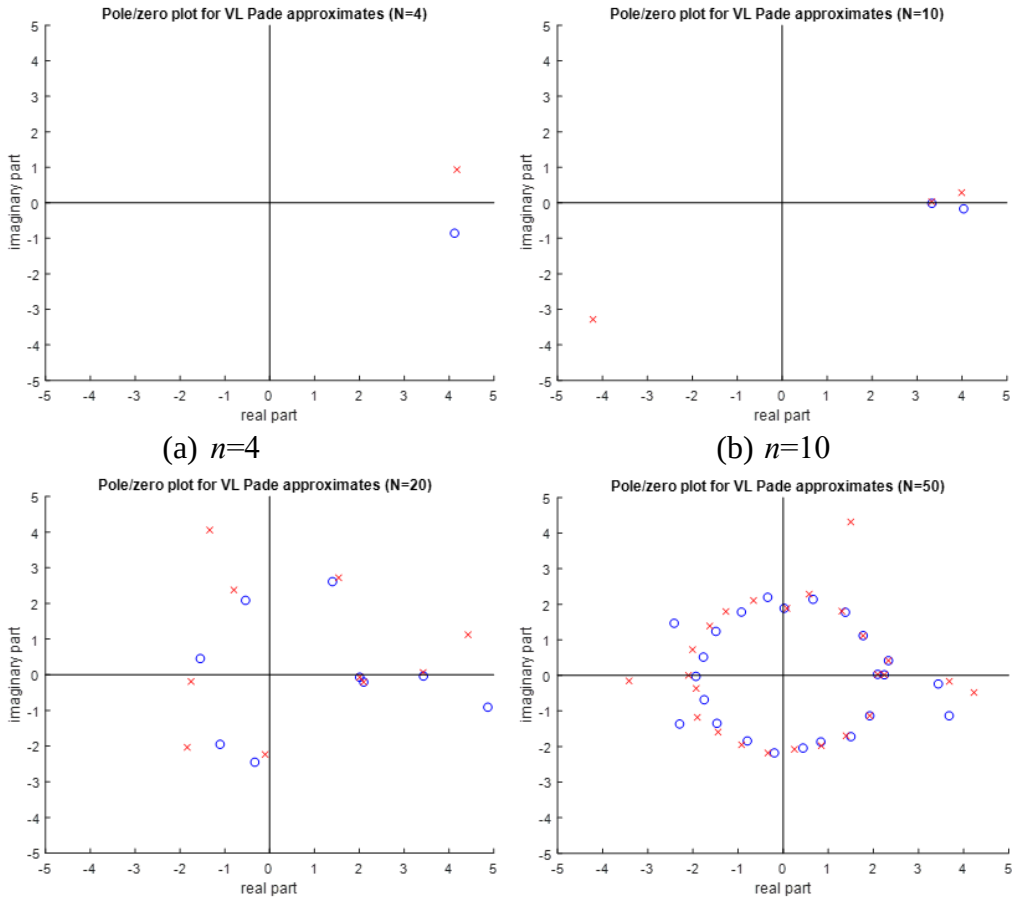

(a) n=4 (b) n=10

(c) n=20 (d) n=50

Figure 6.26 Pole-zero plot for different order of V_L Padé approximant

Let us define the following variables.

- N_{start} is the number of terms at which the Padé approximant starts to have a pole/zero on or near the real axis, which consequently would allow the prediction of the SNBP by the roots method (as seen in Figure 6.26 (b)) to be

reasonably accurate,

- N_{range} is the number of terms at which the Padé approximant starts to have training range poles/zeros all in the training range but these roots remain within the training range so they do not affect the accuracy of the SNBP estimation (as seen in Figure 6.26 (c))
- N_{bad} corresponds to the number of terms of the Padé approximant when there exist training range poles/zeros located beyond the training data range as more and more spurious poles/zeros appear, thus causing estimation errors (as seen in Figure 6.26 (d)).

The general conclusion from a series of tests on the modified 118 bus system is that in general: $N_{start} = 7$, $N_{range} = 12$ and $N_{bad} = 21$. The specific SNBP estimation results for bus 23 are shown in Figure 6.27.

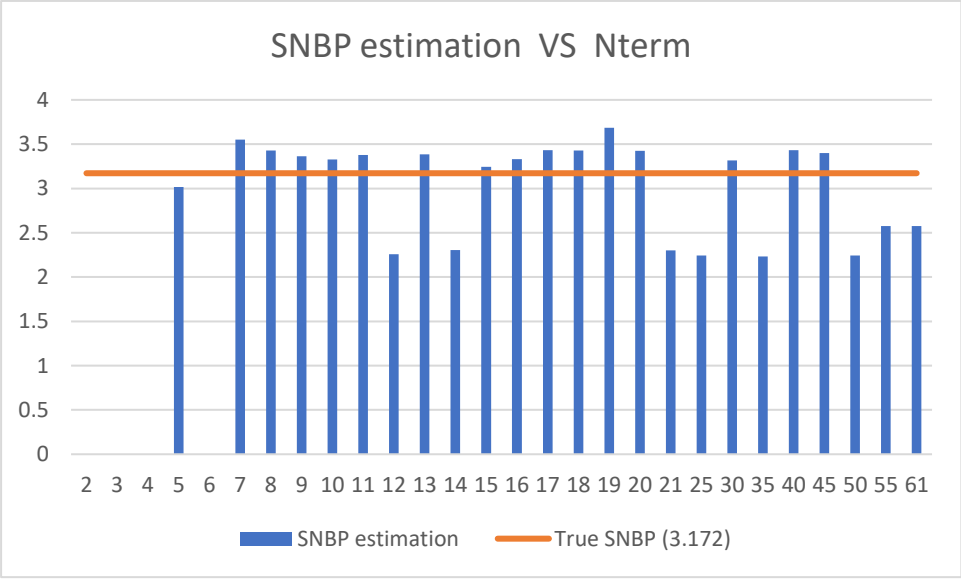

Figure 6.27 The estimation of SNBP vs. number of series terms used in building the Padé approximant of V_L using 200 measurements

As seen from Figure 6.27, one does not need many terms to obtain a reasonably accurate estimate of the SNBP and using too many terms will reduce the accuracy of the estimation eventually. Typically, n=12 to 20 will give a reasonably good SNBP estimation.

6.6.2 The effect of number of measurements

As demonstrated in section 6.3.1, the Padé approximant is calculated by solving a set of overdetermined equations. Increasing the number of measurements is expected to reduce round-off error. If we repeat the simulation in section 6.6.1 with 2000 measurements, the result we obtain is: $N_{start} = 5$, $N_{range} = 18$ and $N_{bad} = 24$, which means we can use a wider range of n selections and still obtain a good estimate. The specific SNBP estimation results are shown in Figure 6.28. Notice that the SNBP estimate is more reliable when 2000 samples are used versus 200 samples, as shown in Figure 6.27.

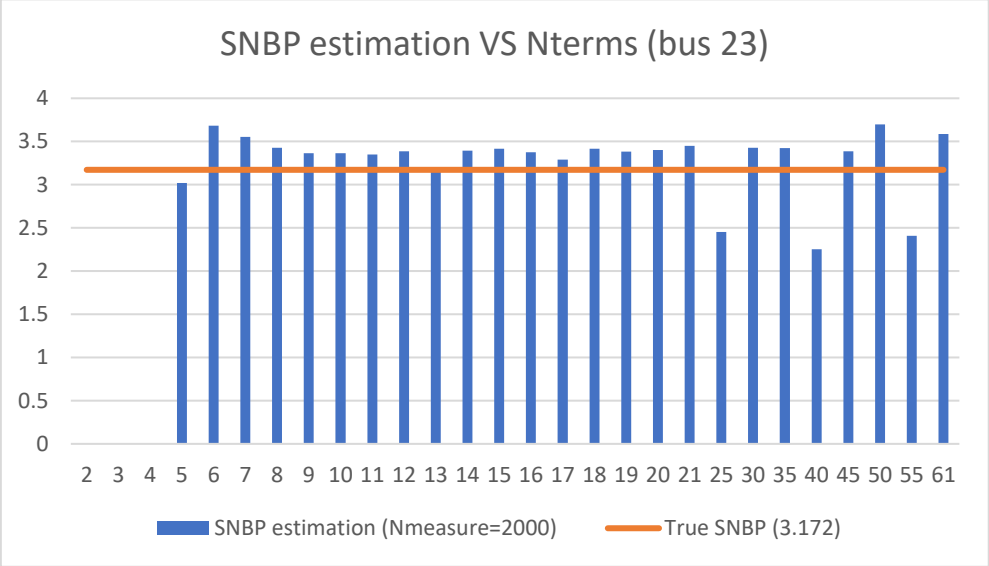

Figure 6.28 The estimation of SNBP vs. number of series terms used in building the Padé approximant of V_L using 2000 measurements

6.6.3 The effect of precision

As shown in Figure 6.27, we classify three types of poles/zeros of the Padé approximant by their locations: meaningful pole/zero, training range pole/zero, and circle pole/zero. To have a better understanding of which factors affect the locations of those roots, we implemented a high precision code that we used to perform the following tests. We recognized that spurious roots could be caused by errors in either the measurements or the calculation of the Padé approximant. Therefore, we implemented out training algorithm with different numbers of digits of precision in both obtaining the pseudo-measurements and fitting the Padé approximants. The simulation results are shown in Figure 6.29, Figure 6.30, and Figure 6.31. The number of terms used here is 50.

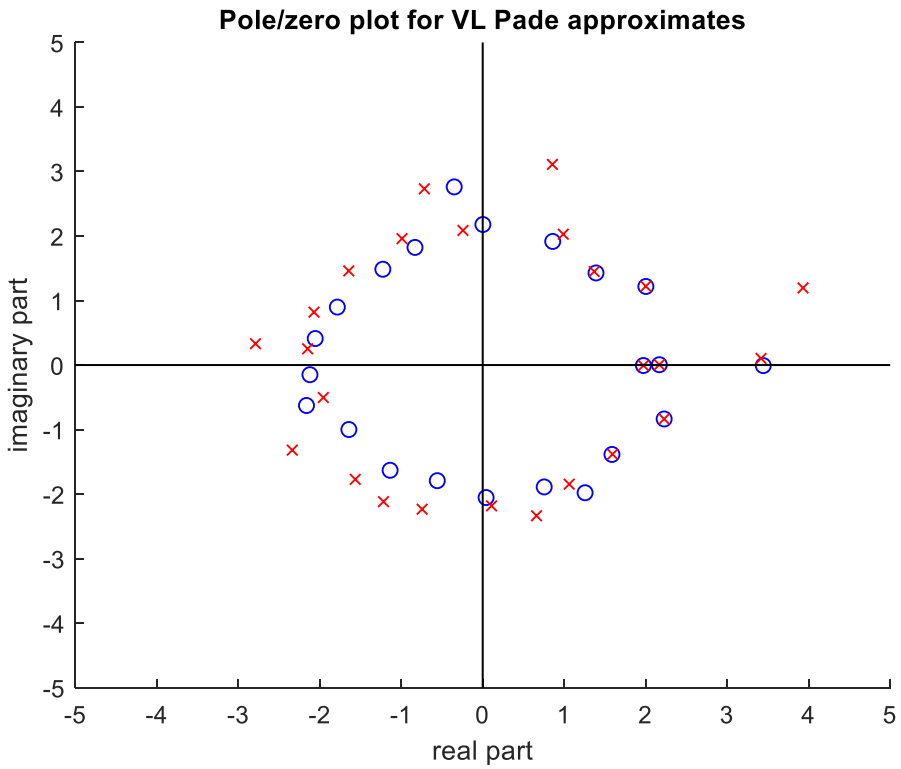

Figure 6.29 Pole-zero plot for V_L Padé approximant for the modified 118 bus system (double precision measurements, double precision Padé approximant)

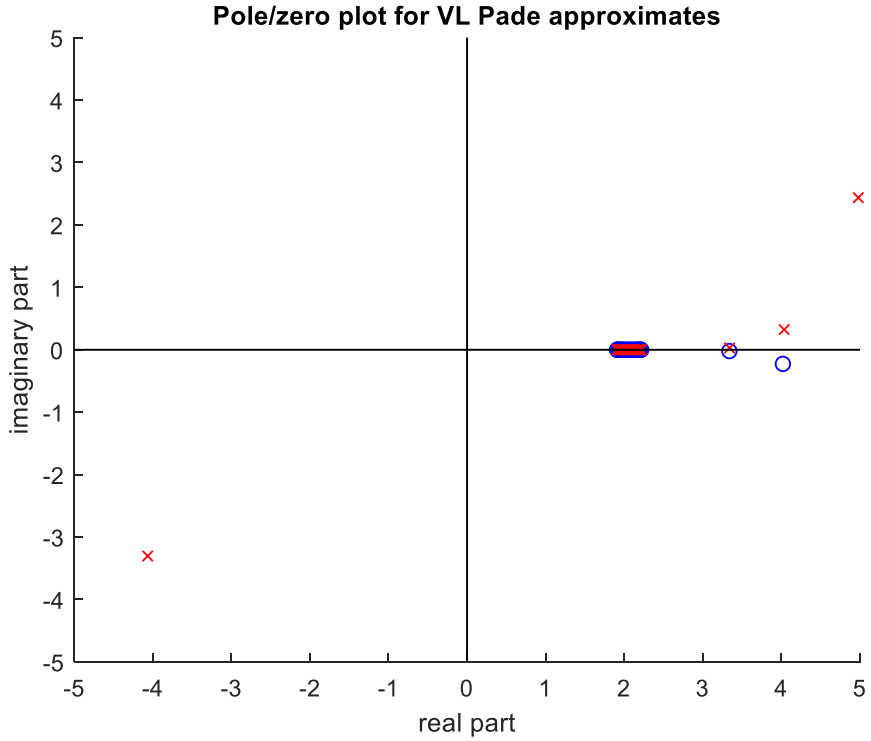

Figure 6.30 Pole-zero plot for V_L Padé approximant for the modified 118 bus system (double precision measurements, 220 digits of precision Padé approximant)

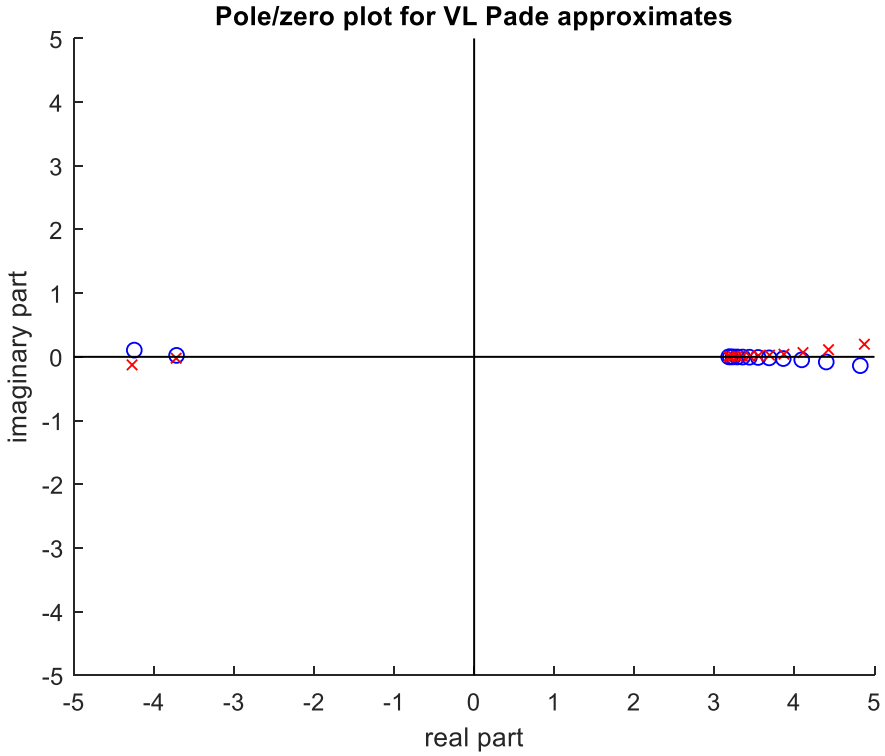

Figure 6.31 Pole-zero plot for V_L Padé approximant for the modified 118 bus system (220 digits of precision measurements, 220 digits of precision Padé approximant)

By comparing Figure 6.29 and Figure 6.30, we can see that the circle poles/zeros disappear when using high precision to fit the Padé approximants. Therefore, the circle poles/zeros are in fact spurious roots due to round-off errors during the calculation of the Padé approximant coefficients. Note that the circle poles/zeros in Figure 6.29 seem to move to the training data range as shown in Figure 6.30 and the location of the meaningful poles/zeros does not change much when using high precision to fit the Padé approximants.

By comparing Figure 6.30 and Figure 6.31, we can see that the training range poles/zeros disappear if both measurements and Padé approximants are calculated with high precision. In addition, the meaningful poles/zeros are closer to the true SNBP of the system (the meaningful pole/zero is located at 3.34 and 3.172 in Figure 6.30 and Figure 6.31 respectively). Therefore, we can conclude that the occurrence of those training range poles/zeros comes from measurement errors. Also, obtaining a more accurate estimation of the meaningful pole requires using high precision for both measurements as well as Padé approximants. Given that precision is limited from PMU measurements (maybe 3-4 accurate digits, if noise is minimal), accurately predicting the SNBP from measured data will require more elaborate means than the simple roots method.

In summary, in order to improve the accuracy of roots method for estimating the SNBP, one should focus on reducing measurement noise or eliminating spurious poles/zeros caused by the computation of Padé approximants.

6.6.4 Comparison of the MPTT and the roots method

The comparison of SNBP estimation error produced by the MPTT using the Built-In method and the roots method was performed using the eleven weakest buses for the modified 118 bus system. The measurements in the 60%-70% range were used to fit the Padé approximant, obtained using MATPOWER with a power-mismatch convergence tolerance of 10^{-8}. The numerical results are shown in Figure 6.32 where mp120 represents using 120 digits of precision to fit the Padé approximants. The error in the SNBP estimation is the average of the absolute errors for all buses shown in Figure 6.32.

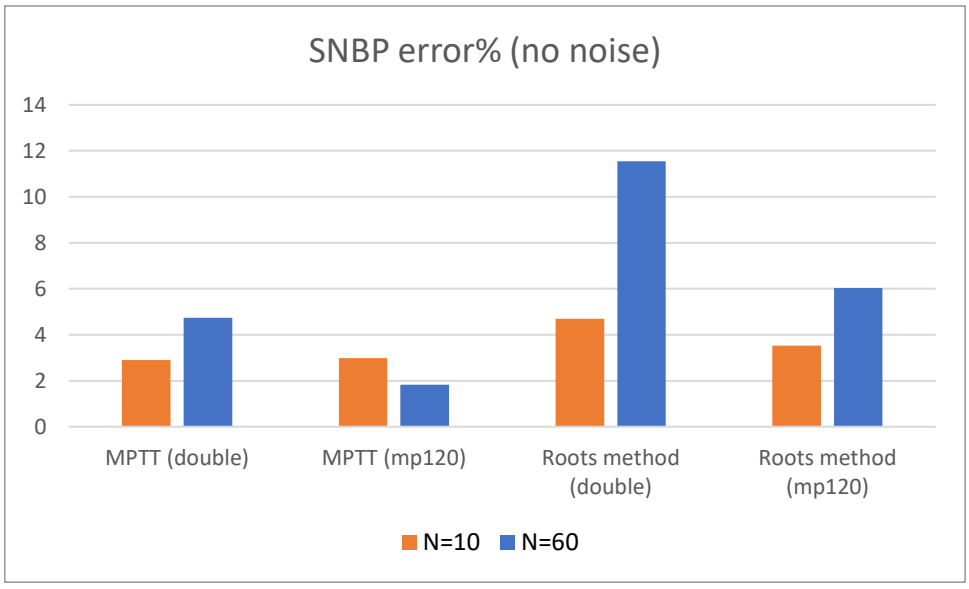

Figure 6.32 Comparison of MPTT and roots method for estimating the SNBP

From Figure 6.32 we can conclude that:

(1) The MPTT method can give more accurate results than the roots method for the system test. The roots method is more sensitive to the number of terms and digits of precision used for the Padé approximant.

(2) Reducing the order of Padé approximant (for example, using n=10 instead of n=60 in this case) helps to eliminate estimation errors with the roots method and with the MPTT method when using double precision.

(3) Increasing precision can improve accuracy, which is expected. But when we use a small-order Padé approximant (n=10 for example), the effect of precision is not as significant.

Therefore, generally, estimating the SNBP using the MPTT method with double precision and n=10 for the Padé approximant seems to be a prudent choice. More numerical experiments on a wide variety of systems is needed to confirm this hypothesis.

6.7 Numerical comparison of different methods using noisy measurements

6.7.1 Numerical results

We inserted random noise (zero mean, standard deviation of 0.01) in a range of PMU voltage pseudo-measurements from the modified 118 bus system and repeated the same numerical tests as presented in section 6.5. The numerical results we obtained are shown in Table 6.8 and Figure 6.33. The average error in SNBP estimation for a 70%-80% training range is around 15%, which is unacceptable. The poles/zeros of the

Padé approximant for bus 23 are plotted in Figure 6.34. It is observed that there are no meaningful poles/zeros in this plot because of the corruption of the measurements by noise; therefore, neither the MPTT method nor the roots method works and more research is needed in the future to develop different methods for ameliorating measurement error.

Table 6.8 Percent error in SNBP estimation for noisy measurements in the 70%-80% training range for the modified 118 bus system

Bus no.	Numerical methods			Average error over all methods
	Built-In	Self-Coded	Best Component	
21	-19.4515	-19.1362	-16.6141	18.40059
22	-19.4515	-17.8752	-19.4515	18.92602
20	-19.1362	17.74905	-4.6343	13.83985
44	11.44388	-15.0378	-15.3531	13.94493
43	-13.4615	-7.47163	-11.2547	10.7293
45	-19.4515	-19.4515	-19.1362	19.34636
23	-16.2989	-7.78689	-19.4515	14.5124

38	-17.2446	-19.4515	-19.4515	18.71585
30	-11.57	-19.4515	6.399748	12.47373
37	-15.6683	-18.8209	-19.4515	17.98024
17	-10.6242	-0.8512	-15.9836	9.153005
Average error over all buses	15.80018	14.82575	15.19833	15.27475

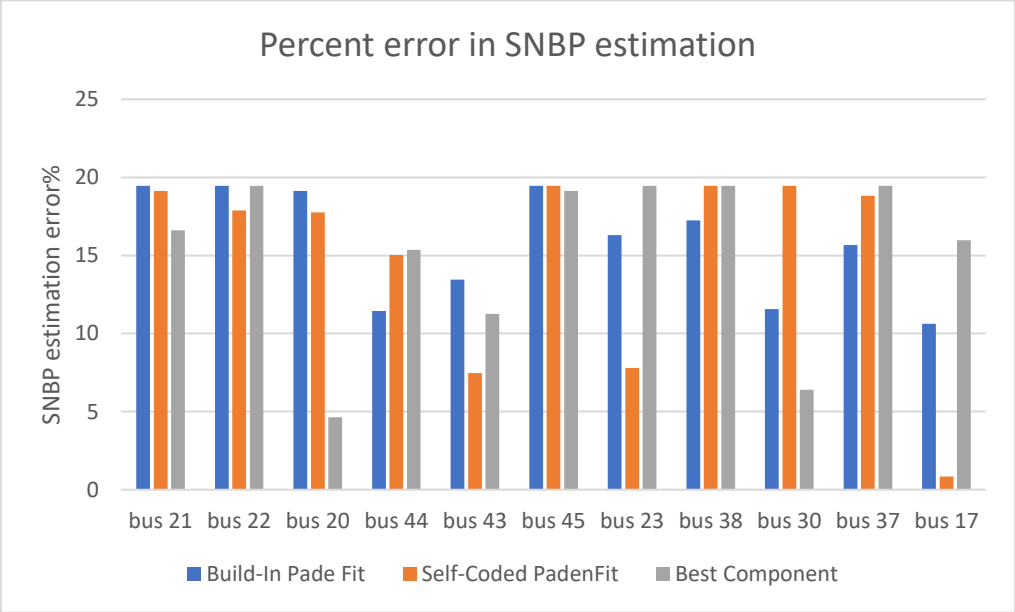

Figure 6.33 Percent error in SNBP estimation for noisy measurements in the 70%-80% training range

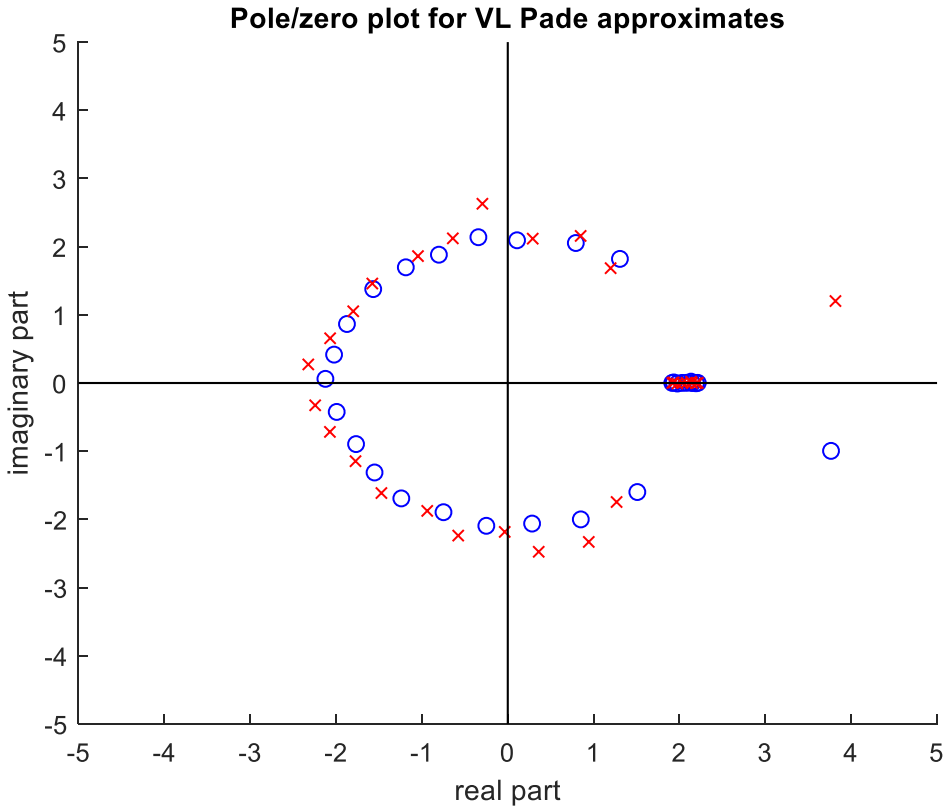

Figure 6.34 Pole-zero plot for V_L Padé approximant with noisy measurements

6.7.2 Analytic Derivative method

In the above tests, the components $\partial|V_s(\alpha)|^2$and ∂R_L in the MPTT were obtained by directly fitting the corresponding Padé approximant from the corresponding numerically calculated incremental values, i.e., the numerically calculate voltage and load resistance increments (i.e., subtraction of adjacent measurements), respectively. Even relatively small deviations in these measurements from the true values (due to measurement noise) will have a large effect on the value of the increment, and therefore on the derivative. To eliminate the use of the numerically calculated incremental values,

another fitting technique was developed, specifically the "Analytic Derivative" method, introduced next.

In the Analytic Derivative method, rather than taking the derivative numerically by subtracting adjacent measurements, the Padé approximant of the needed function is first constructed and then the derivative of this function is performed analytically. For example, the Padé approximant for $\partial|V_s(\alpha)|^2$ is obtained by first fitting the Padé approximant to $|V_s(\alpha)|^2$ from the square of the magnitude of the source voltage measurements and then taking the derivative of this rational function. The approach to getting the Padé approximant for ∂R_L is similar. The MPTT results using the Analytic Derivative method for weak bus 22 in the modified 118 bus system from noiseless measurements is plotted in Figure 6.35 and compared with the results from the Built-In method. The measurement range is 60%-70% of the SNBP load, i.e., α in the range $1.9032<\alpha<2.2204$. It is shown that the Analytic Derivative method does not perform as well as the Built-In method because the LHS of the MPTT for the Analytic Derivative method deviates from the true curve earlier than the Built-In method. Is is believed that performance is inferior in case with noiseless measurements because the process of taking the derivative for $\partial|V_s(\alpha)|^2$ and ∂R_L produces roundoff error.

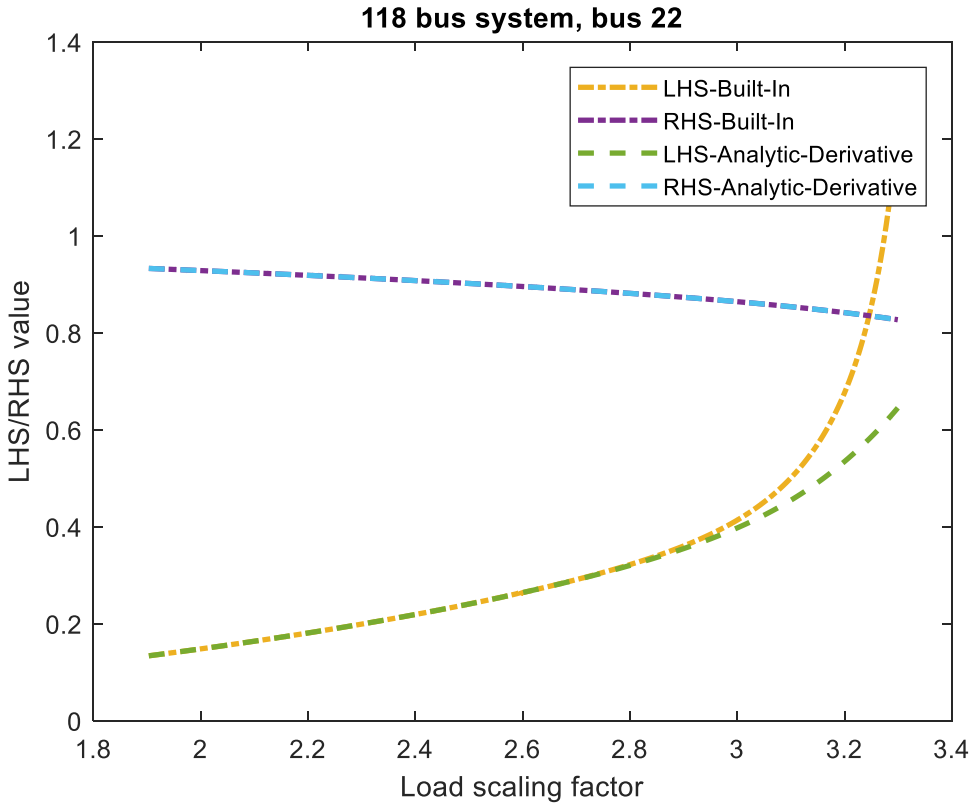

Figure 6.35 LHS and RHS of (6.25) at weak bus number 22 vs. the loading scaling factor for the modified 118 bus system using noiseless measurements

Next, we inserted random noise (zero mean, standard deviation of 10^{-9} and 10^{-6}) into the voltage measurements and repeated the above numerical tests. The MPTT results using noisy measurements with a standard deviation of 10^{-9} and 10^{-6} are shown in Figure 6.36 and Figure 6.37, respectively. We can see that when using measurements with noise, the Analytic Derivative method performs better than the Built-In method because it avoids the use of numerically calculated incremental values. However, this method is still not able to estimate the SNBP with acceptable accuracy. More effort is needed to improve the numerical performance.

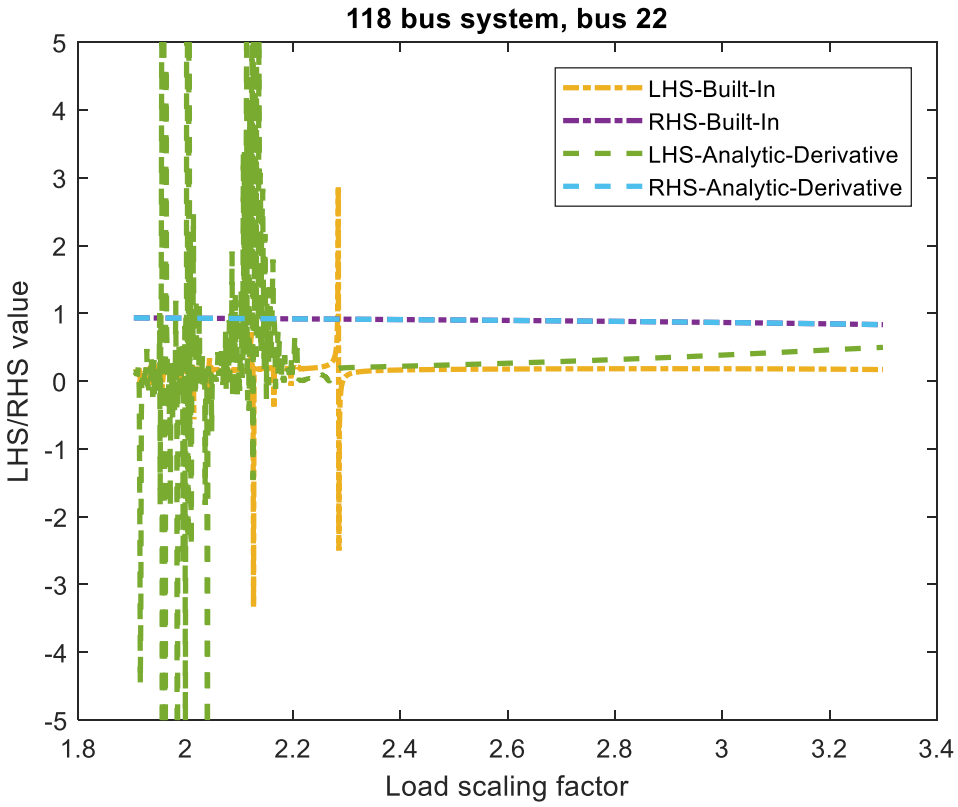

Figure 6.36 LHS and RHS of (6.25) at weak bus number 22 vs. the loading scaling factor for the modified 118 bus system using noisy measurements with standard deviation of 10^{-9}

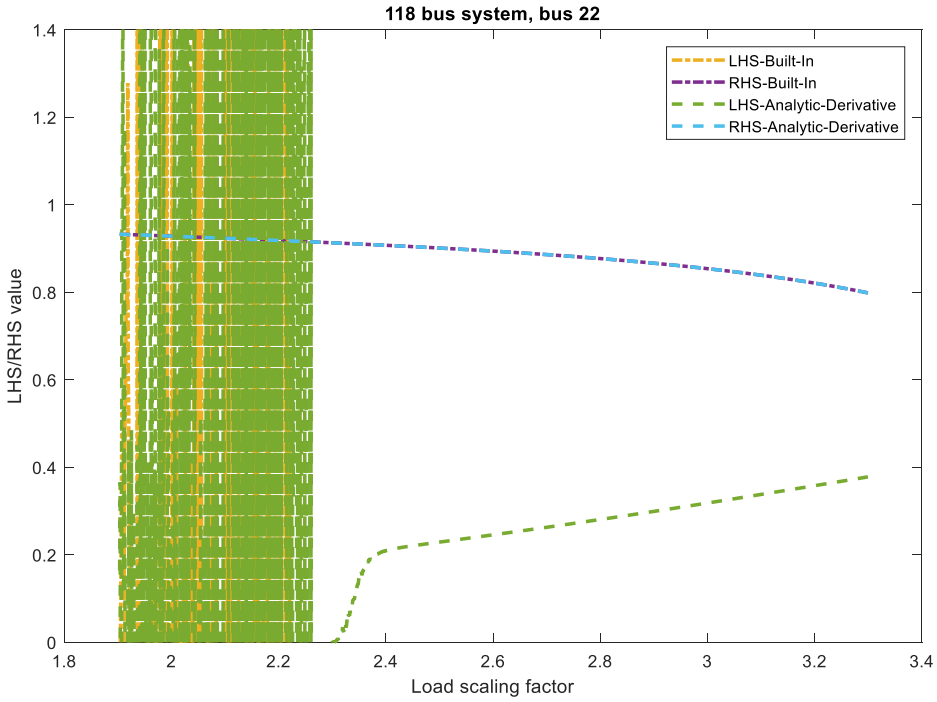

Figure 6.37 LHS and RHS of (6.25) at weak bus number 22 vs. the loading scaling factor for the modified 118 bus system using noisy measurements with standard deviation of 10^{-6}

6.7.3 Summary

From above tests, we see that the noise in the measurements (whether injected, or inherent as roundoff error in the calculation of the pseudo-measurements) has a similar effect on poles/zeros as roundoff error (generated in the calculation of the Padé approximant). They lead to spurious roots in the Padé approximant and affect the accuracy of the non-spurious poles/zeros and the accuracy of the SNBP prediction. It is important to develop methods to eliminate the effect of noise, which is left as future work.

6.8 Summary

This chapter concentrates on the application of HEM to the estimation of the SNBP using local-measurements. We developed a nonlinear Thévenin-like network from HE reduction and establish the Maximum Power Transfer Theorem for estimating the SNBP, which has been validated using high precision. Different numerical methods are investigated and the comparison of their numerical performance is conducted on a modified version of the IEEE 118 bus system using measurements with/without noise. We also looked at the poles/zeros of the Padé approximant to analyze the source of estimation error. We found that spurious pole/zero pairs caused by measurement error and roundoff error impacted accuracy. Developing different ways to minimize the effect of noise is necessary and is left for future work.

7 CONCLUSION AND FUTURE WORK

7.1 Conclusion

The Holomorphic Embedding Method (HEM) is theoretically guaranteed to converge to the operable solution provided Stahl's conditions are satisfied. Numerically, however, the limitations of machine precision can affect the numerical performance, especially for heavily-loaded and ill-conditioned power system models. Two numerical examples are given in chapter 3 to show the benefits of using extended precision.

In the HEM algorithm, there exist three places that deserve attention in terms of numerical convergence: the matrix equation solution, power series inversion and the Padé approximant calculation. In chapter 4, different levels of precision were assigned to these three aspects to investigate which aspect was the most critical and require extended precision. Numerical results showed that extended precision must be used for the entire algorithm to improve numerical performance.

Investigation of the numerical properties of the scalable formulation and the non-scalable formulation was reported in chapter 5. The two formulations show different numerical performance on the 43 bus system and the IEEE 145 bus system. For the 43 bus system, the HEM with the scalable formulation is able to give a converged solution while the HEM with the non-scalable formulation fails to converge. On the contrary, for the IEEE 145 bus system, the HEM scalable form fails to converge while the HEM

non-scalable form does converge. Therefore, one needs to be careful to decide which formulation to use to solve the power flow for a power system model.

The application of HEM to the SNBP estimation using local-measurements was explored in chapter 6. The Maximum Power Transfer Theorem (MPTT) was validated using high precision. Different numerical techniques were developed and their numerical performance were tested on the modified 118 bus system with/without noise. Numerical results show that the MPTT method works reasonably well for weak buses in the system. Another alternative method to estimate the SNBP, the roots method, was also discussed in this chapter but shown to be inferior to the performance of the MPTT. The noise in the measurements leads to spurious roots in the Padé approximant and impact the accuracy of the SNBP prediction for both the MPTT and the roots method.

7.2 Future work

The accuracy of the numerical results obtained in this work for estimating the SNBP from noisy measurements were not acceptable. The spurious roots caused by either measurement error or roundoff error affected the accuracy of the SNBP prediction. There are generally two approaches for minimizing the effect of noise that can be investigated in the future:

1. Eliminating noise in the pseudo measurements by:
    - Using a Kalman Filter to reduce improve the quality of the measurements.
2. Eliminating spurious poles caused by round-off error in the calculation of the

Padé approximant by:

- Reducing the order of Padé approximant.
- Developing more robust Padé approximant methods such as robust SVD method [56] and matrix pencil method.

REFERENCES

[1] J. D. Glover, M. S. Sarma and T. J. Overbye, “Power system analysis and design 4th edition,” Cengage Learning, Stamford, 2007.

[2] H. Hale and J. Ward, "Digital computer solution of power flow problems," AIEE Transactions, pt. III (Power Apparatus and Systems), vol. 75, pp. 398-402, 1956.

[3] W. F. Tinney and C. E. Hart, "Power flow solution by Newton's method," IEEE Transactions on Power Apparatus and systems, no. 11, pp. 1449-1460, 1967.

[4] W. F. Tinney and J. W. Walker, "Direct solutions of sparse network equations by optimally ordered triangular factorization," Proceedings of the IEEE, vol. 55, no. 11, pp. 1801-1809, 1967.

[5] B. Stott and O. Alsac, "Fast decoupled load flow," IEEE transactions on power apparatus and systems, no. 3, pp. 859-869, 1974.

[6] B. Stott, “Decoupled Newton Load Flow,” IEEE Transactions on Power Apparatus and Systems, Sep. 1972, vol. PAS-91, no. 5, pp. 1955-1959.

[7] S. Iwamoto and Y. Tamura, "A load flow calculation method for ill-conditioned power systems," IEEE transactions on power apparatus and systems, no. 4, pp. 1736-1743, 1981.

[8] P. Bijwe and S. Kelapure, "Nondivergent fast power flow methods," IEEE Transactions on Power Systems, vol. 18, no. 2, pp. 633-638, 2003.

[9] D. J. Tylavsky, P. E. Crouch, L. F. Jarriel, and H. Chen, "Advances in fast power flow algorithms," in Control and Dynamic Systems, vol. 44: Elsevier, 1991, pp. 295-343.

[10] P. J. Lagacé, M.-H. Vuong, and I. Kamwa, "Improving power flow convergence by Newton Raphson with a Levenberg-Marquardt method," in Power and Energy Society General Meeting-Conversion and Delivery of Electrical Energy in the 21st Century, 2008 IEEE, 2008, pp. 1-6: IEEE.

[11] D. J. Tylavsky, P. Crouch, L. F. Jarriel, and R. Adapa, "Improved power flow robustness for personal computers," IEEE transactions on industry applications, vol. 28, no. 5, pp. 1102-1108, 1992.

[12] D. J. Tylavsky, P. E. Crouch, L. F. Jarriel, and H. Chen, "Advances in fast power flow algorithms," in Control and Dynamic Systems, vol. 44: Elsevier, 1991, pp. 295-343.

[13] M. D. Schaffer and D. J. Tylavsky, "A nondiverging polar-form Newton-based power flow," IEEE Transactions on Industry Applications, vol. 24, no. 5, pp. 870-877, 1988.

[14] A. Trias, "The holomorphic embedding load flow method," in Power and Energy Society General Meeting, 2012 IEEE, 2012, pp. 1-8: IEEE.

[15] G. A. Baker, G. A. Baker Jr, G. A. BAKER JR, P. Graves-Morris, and S. S. Baker, Padé approximants. Cambridge University Press, 1996.

[16] R. J. Avalos, C. A. Cañizares, F. Milano, and A. J. Conejo, "Equivalency of continuation and optimization methods to determine saddle-node and limit-induced bifurcations in power systems," IEEE Transactions on Circuits and Systems I: Regular Papers, vol. 56, no. 1, pp. 210-223, 2009.

[17] D. R. Gurusinghe, "Saddle Node Bifurcation and Voltage Stability Analysis of Sri Lanka," Engineer: Journal of the Institution of Engineers, Sri Lanka, vol. 45, no. 4, 2012.

[18] V. Ajjarapu and C. Christy, "The continuation power flow: a tool for steady state voltage stability analysis," IEEE transactions on Power Systems, vol. 7, no. 1, pp. 416-423, 1992.

[19] E. Garbelini, D. A. Alves, A. B. Neto, E. Righeto, L. C. da Silva, and C. A. Castro, "An efficient geometric parameterization technique for the continuation power flow," Electric Power Systems Research, vol. 77, no. 1, pp. 71-82, 2007.

[20] E. d. M. Magalhães, A. Bonini Neto, and D. A. Alves, "A parameterization technique for the continuation power flow developed from the analysis of power flow curves," Mathematical Problems in Engineering, vol. 2012, 2012.

[21] A. B. Neto and D. Alves, "Improved geometric parameterisation techniques for continuation power flow," IET generation, transmission & distribution, vol. 4, no. 12, pp. 1349-1359, 2010.

[22] A. Jalali, M. Aldeen, "Novel continuation power flow algorithm", IEEE PES International Conference on Power Systems Technology (POWERCON), 2016.

[23] P. Xu, X. Wang, and V. Ajjarapu, "Continuation power flow with adaptive stepsize control via convergence monitor," IET generation, transmission & distribution, vol. 6, no. 7, pp. 673-679, 2012.

[24] D. A. Alves, L. C. da Silva, C. A. Castro, and V. F. da Costa, "Continuation fast decoupled power flow with secant predictor," IEEE transactions on Power Systems, vol. 18, no. 3, pp. 1078-1085, 2003.

[25] S. H. Li and H. D. Chiang, "Continuation power flow with multiple load variation and generation re-dispatch patterns," in Power Engineering Society General Meeting, 2006.

[26] S. D. Rao, D. J. Tylavsky, and Y. Feng, "Estimating the saddle-node bifurcation point of static power systems using the holomorphic embedding method," International Journal of Electrical Power & Energy Systems, vol. 84, pp. 1-12, 2017.

[27] G. Baker and P. Graves-Morris, "Padé approximants," Series: Encyclopaedia of Mathematics and its applications, Cambridge University Press, pp. 73-85, 1996

[28] Y. L. Luke, "Computations of coefficients in the polynomials of Padé approximations by solving systems of linear equations," Journal of Computational and Applied Mathematics, vol. 6, no. 3, pp. 213-218, 1980.

[29] Y. L. Luke, "A note on evaluation of coefficients in the polynomials of Padé approximants by solving systems of linear equations," Journal of Computational and Applied Mathematics, vol. 8, no. 2, pp. 93-99, 1982.

[30] S. Tripathy, G. D. Prasad, O. Malik, and G. Hope, "Load-flow solutions for ill-conditioned power systems by a Newton-like method," IEEE Transactions on Power apparatus and Systems, no. 10, pp. 3648-3657, 1982.

[31] A. Trias and J. L. Marin, "A Padé -Weierstrass technique for the rigorous enforcement of control limits in power flow studies," arXiv preprint arXiv:1707.04064, 2017.

[32] K. Vu, M. M. Begovic, D. Novosel, and M. M. Saha, "Use of local measurements to estimate voltage-stability margin," IEEE Transactions on Power Systems, vol. 14, no. 3, pp. 1029-1035, 1999.

[33] D. Julian, R. P. Schulz, K. Vu, W. H. Quaintance, N. B. Bhatt, and D. Novosel, "Quantifying proximity to voltage collapse using the voltage instability predictor (VIP)," in Power Engineering Society Summer Meeting, 2000. IEEE, 2000, vol. 2, pp. 931-936: IEEE.

[34] I. Smon, G. Verbic, and F. Gubina, "Local voltage-stability index using Tellegen's theorem," IEEE Transactions on Power Systems, vol. 21, no. 3, pp. 1267-1275, 2006.

[35] S. Corsi and G. N. Taranto, "A real-time voltage instability identification algorithm based on local phasor measurements," IEEE transactions on power systems, vol. 23, no. 3, pp. 1271-1279, 2008.

[36] H. Yuan and F. Li, "A comparative study of measurement-based Thevenin equivalents identification methods," in North American Power Symposium (NAPS), 2014, 2014, pp. 1-6: IEEE.

[37] EPRI Technical Update: Voltage Instability Load Shedding. EPRI, Palo Alto, CA: 2006. 1012491.

[38] M. Zima, M. Larsson, P. Korba, C. Rehtanz, and G. Andersson, "Design aspects for wide-area monitoring and control systems," Proceedings of the IEEE, vol. 93, no. 5, pp. 980-996, 2005.

[39] G. Huang, L. Zhao, “Measurement Based Voltage Stability Monitoring of Power System,” PSERC publication 2001, available online: www.pserc.wisc.edu, 2001

[40] M. Larsson, C. Rehtanz, J. Bertsch, “Real-Time Voltage Stability Assessment of Transmission Corridors,” Proc. IFAC Symposium on Power Plants and Power Systems, Seoul, S. Korea, 2003

[41] J.-H. Liu and C.-C. Chu, "Wide-area measurement-based voltage stability indicators by modified coupled single-port models," IEEE Transactions on Power Systems, vol. 29, no. 2, pp. 756-764, 2014.

[42] S. G. Ghiocel et al., "Phasor-measurement-based voltage stability margin calculation for a power transfer interface with multiple injections and transfer paths," in Power Systems Computation Conference (PSCC), 2014, 2014, pp. 1-6: IEEE.

[43] F. Hu, K. Sun, A. Del Rosso, E. Farantatos, and N. Bhatt, "Measurement-based real-time voltage stability monitoring for load areas," IEEE Transactions on Power Systems, vol. 31, no. 4, pp. 2787-2798, 2016.

[44] B. Milosevic, M. Begovic, “Voltage-stability protection and control using a wide-area network of phasor measurements,” IEEE Trans. Power Systems, vol. 18, no. 1, pp. 121-127, 2003.

[45] M. Glavic and T. V. Cutsem, “A Short Survey of Methods for Voltage Instability Detection,” Proceedings of the IEEE PES General Meeting, Detroit, July 2011.

[46] Uznanski, Dan. "Arbitrary Precision." From MathWorld--A Wolfram Web Resource, http://mathworld.wolfram.com/ArbitraryPrecision.html

[47] Advanpix, “Multiprecision Computing Toolbox for MATLAB,” http://www.advanpix.com.

[48] Advanpix, “Symbolic Math Toolbox (VPA) vs. Multiprecision Computing Toolbox,”

[49] H. Stahl, “On the convergence of generalized Padé approximants,” Constructive Approximation, vol. 5, pp. 221–240, 1989.

[50] A. Trias, “Two-bus load flow: exact developments”, Notes available at URL: http://www.gridquant.com/technology/

[51] S. D. Rao, "Exploration of a Scalable Holomorphic Embedding Method Formulation for Power System Analysis Applications," Arizona State University, 2017.

[52] Y. Zhu, D. Tylavsky, and S. Rao, "Nonlinear structure-preserving network reduction using holomorphic embedding," IEEE Transactions on Power Systems, vol. 33, no. 2, pp. 1926-1935, 2018.

[53] S. Rao and D. Tylavsky, "Nonlinear network reduction for distribution networks using the holomorphic embedding method," in North American Power Symposium (NAPS), 2016, 2016, pp. 1-6: IEEE.

[54] P. Kundur, N. J. Balu, and M. G. Lauby, Power system stability and control. McGraw-hill New York, 1994.

[55] “Voltage Security Assessment Tool,” DSATools, accessed in April 2015, available at: http://www.dsatools.com/html/prod_vsat.php.

[56] P. Gonnet, S. Suttel, and L. N. Trefethen, “Robust Padé Approximation via SVD,” SIAM Review, vol. 55, no. 1, pp. 101-117, 2013.